

METALLIC QUANTUM WELL STATES AND CHEMISORPTION

BY LEVAN TSKIPURI

A dissertation submitted to the
Graduate School—New Brunswick
Rutgers, The State University of New Jersey
in partial fulfillment of the requirements
for the degree of
Doctor of Philosophy
Graduate Program in Physics and Astronomy

Written under the direction of
Professor Robert A. Bartynski
and approved by

New Brunswick, New Jersey

October, 2009

ABSTRACT OF THE DISSERTATION

Metallic Quantum Well States and Chemisorption

by Levan Tskipuri

Dissertation Director: Professor Robert A. Bartynski

In this thesis the adsorption properties of carbon monoxide (CO) on the epitaxial fcc-Co/Cu(100), Ni/Cu (100) and Cu/fcc-Fe/Cu(100) systems are reported. The fcc-Co/Cu(100), Ni/Cu(100) systems are known to exhibit metallic quantum well (MQW) states at energies 1 eV or greater above the Fermi level, that disperse upward with increasing film thickness, but never cross the Fermi level and are less pronounced than MQW features in Cu/fcc-Fe/Cu(100) system. The presence of quantum size effects in electronic structure of these systems gives a possibility to modify molecule-surface interactions and influence CO adsorption. All these systems were explored with low energy electron diffraction (LEED), inverse photoemission (IPE), infrared absorption (FTIR) Spectroscopy and temperature programmed desorption (TPD).

TPD measurements revealed several desorption features upon CO adsorption on The fcc-Co/Cu(100), Ni/Cu(100) systems. These TPD features are linked to the corresponding modes in IR spectra and suggest a range of bonding configurations at Co and Ni surfaces. The analysis of TPD and FTIR spectra are given. The adsorption properties of these thin film surfaces are compared to those of single crystal hcp-Co and Ni(100).

For increasing thickness of Cu on the fcc-Fe/Cu system, MQW states periodically cross and modulate IPE intensity at Fermi level. Changes in the peak temperature of TPD spectra are correlated with these modulations of IPE intensity. IR shows two features in the CO stretch frequency spectra, which are identified as CO adsorbed on terrace sites and at step sites. The IR results also suggest a correlation between intensities of these two spectral features and MQW states crossing the Fermi level.

The results of measurements done on the dimethyl disulfide (DMDS) molecule adsorbed on the Cu/fcc-Fe/Cu(100) MQW system is also reported. DMDS is a simple example of an organic thiol, a class of molecules that exhibit self-assembly properties on metal surfaces. The measurements suggest possible modifications of molecular adsorption on the Cu surface. Similarities and differences of DMDS molecule adsorption on thin film Cu(100) and single crystal Cu(100) will be discussed.

Acknowledgements

I wish to express my gratitude towards the people who helped me through these long, unforgettable years which I spent at Rutgers as a graduate student. First, I would like to thank my thesis advisor Bob Bartynski for being a great teacher and kind friend, whose invaluable help in and outside the lab and his tolerance to my odds made this thesis possible. It was Bob's merit to create the working and friendly atmosphere in the group, without which research would not be so fun. I would also like to thank past and present group members including Sylvie Rangan, who aided me throughout my research and who has been real friend and a person one seeks then problem arises, Hua Yao and Anthony Danise, from whom I inherited experimental chamber and guidance during my early stage of being experimentalist, Eric Bersch who always was there to listen to my every problem starting from experiment and ending with household. Many thanks to James Lallo, Senia Katalinic, Ryan Thorpe, Eva Dupont-Ferrier, Everett Lee and many others, whose friendship made lab, lunch and coffee break more fun. I also owe thanks to Jean-Francois Veyan who was a great help in many technical details regarding my experiment and while I was working in the student machine shop, also Thanks to Bill, Ernie, Eric and Arvid from machine shop for turning my clumsy experimental designs into well-machined pieces of equipment.

I would like to express my gratitude to people in the Rutgers physics department and beyond. First of all, I should mention my old friends Mike, Korneel, Junya and CJ, with whom I spent many hours studying physics during my first two years of graduate school, other grad students for sharing crazy evenings and even nights working on homework in ARC building. I do appreciate the great lectures and guidance I have

received from many professors in the physic department, especially Theodore Madey, David Vanderbilt, Piers Coleman, Natan Andrei and Ronald Ransome.

Finally, I would like to thank my family, my little son whose arrival has changed my relaxed, somewhat irresponsible student life forever, and my wife Tamar, my dearest and best friend.

Dedication

To my wife Tamar

and

my son Teimuraz

Table of Contents

Abstract	ii
Acknowledgements	iv
Dedication	vi
List of Tables	ix
List of Figures	x
1. Introduction	1
1.1. Overview	1
1.2. Metallic quantum well states	1
1.3. Chemisorption	5
1.4. Thesis outline	9
2. Experimental Aspects	10
2.1. Introduction	10
2.2. Ultra High Vacuum	11
2.3. Sample preparation	15
2.4. Techniques	18
2.5. Summary	41
3. Unoccupied states of fcc-Co/Cu(100) and CO chemisorption	42
3.1. Introduction	42
3.2. Experimental Aspects	45

3.3. Unoccupied States of fcc-Co/Cu(100)	48
3.4. CO adsorption: Results and Discussion	58
3.5. Summary	71
4. Unoccupied electronic structure and CO chemisorption on the Ni/Cu(100) system	73
4.1. Introduction	73
4.2. Experimental Aspects	75
4.3. Unoccupied electronic structure of the Ni/Cu(100)	76
4.4. CO adsorption on Ni/Cu(100) system	82
4.5. Summary	91
5. CO and dimethyl disulfide (DMDS) chemisorption on the Cu/fcc-Fe/Cu(100) system	93
5.1. Introduction	93
5.2. Experimental Aspects	95
5.3. IPE spectra of the Cu/fcc-Fe/Cu(100) and CO chemisorption	96
5.4. DMDS adsorption on Cu/fcc-Fe/Cu(100) system: results and discussion	105
5.5. Summary	120
Appendix A. List of Acronyms	122
References	123
Vita	131

List of Tables

5.1. Vibrational modes of DMDS and methanethiol/Cu(100) system	117
--	-----

List of Figures

1.1. Schematic representation of a MQW states	3
1.2. Schematic representation bulk and projected bands	4
1.3. Charge densities of CO orbitals	7
1.4. A simple picture illustrating CO-metal bonding	7
2.1. A schematic drawing of UHV chamber	13
2.2. A schematic drawing of e-beam metal evaporation source	16
2.3. Schematics of Michelson interferometer	19
2.4. The interferogram and the single-beam FTIR spectrum	22
2.5. Illustration of the inverse photoemission process	24
2.6. Schematics of IPE geometry	26
2.7. IPE spectrum from the Cu(100) single crystal	28
2.8. Schematic diagram for TPD experimental setup	30
2.9. TPD spectrum of 1 ML CO/Cu(100)	31
2.10. A schematic drawing of LEED	32
2.11. A schematic energy diagram of Auger process for an atom in a solid [1]	34
2.12. Auger spectrum of clean Cu(100)	35
2.13. A schematic drawing of a double-pass CMA	36
2.14. Schematics of Auger experimental setup	37
2.15. A schematic figure of an STM [2]	39
3.1. Direct lattice, reciprocal lattice and special points of the surface Brillouin zone (SBZ) of the face center cubic (fcc) crystalline structure	45

3.2. LEED pattern from the clean Cu(100) surface.	47
3.3. LEED pattern from a 5 ML fcc-Co/Cu(100) MQW surface.	47
3.4. IPE spectra of clean Cu(100) and fcc-Co/Cu(100)	49
3.5. Comparison of energy bands $E(\mathbf{k})$ of Co and Cu	50
3.6. IPE spectra from the CO/n-ML Co/Cu(100) system	52
3.7. A schematic drawing of the PAM model	54
3.8. PAM calculation results: phase vs energy	57
3.9. PAM calculation vs experiment	58
3.10. FTIR spectra from the CO/5 ML fcc-Co/Cu(100) system	60
3.11. TPD spectra from CO/5 ML fcc-Co/Cu(100) system	61
3.12. FTIR spectra of CO adsorbed on 5 ML fcc-Co/Cu(100)	62
3.13. Infrared spectra of CO adsorbed on 5 ML fcc-Co/Cu(100) surface at RT	63
3.14. TPD spectra from CO/8 ML fcc-Co/Cu(100)	66
3.15. TPD spectra from CO/n-ML fcc-Co/Cu(100) films	67
3.16. STM image of cobalt thin film grown on Cu(100)	69
3.17. High temperature annealing effect for cobalt films	70
4.1. The band structure of Ni(100) [3]	76
4.2. IPE spectra from the Ni(100)	77
4.3. IPE spectra from the Ni/Cu(100) system [1]	78
4.4. PAM calculation vs experiment	80
4.5. IPE spectra from CO covered Ni films [1]	81
4.6. CO adsorption sites on a Ni(100) surface.	83
4.7. TPD spectra from the surface of the Ni(100) single crystal [4]	83
4.8. FTIR spectra from the CO/7 ML Ni/Cu(100) system for different CO exposures	85
4.9. TPD spectra from different CO exposures onto 10ML Ni/Cu(100) film	87

4.10. TPD spectra from 1L CO adsorbed onto n-Ni/Cu(100) film	88
4.11. FTIR spectra from the CO/7 ML Ni/Cu(100) system annealed to inter- mediate temperatures	89
4.12. FTIR spectra from the CO/5 ML Ni/Cu(100) and Ni(100)	90
5.1. IPE spectra from the Cu/fcc-Fe/Cu(100) system	97
5.2. T_d and IPE intensity at E_F from the Cu/fcc-Fe/Cu(100) system	99
5.3. FTIR spectra from the Cu/fcc-Fe/Cu(100) system	100
5.4. STM images of the Cu/fcc-Fe/Cu(100) surface	101
5.5. FTIR spectra peak intensities vs Cu film thickness for Cu/fcc-Fe/Cu(100) system	102
5.6. A schematic view of methanethiolate formation on Cu(100) surface . . .	105
5.7. IPE spectra from the DMDS/Cu/fcc-Fe/Cu(100) system	106
5.8. Calculated DOS for methanethiol - single Cu atom	108
5.9. Electronic orbitals of unsupported methanethiol & methanethiol - single Cu atom system	109
5.10. STM images of the DMDS/Cu(100) surface	112
5.11. Auger spectrum of annealed DMDS/Cu(100) and Cu(100)	113
5.12. LEED image of the DMDS/Cu(100) surface	114
5.13. FTIR spectra from the DMDS/Cu/fcc-Fe/Cu(100) system	118
5.14. TPD spectra from the Cu films exposed to DMDS	119

Chapter 1

Introduction

1.1 Overview

The field of surface science has developed very quickly during past few decades, along with advances in fabrication and measurement technologies at nanometer length scales. This dramatic reduction in size brought along the concepts of reduced dimensionality, reduced symmetries, changes in structural geometry, new types of interactions involving electron spin and different kinds of physical phenomena behind it [5, 6]. The development of molecular beam epitaxy (MBE) made it possible to grow layered nanostructures [7] with atomic-scale thickness control. At this scale under favorable conditions and material selection, one could stabilize nanostructures in a state which was different from the equilibrium bulk structure [8, 9]. Research over the past years has shown that the quantum size effects (QSE) can be manifested in small dimensions. In some cases the properties of metal are even dominated by these QSE, the importance of which we will try to address in this thesis.

1.2 Metallic quantum well states

A good example of a system with quantum size effects (QSE) is a metal thin film grown on another metal substrate. When the thickness of a metal film reaches nanoscale dimensions, QSE can cause many material properties to differ greatly from those of the bulk [5, 6, 10, 11, 12, 13]. In particular, electronic states become confined in the

direction perpendicular to the plane of the film and their energy spectrum acquires discrete features. These confined states, often called metallic quantum well (MQW) states, change energy as a function of film thickness and have been linked to many unique properties of ultrathin metal films and multilayers. For example, MQW states are thought to mediate the magnetic exchange coupling between ultrathin ferromagnetic films separated by a nonmagnetic spacer layer, leading to the giant magnetoresistance (GMR) effect [5, 6, 14, 15]. A simple example of a GMR system is magnetic metal layers, which are separated with non-magnetic metal spacer layers, such as Cu or Au. The resistance in GMR systems can change dramatically depending on the direction of the applied magnetic field [16, 17]. The resistance of the material is low (high) when the magnetic moments in magnetic layers separated by the non-magnetic spacer layer are parallel (anti-parallel). Such devices are used in production of magnetic memories and sensors [18].

MQW states also have been found to stabilize certain thicknesses in metal thin film or island growth on various substrates, a phenomenon that has come to be known as electronic growth [19, 20, 21, 22, 23]. In addition there have been reports that the superconducting properties of ultrathin Pb films, including the critical temperature and magnetic field, as well as flux pinning properties, are strongly modified when accompanied by quantum confinement in ultrathin films [24]. In each of these cases, the unusual physical behavior has been correlated with MQW states crossing the Fermi level as the thickness in the confinement direction is varied. Several recent studies have examined the interaction between adsorbates and the surfaces of MQW systems [25, 26, 27]. Upon exposing ultrathin Mg MQWs grown on Si to various exposures of oxygen, Aballe et al. [27] using low-energy electron microscopy (LEEM) and x-ray photoelectron emission microscopy (XPEEM), found that the relative intensity of the chemically shifted Mg 2p core level was enhanced, thus indicating increased reactivity, for those thicknesses where MQW states cross the Fermi level. In a different investigation focusing on molecular

chemisorption, Danese et al. [28] found an oscillatory change in the bonding energy of CO to the surface of the Cu/fcc-Fe/Cu(100) system, characterized by increases in the peak temperature in temperature programmed desorption (TPD) spectra when Cu MQW states crossed the Fermi level.

The main focus of our interest in this thesis are the noble metal - transition metal systems, mostly because these systems are prototypes for magnetic and catalytic applications. For more detail discussion of MQW states in the later chapters, it will be helpful to put some light onto the subject. As the name already suggests, MQW states are similar to the electronic states in a sample square well potential. When the interface between the thin film and the substrate has high electron reflectivity, the majority of a valence electron wave function is confined in the metal film, and unoccupied MQW states are created by quantizing the confined electron momentum perpendicular to the surface [29]. The metal film may be bound on both sides by another metal substrate or can be bounded on one side by a different metal layer and on the other by vacuum. Fig. 1.1 below shows a schematic diagram of possible MQW wave functions in each of these structures.



Figure 1.1: schematic representation of a MQW states [30]. Left: metal thin film bounded on one side by different metal layer and on the other by vacuum; Right: metal thin film bounded on both sides by different metal layer.

Similar to the square well potential problem, one should expect the energy of MQW states to change as a function of film thickness, which indeed is true, but there are

some differences characteristic to MQW states only. Unlike simple model states in MQW system usually disperse upward in energy and this behavior was related to band structure of the metal film [14, 15]. The fact that electrons are confined in the perpendicular direction, but free to move in the plane of the film, results in a two dimensional dispersion as a function of parallel momentum k_{\parallel} . For a given value of k_{\parallel} we consider the quantization of the perpendicular component of momentum, k_{\perp} . As a consequence projecting the bulk bands in the direction perpendicular to the surface leads to the formation of the projected bulk band structure [31]. Figure 1.2 illustrates the relationship between the bulk bands and projected bands.

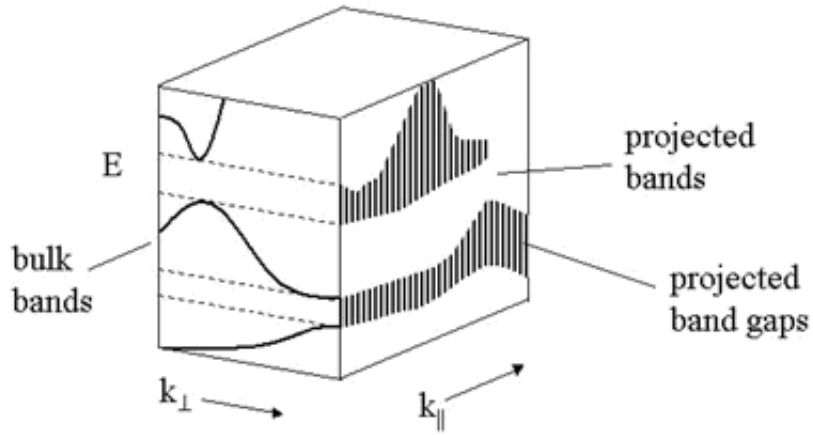


Figure 1.2: Schematic representation of bulk and projected bands [31].

The interface scattering magnitude will depend on the electronic structure both of the film and the substrate material, and how the projected band gaps are aligned with respect to each other. There are two distinct cases: If the energy levels of the film are degenerate with the projected bands of the substrate, then this film state may couple to substrate state to form a so-called quantum well resonance. Such resonances allow charge carrier tunnelling through the interface. In another scenario the energy state in the film encounters a band gap of the substrate and forms a true quantum well state.

Usually both quantum resonances and quantum well states have substantial impact on density of states of the film and therefor it is unnecessary to make sharp distinction between true quantum well states and resonances.

1.3 Chemisorption

So far we have discussed MQW states and their role in changing the local electronic structure and magnetic properties of a material, but this list is not exhaustive: investigation of catalytic properties, namely modification and control of molecule-surface reactions long has been point of scientific interest. A catalyst itself is a substance that increases the rate and improves the selectivity of a chemical reaction without being consumed in the process. A typical approach to studying the fundamental processes that control catalyzes, involves the study of prototype chemical reactions at well-ordered, clean single crystal surfaces. The catalytic properties of such surfaces vary as a function of a combination of various external parameters like temperature, pressure, etc. In contrast to this, there exists a class of bimetallic catalysts, which offer great deal of flexibility in terms of adjustable internal parameters like thickness of the metal film or morphology of an active surface. Using metal alloys often improves catalytic performance, since two or more metals cooperate in order to enhance an ongoing chemical reaction.

The ability to control catalytic properties and molecular adsorption on thin metal films has drawn a significant amount of interest to the study of chemical reactions on such surfaces. Research has shown that transition metal alloys are good candidates for bimetallic catalysts and can outperform single metals in both catalyzing gas-phase chemical reactions [32] and production of certain carbon nanostructures grown by chemical vapor deposition (CVD) [33, 34]. In order to understand molecule-surface reactions two main experimental methods are employed in this thesis research. First, one should

be able to access bonding energy between the molecule and the surface. This is achieved by measuring the molecule desorption temperature from the surface, which is a temperature where a molecules' desorption rate from the surface is at a maximum under a constant rate of heating. Second - it is important to extract information about the site-specific behavior of molecules on the surface and adsorption site characteristics, which can be obtained by measuring vibrational spectrum of molecule itself. A good test molecule in many case studies of chemisorption on transition metal surfaces is the carbon monoxide (CO) molecule. CO is a simple molecule with a high dissociation energy and a well understood electronic structure. Owing to its closed shell electronic structure and high dissociation energy, CO adsorbs molecularly on most transition metal surfaces. Both experimental and theoretical studies indicate [30, 1, 35, 36] that changes in desorption temperature are expected from different transition metal thin film structures (Pd, Ni, Cu) as compared with the corresponding truncated bulk surfaces. A lot of effort has been spent to investigate CO molecule in detail and much experimental and theoretical data exist to accurately account for many of the subtleties of the CO molecular orbitals.

The existing knowledge about the CO molecule gives a lot of insight in understanding molecule-metal bonding character as well. It is well understood that orbitals contributing in CO-metal bond are occupied 5σ , the highest occupied molecular orbital (HOMO), and unoccupied $2\pi^*$, the lowest unoccupied molecular orbital (LUMO). The calculated HOMO and LUMO orbitals of unsupported CO molecule are illustrated on figure 1.3 [37]. Upon bonding to most transition metals, the occupied CO 5σ orbital donates charge to the substrate d-bands, and the substrate d-bands back-donate charge to the unoccupied CO $2\pi^*$ antibonding orbital as explained by Blyholder model [38] and illustrated in the schematic diagram of figure 1.4. This type of adsorption involves a significant charge transfer between the adsorbate and surface, resulting quite strong CO-metal bond formation. In contrast to most transition metal surfaces, where

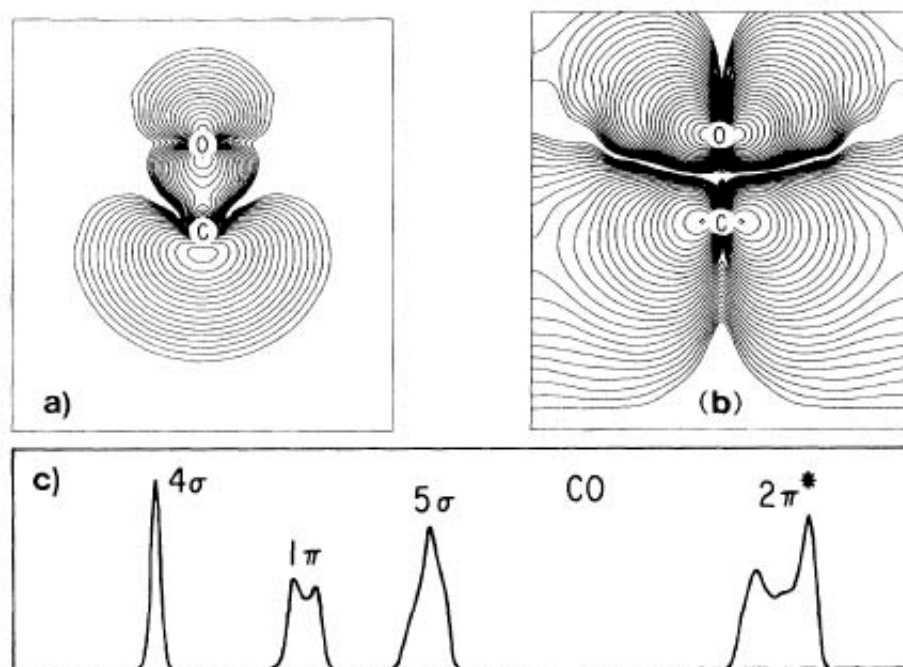


Figure 1.3: Charge densities of (a) 5σ , (b) $2\pi^*$ states in an unsupported film of CO molecules and (c) partial densities of states for unsupported CO film [37].

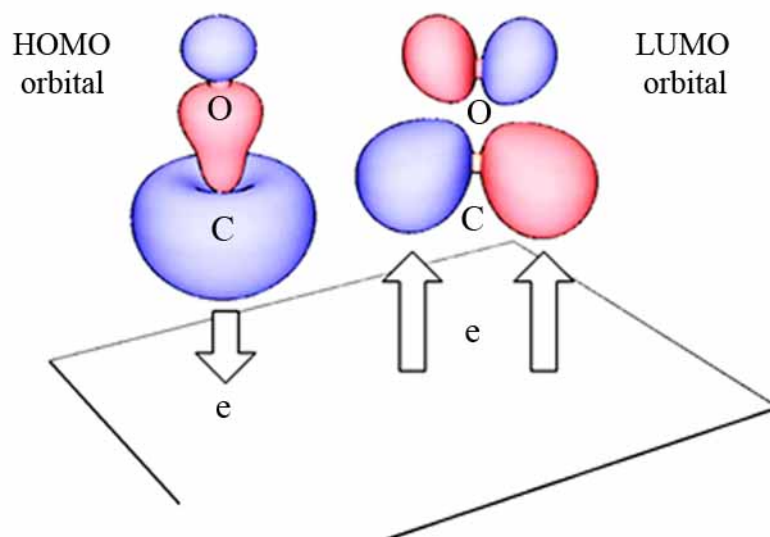


Figure 1.4: A simple picture illustrating how a CO molecule bonds to a transition metal surface.

CO-metal bond is strong, CO interacts more weakly with near noble metal surfaces such as Cu(100), and it is believed that the *sp* electrons of copper play an important role in the bonding of CO to the surface together with the d-band electrons [39]. In this picture, $2\pi^*$ antibonding back donation of electrons is not as intense as in case of transition metals like nickel or cobalt. The weakness of CO-copper interaction and the fact that a lot of MQW states in copper are associated with the quantization of the Cu 4*sp* band makes it possible to see desorption temperature modifications caused by MQW states [28, 30, 40]. Intermolecular interaction is another important factor for CO covered transition metal surfaces, since packing on the surface is usually dense. This interaction results in a formation of ordered over-layers and de-localization of CO orbitals. Usually the carbon-oxygen bond gets weaker upon adsorption on metal surface and one can observe corresponding downward frequency shifts in features in infrared absorption spectra of carbon monoxide adsorbed at different metal surfaces compared to gas phase CO absorption spectra.

Another molecule we tested on transition metal thin films was dimethyl disulfide (DMDS) molecule from the class of self-assembled organic molecules, (SAMs), which forms ordered monolayers on the surface and is interesting as a candidate for molecular electronics applications. These molecules can be tethered to noble-metal surfaces through head-group atoms such as sulfur. The sulfur-metal bond is very strong and temperature programmed desorption (TPD) measurements usually dissociate the molecule, desorb fragments of it, and leave sulfur contaminated metal surface behind. There are experimental and theoretical indications that suggest possible modifications of molecular adsorption on the MQW surface. Studying the CO and DMDS chemisorption on transition metal nanostructures provides ways to understand physics behind the processes in similar structures as well.

1.4 Thesis outline

In this thesis we present studies of an electronic and chemisorption properties of various metallic quantum well (MQW) systems, including Co/Cu(100), Cu/Fe/Cu(100) and Ni/Cu(100). Carbon monoxide and dimethyl disulfide adsorption on these MQW systems is investigated by different experimental techniques. In Chapter 2 we describe details of the experimental setup and explain each experimental procedure including: temperature programmed desorption (TPD), Fourier transformed infrared (FTIR) spectroscopy together with various surface characterization techniques like low energy electron diffraction (LEED) and Auger electron spectroscopy (AES).

The CO chemisorption properties and the experimental results for cobalt metal films of different thickness grown on copper single crystal as well investigation of unoccupied electronic structure of same MQW system are given in Chapter 3. A simple theoretical explanation for unoccupied MQW states as a function of thin film thickness is also given and discussed in the context of the phase accumulation model (PAM).

In Chapter 4 we will discuss CO chemisorption properties and unoccupied electronic structure of Ni/Cu(100) MQW system. CO adsorption on nickel strongly modifies the inverse photoemission (IPE) spectrum by suppressing the surface resonance feature, characteristic to nickel. CO bonding characteristics and desorption temperatures will be also discussed and summarized.

Chapter 5 is dedicated to CO and dimethyl disulfide (DMDS) chemisorption on Cu/fcc-Fe/Cu(100) MQW system. We will try to emphasize quantum size effects (QSEs) present in this particular MQW system, while providing experimental evidence from CO chemisorption studies. At the same time, we will discuss different phases of self-assembled monolayers (SAMs) formed on Cu(100) surface upon adsorbing DMDS.

Chapter 2

Experimental Aspects

2.1 Introduction

The research presented in this thesis requires a special experimental environment in order to achieve the desired quality of surface cleanness, and also the conditions necessary for conducting measurements and acquiring reasonable experimental data. There are several factors we should consider before turning to the experimental techniques for characterization and analysis of a given surface. First of all, one should maintain an atomically clean and well ordered surface for a period of several hours - the usual time required to perform typical experimental measurements. This implies the use of an ultra high vacuum (UHV) chamber, the description of which we will give below. Secondly, the experimental observations require experimental techniques that are very surface sensitive. In other words the response signal coming from the first few atomic layers of given material should be distinguished from that which is coming from the bulk. We will try to address each of these conditions in the present chapter, as well as provide a detailed description of the experimental techniques. Several such techniques, that are particularly useful surface science tools, were employed in this study, including: inverse photoemission (IPE) spectroscopy, low energy electron diffraction (LEED), Auger electron spectroscopy (AES) and scanning tunnelling microscopy (STM). The experimental data obtained using these techniques, combined with other methods for surface analysis, such as Fourier transformed infrared (FTIR) spectroscopy and temperature programmed desorption (TPD), will be the focus of our discussion in the later

chapters.

2.2 Ultra High Vacuum

As we have already mentioned, an ultra high vacuum environment is necessary to avoid surface contamination of the prepared sample from ambient gasses. Simple estimations show that at atmospheric pressure (~ 760 torr), using kinetic theory of gases, predict the formation of a contaminant monolayer ($\sim 10^{15}$ particles per cm^2) on the surface of the sample within nanoseconds. As a consequence, a vacuum pressure that is about 10^{-13} of an atmosphere is needed to keep the sample surface clean for a few hours while performing different measurements. UHV is created inside the stainless steel vacuum chamber with a vacuum pressure of $\sim 10^{-10}$ torr (1 torr= $133 \text{ N/m}^2(\text{Pa})$) or better, using a combination of different vacuum pumps. The common set of pumps include a rotary vane pump, a turbomolecular pump and an ion pump.

The rotary vane pump is the first stage of pumping, where it is used to bring down the pressure below ~ 0.1 Torr. In this pump, a rotary vane is swept to trap the gas at the exhaust of turbomolecular pump, push it to the outlet port, and eventually release it to the atmosphere or, if contents of the exhaust are poisonous or otherwise dangerous, to an environmentally friendly hood [41, 42]. The turbomolecular pump represents a second and a main stage of the pumping cycle. Being backed up by a rotary vane pump, it can operate within wide range of pressures from 1 down to 10^{-10} Torr, using several levels of rotating angled blades (rotors) paired with stationary blades (stators). Operating at very high angular speed¹, each rotary blade transfers momentum to gas particles and pushes them out towards the stationary blade, behind which a new rotor takes over transferring gas particles to the next pumping level. The successive arrangement of rotors and stators with variable blade angles compresses the gas by factor of ~ 5

¹The typical operating speed depends on rotor blade diameter and varies from 3×10^4 rpm to 6×10^4 rpm for some small diameter units.

per level, resulting in a pumping ratio of 10^{-6} or better for most of the gases, except H_2 , between the inlet and outlet ports of the pump. This compression ratio stays the same regardless of outlet pressure. As a result, the ultimate pressure can be reduced by orders of magnitude (down to 10^{-10} Torr), if rotary vane pump pressure were reduced accordingly.

A sputter-ion pump represents the last stage of the pumping cycle. It is a one of the variety of capture pumps, which do not expel the gases they pump during operation, but rather trap and permanently bury them inside their volume. The basic parts of the sputter-ion pump are two parallel, Ti coated stainless steel plates, which are cathodes, and an array of stainless steel cylindrical anode tubes, usually arranged as an egg-crate structure. A high voltage (~ 3 kV) is applied between the cathode plates and the anode tubes, forcing electrons to eject from the cathodes, which then follow a helical path under a strong magnetic field directed along the axis of anode cylinders. Electrons ejected from the cathode plates ionize gas molecules in their elongated path, and these ionized molecules will stick to Ti coated cathode walls, either embedding inside or chemisorbing, thereby effectively pumped out from the volume. In addition, when ionized gas bombards the cathode, some of the titanium is sputtered off onto the anodes and surrounding surfaces and will trap more molecules via chemisorption. This mechanism is often referred as gettering action, and it further increases the pumping speed. The sputter-ion pump is very effective way to pump many reactive gases, even when the high voltage is not applied and discharge is stopped, but it performs poorly on pumping of heavy noble gases, especially when ion bombardment uncovers previously embedded gas. There are several solutions to improve pumping, including both modifications in design and using sputter-ion pump in combination with a titanium sublimation getter pump, detailed descriptions of which are given in literature [41, 42]

Most of the experiments reported in this thesis are performed in a custom built UHV chamber at the Laboratory for Surface Modification (LSM) at Rutgers University. It is

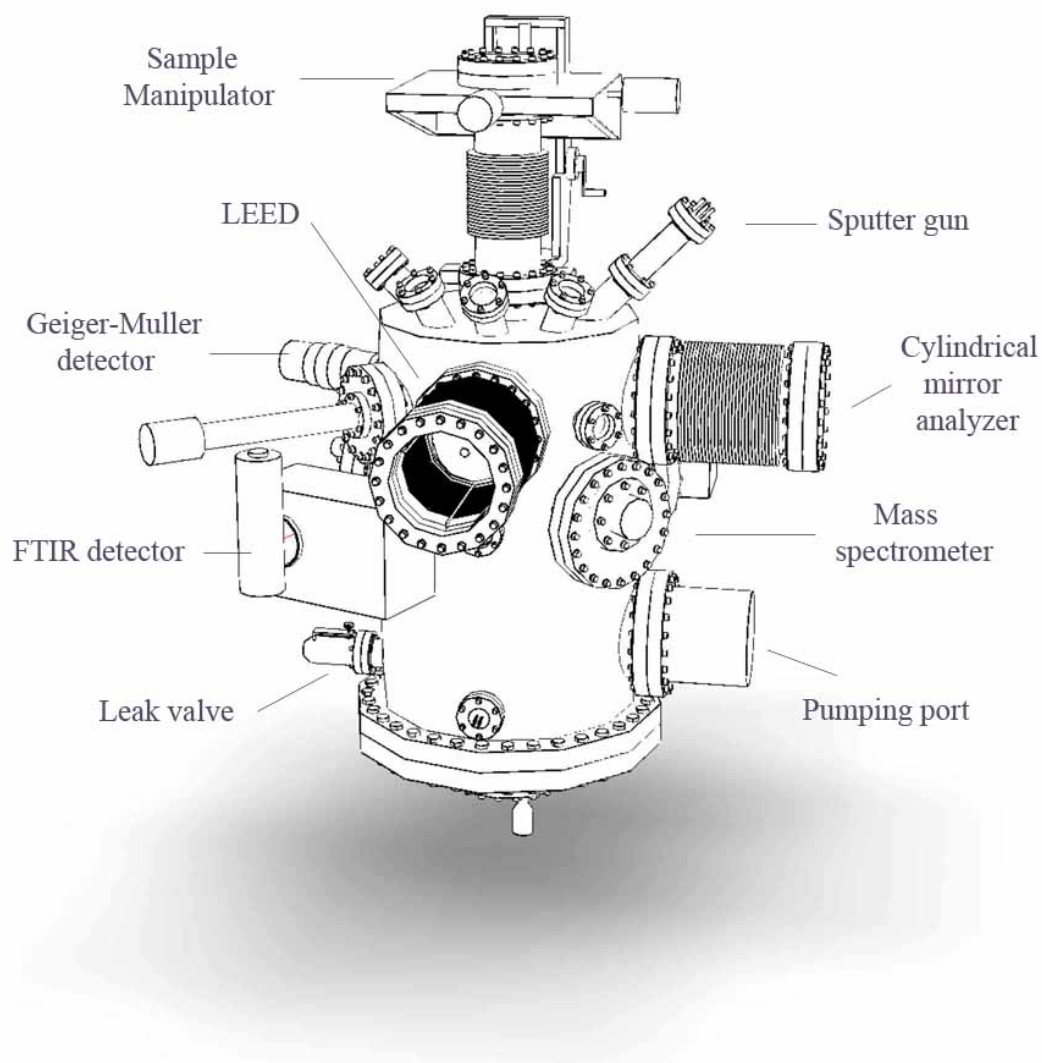


Figure 2.1: A schematic drawing of custom built UHV chamber equipped with: surface preparation tools, including various metal evaporation sources and quartz crystal microbalance QCM for film thickness monitoring, electron gun and the detector for IPE spectroscopy, Fourier transformed infrared (FTIR) spectroscopy with MCT detector and low energy electron diffraction (LEED)

equipped with a different facilities for sample preparation, film growth, characterization, as well as various experimental analyzes tools like: inverse photoemission (IPE) spectroscopy, Auger electron spectroscopy (AES), low energy electron diffraction (LEED), Fourier transformed infrared (FTIR) spectroscopy and temperature programmed desorption (TPD) techniques. A schematic diagram of the chamber is shown in the figure 2.1. Besides the main volume, where preparation and analysis of the sample is carried out, it has a load-lock for rapid sample introduction into the chamber without exposing the main compartment to the open air. A transfer of the sample within a wide range (x direction: 40 mm, y direction: 30 mm, z direction: 150 mm, Rotation angle θ : 360°) can be achieved using the manipulator, located at the top of the chamber. We can apply current or voltage to the sample, as well as measure sample current and the temperature via electrical feed through located at the top of the manipulator.

We already mentioned that UHV conditions are necessary to maintain the clean and well-ordered samples, but surface preparation and analysis tools are also required to operate at low pressures. Since many measurement techniques often involve low energy electrons or ions, they will suffer from significant scattering at the ambient pressure, seriously compromising or prohibiting the experiment unless the pressure is low. In addition to this many experimental procedures involve high voltages and considerable amount of heating. Instrumentation malfunction is expected in the absence of high vacuum conditions and it would be impossible to maintain high voltages without breakdown or discharges occurring. Although high vacuum requirements here are not as strict as in maintaining the surface order and cleanliness, and the usual instrumentation based limit of the pressure is 10^{-6} torr. Overall, UHV is very critical for all experiments reported in this thesis and one should devote a significant amount of time and energy to achieve and maintain good UHV conditions, which includes lot of routine, basic care procedures on a daily basis.

2.3 Sample preparation

Sample preparation is the necessary first step in performing surface physics experiments. The preparation of atomically clean, well-ordered surfaces and interfaces includes procedures for both polishing the sample before introducing it into UHV chamber and farther in situ cleaning using sputter-annealing cycles. All films examined in this thesis were prepared on a Cu(100) single crystal that was cut and polished to within 0.5° of its high symmetry direction, as determined by x-ray diffraction. Polishing is a two step procedure that involves a mechanical polish with the diamond solution and electrochemical polish in 85% phosphoric acid and 15% of deionized water solution.

Once the sample is polished, and it is smooth and scratch free to the eye, the sample is transferred into the UHV chamber using the load-lock, and mounted on a sample holder, which is equipped with a chromel-alumel thermocouple and a heating wire. Inside the UHV chamber the residual surface contamination is removed with cycles of sputtering, where energetic (~ 1 keV) beam of Ne ions is directed to the sample, ejecting surface atoms via momentum transfer in the collision process. An ion current density of $\sim 12 \mu\text{A}/\text{cm}^2$ can be attained with the sputter gun in a good working condition. Formation of the plasma, from which ions are extracted, requires backfilling the chamber with Ne gas and maintaining the pressure of $\sim 5 \times 10^{-5}$ torr for 20-25 minutes, which is a typical time for sputtering in case of Cu(100).

The sputtering process cleans the surface, but disorders it at the same time. Surface order can be facilitated by annealing, where the copper single crystal temperature is elevated up to 750 K for 10-20 minutes. Annealing is an important procedure as surface roughness can degrade the outcome of the experiment and any related quantum size effects (QSEs) therein. The Cu(100) surface is not very reactive to residual gas molecules inside the chamber and it stays clean for quite a long time, which is a significant advantage over other transition metal surfaces.

The next step after attaining a good Cu(100) surface is to grow ultra-thin metal films, and calibrate the film thickness at the atomic scale. For iron, cobalt and nickel

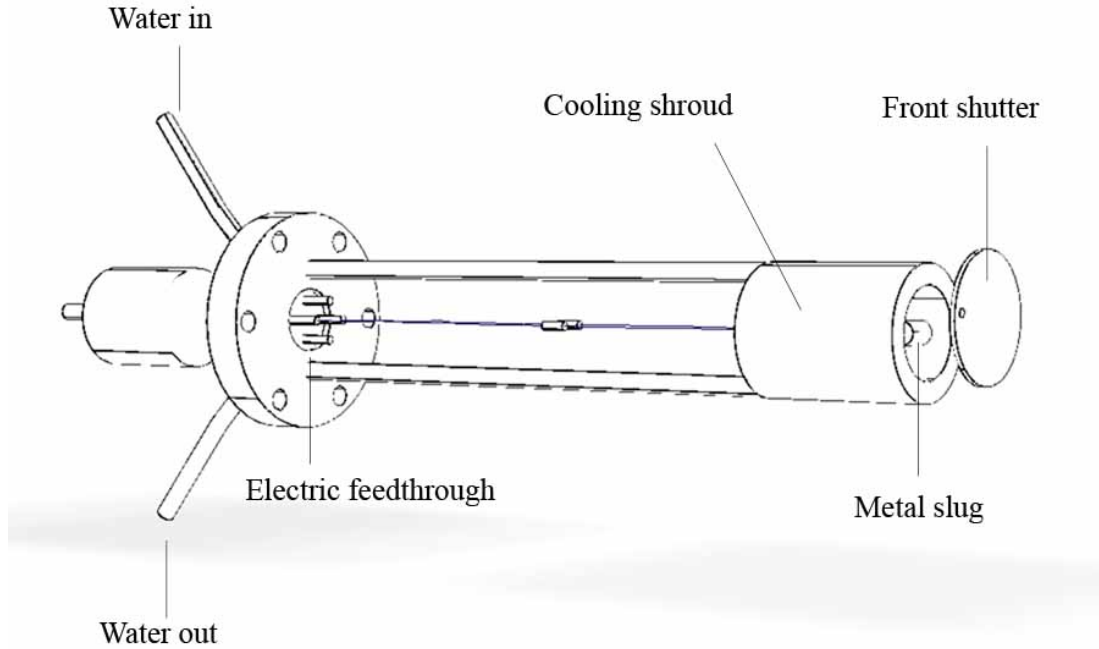


Figure 2.2: A schematic drawing of electron-beam (e-beam) metal evaporation source

thin-film deposition, we use electron-beam (e-beam) metal evaporation sources containing high purity ($\sim 99.95\%$ or better) metal slugs, while for copper deposition we use resistive heating, as described below.

Figure 2.2 is a graphical drawing of a metal evaporator, which illustrates the components and working principles of the e-beam source: a high purity slug of a given metal is placed in front of a tungsten filament and a high voltage (~ 1.2 KeV) is applied between the filament and the evaporation source. As the filament gets hot by passing current through it, electrons are emitted and accelerated towards the metal slug

guided by the high electric field. When these electrons impact the slug, a significant part of their kinetic energy is converted to thermal energy, causing the sublimation of the target material. In this way the sample, which is placed in front of the evaporator, can get sufficient flux of evaporated metal atoms with the typical currents of ~ 30 mA drawn from the filament. In the resistive heating method, a high purity copper wire is tightly wrapped around a tungsten filament and heated by passing current through it. When the temperature of the copper is sufficiently elevated, it melts into a small ball and begins to sublime. In both deposition methods described above, the deposition source is surrounded by a water-cooled stainless steel shroud (As shown in Fig. 2.2) that reduces the background pressure during the sublimation process. A front shutter is used to control the amount of material deposited.

The deposition rate and total deposition thickness can be monitored using a quartz crystal microbalance (QCM). A QCM contains a quartz crystal whose resonant vibrational frequency depends on the amount of mass deposited on it, so one can observe the shift in resonant vibrational frequency as a result of deposited mass. The QCM controller however is typically measuring the relative thickness of a deposited film, since the positions of sample and the QCM are not exactly the same. To make an absolute thickness measurement, the QCM is calibrated by performing Rutherford Backscattering Spectroscopy (RBS) on samples that had thin films, thicknesses of which were determined with QCM, to an accuracy of 0.1 ML. RBS is very sensitive technique, which employs a high energy beam ($\sim 2-4$ MeV) of low mass ions (He^{++}) to probe the test sample and determine the chemical composition or depth profiles of elements in thin films by detecting the elastically backscattered projectiles at large angles [43]. The RBS spectrum was measured at Tandetron accelerator housed in the Laboratory for Surface Modification at Rutgers University. By comparing the RBS results with the crystal monitor reading, absolute calibration of the QCM was obtained. Together with RBS, Auger electron spectroscopy measurements are very helpful to cross check

the relative film thickness, which we will discuss in more detail in Section 2.4.5.

Finally, it is worthwhile to mention that once established and understood, inverse photoemission (IPE) spectra 2.4.2 can also serve as a reference for assessment of thin film thickness and surface quality, since the technique is very sensitive to the composition of the top most layers of the sample surface.

2.4 Techniques

2.4.1 Fourier transform infrared (FTIR) spectroscopy

Fourier transform infrared (FTIR) spectroscopy is a widely used experimental technique to identify molecular adsorbates that form on different surfaces in the course of various chemical reactions, as well as to investigate gas phase systems or liquid suspensions. For our measurement purposes, we performed studies of the adsorbate vibrational properties of CO on MQW systems. One of the great advantage of FTIR spectroscopy is that it is one of the few surface-sensitive probes that provide molecule-specific information without destroying the chemisorbed state. Together with TPD, FTIR can give a more complete picture about the adsorption state of a molecule and its bond with the surface, including information such as: identification of the adsorbate, whether it is dissociated (atomic, molecular or intermediates); determination of the molecular symmetry through the surface dipole selection rule and the number of observed dipole active modes; identification of a bonding site; conclusions on the metal-adsorbate bond through frequency shifts of internal modes in comparison to the gas-phase spectrum of the molecule and the presence of additional vibrational modes if any.

The development of FTIR spectroscopy began with the invention of the two-beam interferometer by Michelson and realization that it was possible to extract spectra from the interferogram through the Fourier transform. The basic idea behind the

FTIR spectroscopy is a possibility to measure the intensity variations of the beam

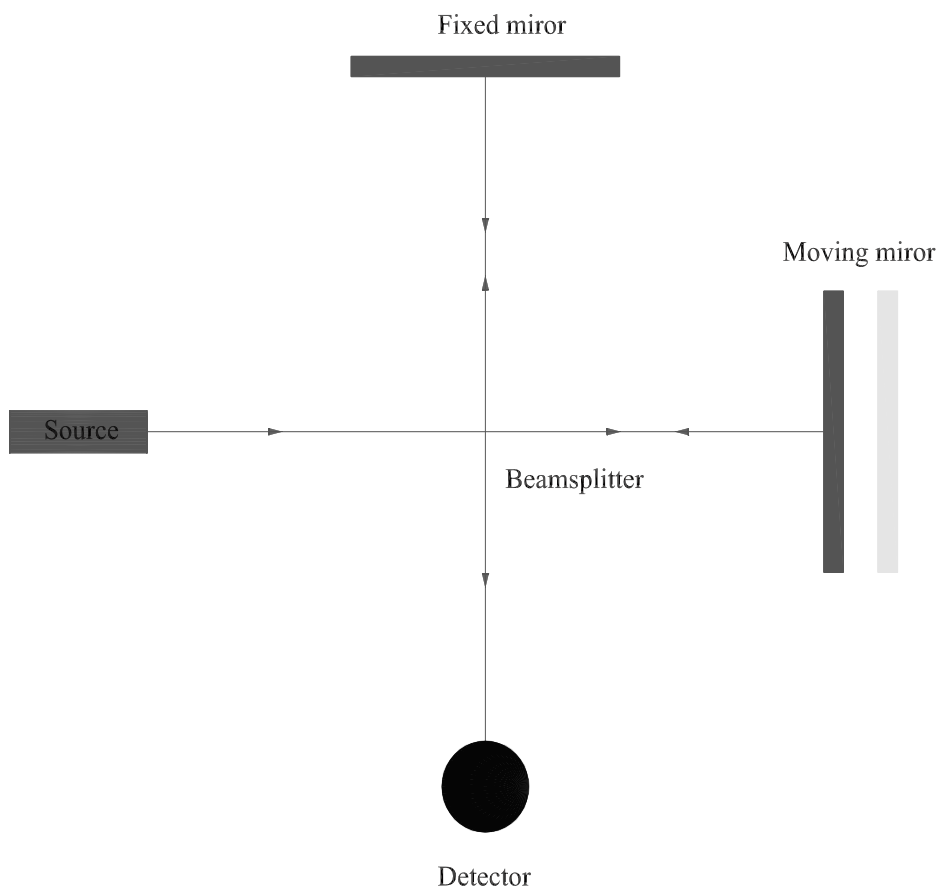


Figure 2.3: Schematics of Michelson interferometer.

coming from the interferometer as a function of path difference. The simple form of the Michelson interferometer is shown on figure 2.3. It consists of two mutually perpendicular mirrors and a beam-splitter. One of the mirrors is fixed and another is movable. The beamsplitter reflects half of the radiation to the fixed mirror and transmits rest to the movable mirror. As the split beams return to the beamsplitter they recombine and again are partially reflected from and partially transmitted through the beamsplitter. The reflected beam goes to the detector and, because of interference

effect, its intensity changes as a function of path difference.

One can consider the monochromatic radiation with the wavenumber:

$$\bar{\nu} = \frac{1}{\lambda} \quad (2.1)$$

When the mirrors are positioned at same distance from beamsplitter the two beams are in phase and they interfere constructively. If a movable mirror is displaced by a distance of $\lambda/4$ the difference in path length becomes $\lambda/2$ which means that two beams are completely out of phase and they interfere destructively, thus moving the mirror at the constant velocity would cause the intensity of signal $I(\delta)$ measured as a function of the path length difference δ vary sinusoidally. Interference record can be expressed by equation 2.2 [44]:

$$I(\delta) = B(\bar{\nu}) \cos 2\pi\delta\bar{\nu} \quad (2.2)$$

Here $B(\bar{\nu})$ is an modified intensity of the source. As we see $I(\delta)$ simply represents the cosine Fourier transform of $B(\bar{\nu})$. Since movable mirror is usually scanned at a constant velocity v the difference in path length can be expressed as a product of velocity and time:

$$\delta = 2vt \quad (2.3)$$

Substituting this to the equation 2.2 we will get:

$$I(t) = I_0\{1 + \cos 2\pi ft\} \quad (2.4)$$

where f is given by:

$$f = 2v\bar{\nu} \quad (2.5)$$

By measuring intensity $I(\delta)$ one can extract $B(\bar{\nu})$, which is a trivial case for a monochromatic beam.

When the source is a continuum of wavenumbers, the interferogram can be represented by Fourier integral:

$$I(\delta) = \int_{-\infty}^{+\infty} B(\bar{\nu}) \cos 2\pi\delta\bar{\nu} d\bar{\nu} \quad (2.6)$$

and inverse Fourier integral:

$$B(\bar{\nu}) = \int_{-\infty}^{+\infty} I(\delta) \cos 2\pi\bar{\nu}\delta d\delta \quad (2.7)$$

The last equation is a main equation showing that in theory the exact form of the complete spectrum can be measured at any resolution. In practice the resolution is limited by finite sampling intervals and the range of scanning length of movable mirror[44].

The effect of finite scanning length is reflected in the Fourier transformed spectra as a convolution of two functions: the true spectrum $B(\bar{\nu})$ and the Fourier transform $g(\bar{\nu})$ of a truncation function $G(\delta)$ which depends the way one sets up the spectrometer. Mathematically this can be written in the following way:

$$B^*(\bar{\nu}) = B(\bar{\nu}) * g(\bar{\nu}) = \int_{-\infty}^{+\infty} B(\bar{\nu}') g(\bar{\nu} - \bar{\nu}') d\bar{\nu}' \quad (2.8)$$

The simplest expression for the truncation function is the so called boxcar function, e.g. step-like truncation at a certain distance Δ . As it turns out this type of function is not a good choice in many instances. For example, if one would like to resolve weak line in the spectrum very close to the strong main line, the weak feature will be obscured by modulation that is an artifact of the truncation function, because boxcar function yields $g(\bar{\nu}) \propto \text{sinc}\pi\bar{\nu}\Delta$ and it does not die fast enough away from $\bar{\nu}_0$. There are many functions that are used for the path length difference cut off in FTIR spectroscopy, called apodization functions, which does not suffer from this drawback. One function commonly used in many spectrometers is called the Happ-Genzel apodization function:

$$G(\delta) = 0.54 + 0.46 \cos \pi \frac{\delta}{\Delta} \quad (2.9)$$

Happ-Genzel apodization function as well as the other commonly used triangular apodization function can fully resolve peaks separated by $2/\Delta \text{ cm}^{-1}$, giving an advantage in resolution. In our experiments we measure absorbance $A(\bar{\nu})$ which is given by formula:

$$A(\bar{\nu}) = \log \frac{I_0(\bar{\nu})}{I(\bar{\nu})} \quad (2.10)$$

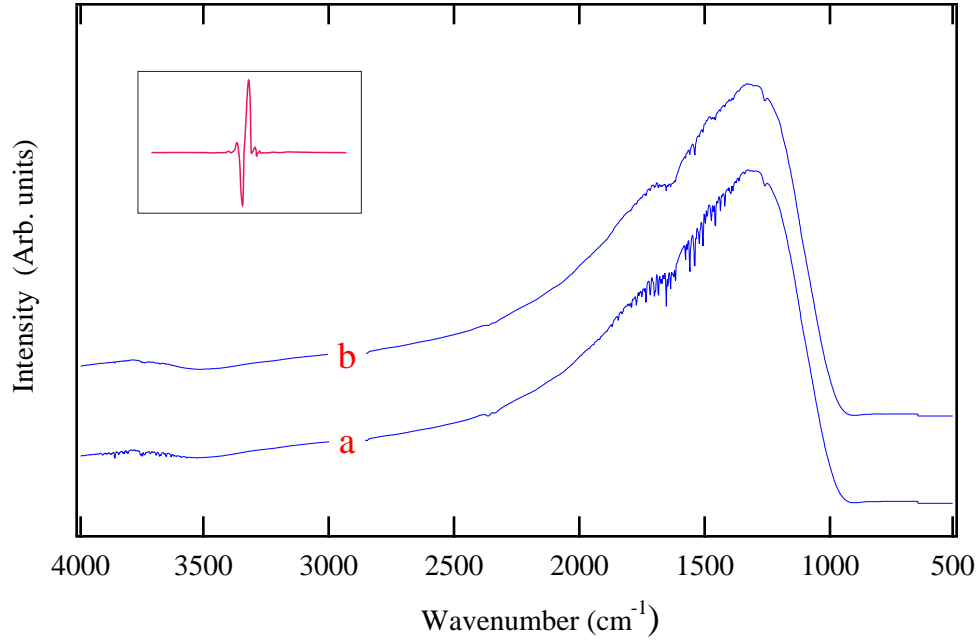


Figure 2.4: The interferogram (sub-window) and the single-beam FTIR spectrum: a) beam line is purged with dry air, b) beam line is not purged

where $I_0(\bar{\nu})$ is the intensity of radiation incident on the sample and $I(\bar{\nu})$ is the intensity of radiation transmitted to the detector.

For the absorbance measurements we used commercially available FTIR spectrometer (Nicolet model 752) set to direct the infrared beam to the UHV chamber equipped with the special windows (in and out ports), which were transparent to mid-infrared light. This infrared beam then was reflected from the sample surface, and the reflected signal was detected and analyzed using a liquid nitrogen cooled mercury-cadmium-telluride (MCT) detector. Mercury-cadmium-telluride alloy is a combination of a CdTe semiconductor material, with bandgap of approximately 1.5 eV at room temperature, and metallic HgTe mixture, from which a bandgap between 0 and 1.5 eV can be obtained. MCT detectors are commonly used for mid-infrared range of FTIR spectroscopy, where the amount of cadmium (Cd) in the mercury-cadmium-telluride alloy can be varied to tune the optical absorption of the material to the desired infrared wavelength [45, 46, 47]. An infrared photon detection occurs when a photon of sufficient energy

kicks an electron from the valence band to the conduction band. This electron is collected by a suitable external readout integrated circuit and transformed into an electric signal, which is further analyzed using fast fourier transform (FFT) methods and software provided by the spectrometer manufacturers.

The insert to figure 2.4 shows a typical interferogram, while the figure itself shows the single-beam spectrum collected using an FTIR spectrometer, which employs liquid nitrogen cooled MCT detector. As we can see from the figure, the spectrum contains strong absorbance lines of water vapor in the range of $1200\text{-}1900\text{ cm}^{-1}$, so purging the beam line with pure nitrogen gas or dry air is very important in order to resolve desired absorbance features and reduce changes in background noise.

2.4.2 Inverse Photoemission (IPE) Spectroscopy

Inverse Photoemission (IPE) Spectroscopy is a widely used experimental technique to examine the unoccupied electronic structure of surfaces and thin films [48, 49, 50, 51]. Together with the ultraviolet and x-ray photoemission spectroscopy techniques (UPS, XPS) [52, 53, 54, 55, 56], an angle-resolved inverse photoemission spectroscopy has played the dominant role in mapping energy bands of many clean and adsorbate-covered surfaces. IPE is an important measurement tool in our experiments, since, as we outlined in the introduction, investigation of unoccupied electronic states can provide valuable information about electronic properties of thin film systems and possible quantum size effects (QSEs) in them.

Figure 2.5 illustrates the idea of the inverse photoemission process, where a well collimated electron beam produced by the electron gun of the Stoffel-Johnson design [57], is incident on the sample. An impinging electron couples to an unoccupied state above the vacuum level and decays into a lower unoccupied state. A fraction of these

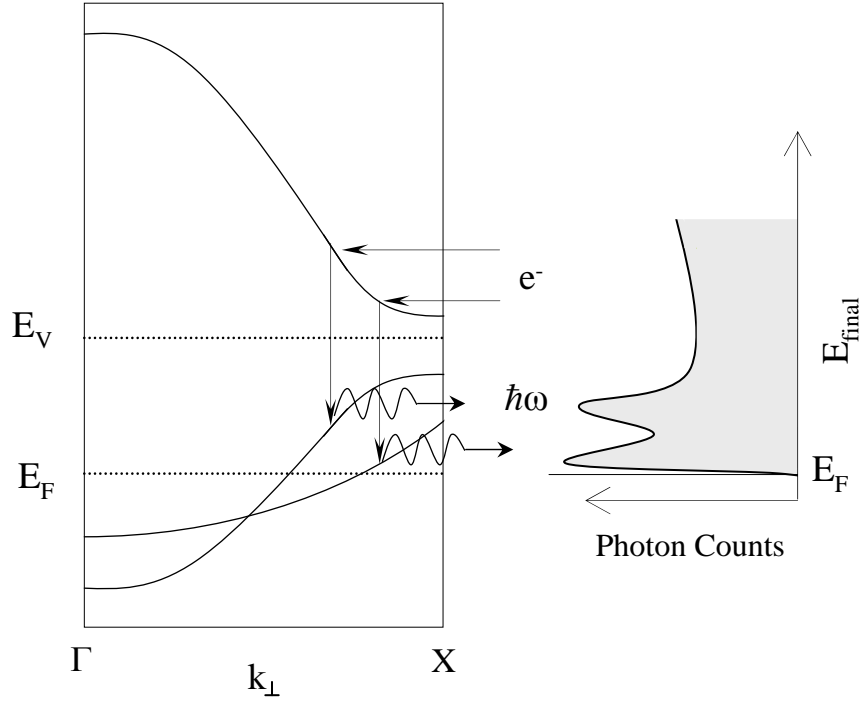


Figure 2.5: Illustration of the inverse photoemission process: An incident electron couples to an unoccupied state above the vacuum level and decays to a low-lying unoccupied state. A photon is emitted in the process.

decaying transitions are direct k -conserving transitions, which are resulting in a radiative emission. A photon whose energy equals the difference between the two states is detected and analyzed thereafter. IPE is a highly surface sensitive technique because it is operated at low incident electron energy (~ 20 eV). The inelastic mean free path (IMFP) of these electrons, which is a measure of the average distance travelled by an electron through a solid before it is inelastically scattered, is an order of a few monolayers ~ 10 Å [31].

The underlying principle of the IPE process is somewhat similar to time reversed photoemission, although final states are not identical in IPE and UPS. In UPS the

system of an initial $|N\rangle_{electron}$ state changes to a final $|N-1\rangle_{electron}$ state, while in IPE the system of an initial $|N\rangle_{electron}$ state changes to a final $|N+1\rangle_{electron}$ state. In case of metals, however, the electronic states are sufficiently delocalized and spread over multiple lattice sites, so the energy difference between $|N+1\rangle_{electron}$ and $|N-1\rangle_{electron}$ states becomes negligible, as N grows to a very large number.

The rate Γ , at which electrons undergo transitions from initial to final state in the IPE process can be obtained by treating the electromagnetic field as a perturbation to the ground state Hamiltonian of the electron system inside the crystal. Using formula for Fermis golden rule [58] would give us the following equation for Γ :

$$\Gamma \propto \frac{2\pi}{\hbar} \left(\frac{e}{mc} \right)^2 \left| \langle \Phi_f | \vec{A} \cdot \vec{p} | \Phi_i \rangle \right|^2 \delta(E_f - E_i + \hbar\omega) \quad (2.11)$$

where \vec{A} is the vector potential of radiative field, \vec{p} is the momentum of the electronic state, E_f is the energy of the final state, E_i is the energy of the initial state, Φ_f is the final state wave function and Φ_i is the initial state wave function. This expression for IPE transition rate is similar to the one obtained for UPS [59], however, the vector potential should be treated as quantized rather than classical field in inverse photoemission, since the photon is being produced during the process. Theoretical analysis show that the emission cross section per unit solid angle $d\sigma/d\Omega$ and the corresponding count rate in the inverse photoemission experiment is much lower compared to photoemission, due to the difference in wavelength of incident electron λ_e and photon λ_p [59]. The energy dependent cross section ratio of IPE and UPS process is given by equation:

$$\frac{d\sigma_{ipe}/d\Omega}{d\sigma_{ups}/d\Omega} = \left(\frac{\lambda_e}{\lambda_p} \right)^2 \quad (2.12)$$

As we can see for the typical electron and photon energies ($\sim 20\text{-}40$ eV) used in experiments this ratio is rather small, of the order 10^{-5} , meaning smaller count rates for IPE spectrometry and longer overall yield time for an experiment. Although this drawback in IPE is partially compensated by using a high incident electron flux and a large solid angle of photon acceptance.

During the inverse photoemission process photons of various energies are produced, which can be collected using either isochromat or spectrograph mode. In the spectro-

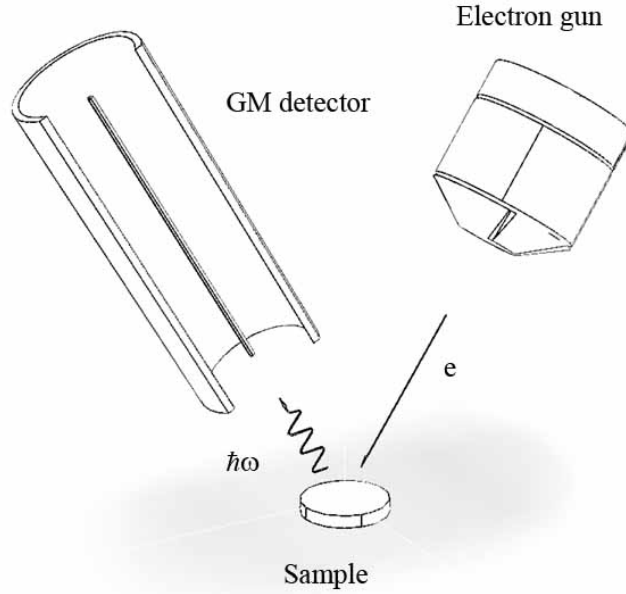


Figure 2.6: Schematics of IPE geometry: an electron beam produced by the electron gun is incident on the sample. The resulting photon is detected by the GM detector

graph mode, one should have a mono-energetic beam of incident electrons and use a diffraction grating to disperse the emitted photons that are in turn detected with a two-dimensional (2D) position sensitive detector over a range of different energies. When a photon strikes the detector, an electronic signal is generated that contains information about the position and thus the energy of the photon.

In the isochromat mode, which was the case for all IPE experiments described in

this thesis, the energy of the incident electrons is ramped and only those photons with a pre-defined energy (~ 9.5 eV) are detected. Figure 2.6 shows the geometry of an inverse photoemission experiment in the isochromat mode. As was already mentioned, in our experiments we employ an electron gun of Stoffel-Johnson design, which produces a beam of low energy ($E_i \leq 20$ eV) electrons directed at the sample. The electron gun cathode consists of a tungsten filament embedded in a low work function (2.1 eV) barium oxide (BaO). This allows the operation of the cathode at a relatively low temperature (~ 750 C), while reducing the thermal spread (~ 200 meV) in electron energies. Voltages in the gun extract, accelerate and focus the electrons to a small spot size of ~ 1 mm² on the sample [60]. Emitted photons are detected by an energy-selective Geiger Müller (GM) photon detector. The GM detector consists of a stainless steel discharge tube attached to the UHV chamber. The discharge tube is at ground potential and contains a center anode conductor that is maintained at ~ 320 V. A strontium fluoride (SrF₂) window is sealed to the end of the GM tube, allowing photons with energy less than 9.7 eV to pass through, thus providing the high energy photon cutoff for the spectrometer. The low energy cutoff is realized by using a mixture of Iodine gas at its room temperature vapor pressure ($\sim 6 \times 10^{-2}$ torr) and ~ 10 torr of Helium (He) gas held inside the stainless steel tube volume. The first ionization energy of the I₂ gas is 9.3 eV, so only photons with energy equal or higher of ionization energy of iodine can generate the discharge inside the tube. Following immediately after the $I_2 \longrightarrow I_2^* + e^-$ ionization process, created ions accelerate away from center anode, collide with other I₂ molecules on the way and create more ionized electrons. This way a single photon can cause a cascade of electrons, which hits the center anode and creates a negative dip in the positive anode voltage that is recorded. The number of discharges per unit time is proportional to the number of photons that penetrate into the tube during that time. Each pulse is recorded as a single count and the spectrum is taken by monitoring the number of counts as a function of incident electron energy. The

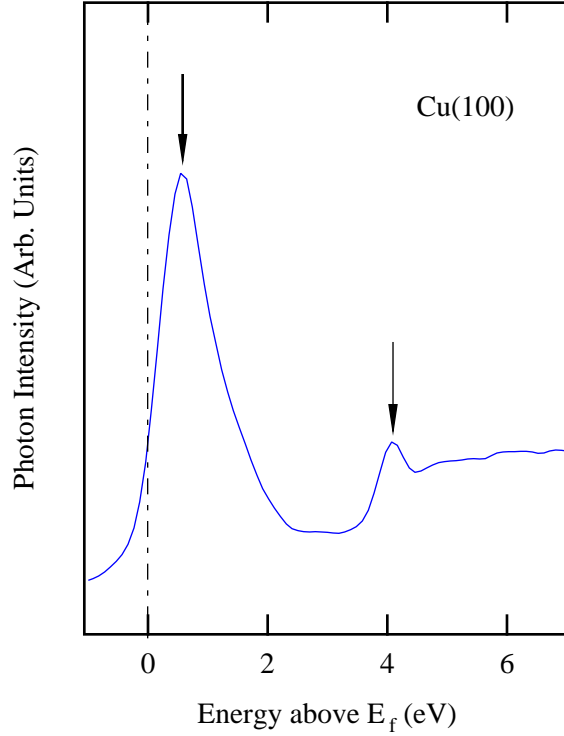


Figure 2.7: IPE spectrum from the Cu(100) single crystal.

combination of the SrF_2 window and I_2 gas thus makes the GM spectrometer sensitive to ~ 9.5 eV photons with a resolution better than 400 meV [30, 1, 61].

A typical IPE spectrum (photon intensity vs energy) is plotted on figure 2.9 taken from the clean Cu(100) single crystal surface. Energy scale is given with respect to Fermi energy $E_F = 0$. As we see the IPE spectrum of Cu(100) exhibits two features: First is a very intense feature at ~ 0.5 eV, which is associated with a bulk direct transition and a well defined Cu(100) image potential state near ~ 4.2 eV [62, 63]. A detailed discussion both of these features will be carried out in later chapters.

2.4.3 Temperature Programmed Desorption

Many surface science experiments involve different gas adsorbates, which cover the metal single crystal or thin-film surfaces, and it is crucial to extract information about

the bonding strength between gas molecules and a the surface. Temperature programmed desorption (TPD) is a very successful technique that can be used to assess these bond energies, especially for simple, non-dissociative adsorbates.

In a typical TPD experiment, the sample is exposed to some predefined amount of a high purity gas by back filling the chamber with the gas through a leak valve. The gas exposure can be controlled by controlling the chamber pressure and time of exposure, where the amount of exposure is usually measured in units of Langmuir ($1 \text{ L} = 1 \times 10^{-6} \text{ torr}\times\text{sec}$). The sample is then placed in front of a mass spectrometer and the temperature is then increased by passing a current through a tantalum filament at a controlled rate². During heating, the molecules begin to desorb from the sample surface and the desorption rate from the surface is monitored as a function of the sample temperature. In this way, a TPD spectrum is acquired.

The mass spectrometer houses a quadrupole mass analyzer that consists of four parallel metal rods aligned in a circle, with the opposing rods held at the same electrical potential. An oscillating voltage superimposed on a DC voltage is applied to each pair of rods. Ionized gas molecules from desorbing species travel through the quadrupole analyzer in between the rods and they are filtered based on their mass-to-charge ratio (m/q). Only ions of a certain m/q will reach the detector for a given voltage: others will have unstable trajectories and will eventually collide with the rods. This allows selection of an ion with particular m/q ratio in a fixed mass mode of the spectrometer, or one can scan a range of m/q -values by continuously varying the voltages on rods [64, 65]. In general, multiple bonding sites may be involved in the adsorbate-surface reaction and this will lead to a complex, multipeaked TPD spectrum, where peaks (T_D) indicate temperatures of maximum desorption rate.

A TPD measurement can begin with the sample at room temperature ($\sim 300 \text{ K}$) or at low temperature ($\sim 110 \text{ K}$). In the low temperature case, the sample is cooled

²The rate of heating in our studies is 1 K/s

down to 110 K using the liquid nitrogen cooled dewar with a copper cold finger, which comes to contact with the sample. The design of the sample holder minimizes the thermal contact between sample and surroundings, in order to avoid much heat loss. The temperature during TPD experiment is measured through a thermocouple which is pressed against the sample to keep it in direct contact.

Figure 2.8 shows a block-diagram of a TPD experiment. The programmable power supply is paired with a computer to control current to the sample and provide a response to temperature variance. A mass spectrometer control unit is also connected with the computer and set to detect desorbing species of defined mass(es). In our experiments

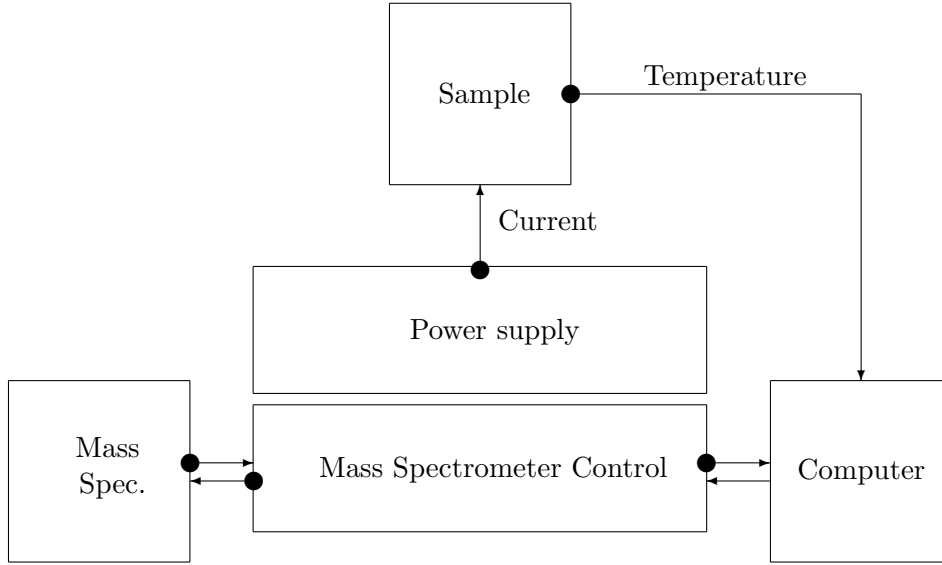


Figure 2.8: Schematic diagram for TPD experimental setup

we are most interested in the peak temperature (T_d) of TPD spectrum, since this is directly related to the bonding strength between the molecule and surface. Redhead [66] has shown that for a certain range of temperature, the relation between the activation energy for desorption E_{des} and desorption temperature peak T_d to a good approximation is given by the equation:

$$\frac{E_{des}}{RT_d} = \ln \left[\frac{\nu T_d}{\beta} \right] - 3.64 \quad (2.13)$$

where β is the rate of desorption, ν is the pre-exponential that characterizes the

molecule's desorption attempt frequency, R is the universal gas constant³ and T_d is the temperature. Equation 2.13 is called the Redhead equation and has been widely

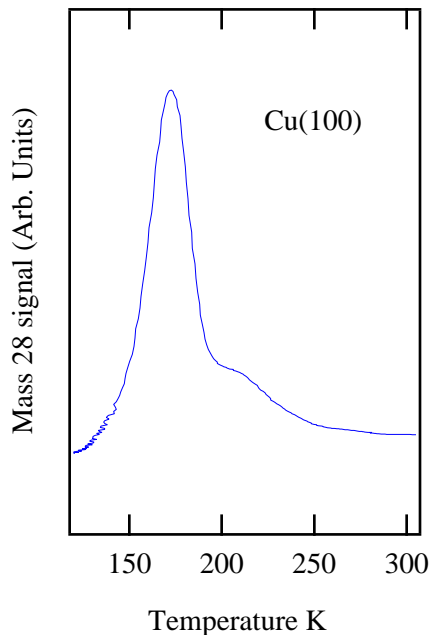


Figure 2.9: TPD spectrum obtained from the 1ML CO adsorbed on Cu(100) single crystal.

used to calculate the desorption energies E_{des} corresponding to each desorption peak T_d . As we are primarily interested in the qualitative changes of the molecule-surface bonding strength in all the experiments discussed in this thesis, T_d instead of E_{des} will be stated hereafter.

Figure 2.11 shows a typical TPD spectrum taken of CO desorbing from the Cu(100) surface. The main peak in the figure is attributed to desorption of CO adsorbed at the atop site of the Cu(100) surface, while the small shoulder on the high temperature side is attributed to CO desorption from step edges and defects [67].

³ $R = 8.3144 \text{ J mol}^{-1} \text{ K}^{-1} = 1.9872 \text{ cal mol}^{-1} \text{ K}^{-1}$

2.4.4 Low energy electron diffraction (LEED)

Low energy electron diffraction (LEED) is a standard surface physics technique used to qualitatively assess the order of crystal structure in the surface region [68]. In

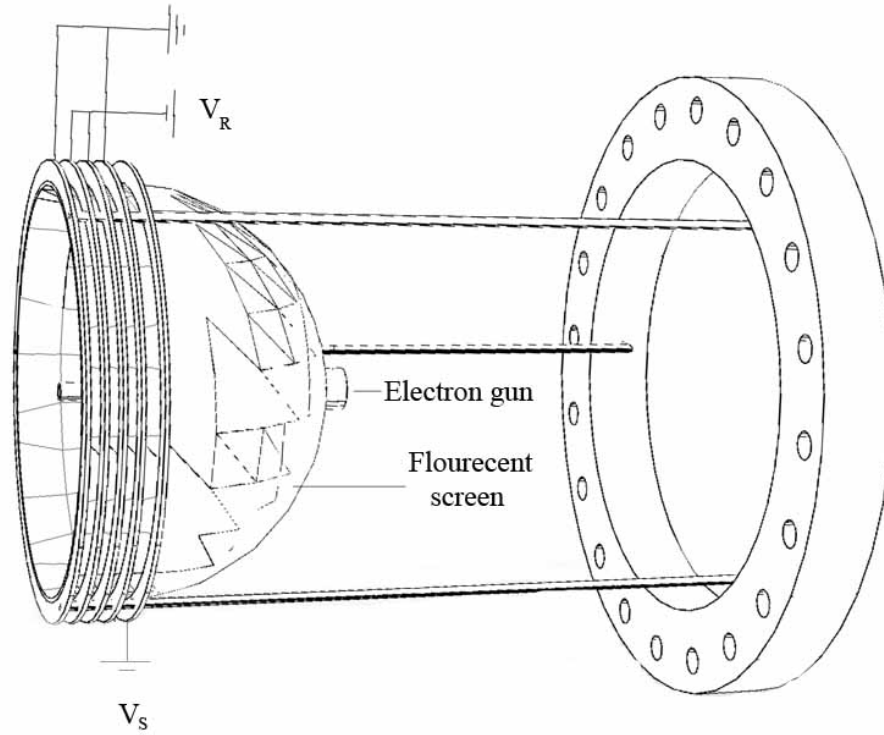


Figure 2.10: A schematic drawing of LEED.

a LEED experiment a monoenergetic, low energy beam of electrons is incident on the sample. Owing the short inelastic mean free path (IMFP) of $\sim 10\text{-}20 \text{ \AA}$, as mentioned in section 2.4.2, these electrons can not penetrate deep inside the crystalline bulk without suffering energy loss from inelastic scattering. Therefore, to a good approximation,

elastically scattered electrons come from the collisions with the 2D lattice of surface atoms. Elastically backscattered electrons are detected on the fluorescent, phosphor-coated screen. If the sample is well-ordered, a sharp interference pattern will be observed on the fluorescent screen. Because of the high surface sensitivity, which is on the order of few atomic layers, LEED is also useful in determining overlayer structures deposited on the surface and monitoring thin-film growth.

A schematic diagram of a LEED apparatus is shown in Figure 2.10. In a typical setup there are four concentric stainless steel mesh grids in front of the fluorescent screen. The first and forth grids are grounded, while a suppression voltage is applied on the second and third grids ($V_R \sim 20 - 50 \text{ V}$) to repel inelastically backscattered electrons. After passing this filter, the remaining electrons are accelerated in a strong potential ($V_S \sim 4\text{-}5 \text{ kV}$) imposed at the fluorescent screen, giving an intense, bright spot on the screen, where electrons interference constructively.

As was already mentioned, elastically scattered electrons mostly interact with the 2D lattice of surface atoms in LEED experiments, which means that direct lattice can be represented by two primitive lattice vectors parallel to the surface, while the primitive lattice vector perpendicular to the surface is considered to be infinite. This implies that the reciprocal lattice vectors lie in-plane, with no perpendicular component, so in three dimensions the reciprocal lattice would be an array of lines perpendicular to the surface.

At normal incidence, constructive interference of the elastically backscattered electron waves with momentum \vec{k} will occur when the deflected beams satisfy the Bragg condition given by the Eqn. 2.14:

$$\vec{k}_{\parallel} = \vec{G} \quad (2.14)$$

where \vec{G} is a surface reciprocal lattice vector and \vec{k}_{\parallel} is a momentum parallel to the surface. The corresponding LEED pattern would simply represent the reciprocal space image of direct 2-dimensional crystal lattice. This mapping of k-space is very useful to

understand the real space structure of the surface as well as orientation of the crystal which is necessary when performing other experiments like photoemission or inverse photoemission.

2.4.5 Auger electron spectroscopy (AES)

Auger Electron Spectroscopy (AES) is an experimental technique commonly used to identify the elements near the surface region of the probed sample and provide a rough estimate of their concentration. In this technique, a monoenergetic beam of electrons of ~ 3 keV energy is incident on the sample. Some of these electrons, due to their

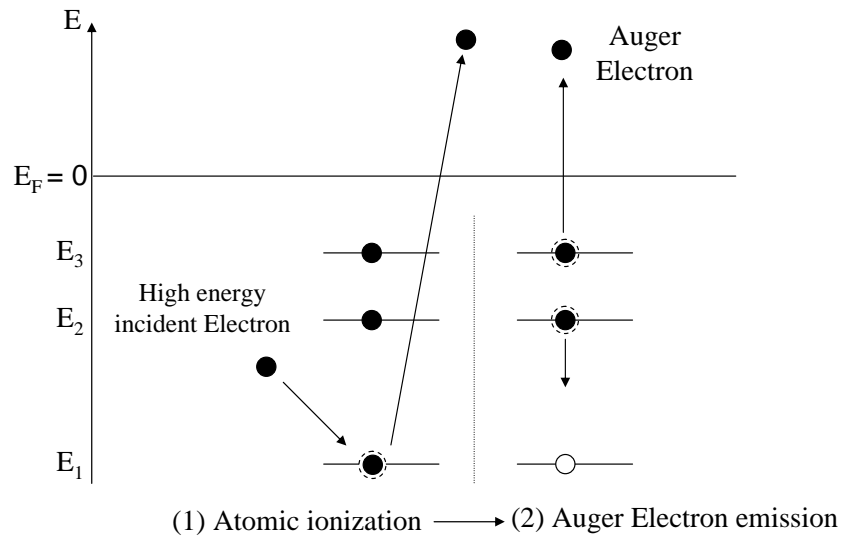


Figure 2.11: A schematic energy diagram of Auger process for an atom in a solid [1]

high kinetic energy, might eject core electrons from atoms located near the surface region. A core hole created in this process is filled with a higher lying core or valence electron, which has two possible routes to decay. One is a radiative transition, where, a photon of energy equal to the energy difference between the two levels is emitted as a result of conservation of energy. The second decay path is two-electron process, where

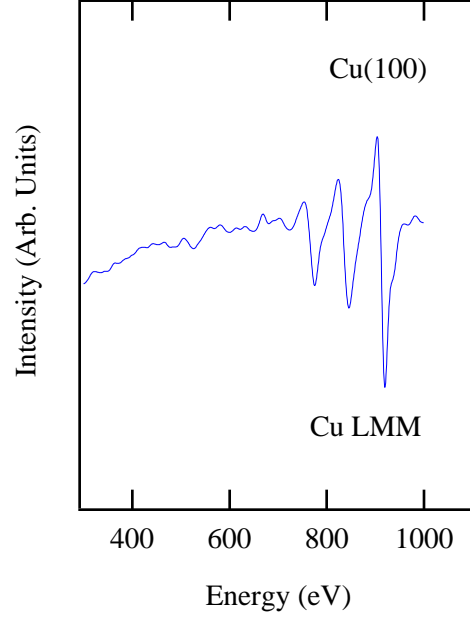


Figure 2.12: Auger spectrum of clean Cu(100)

one electron fills the core hole, while the excess of energy is carried away by a second electron known as the Auger electron. The Auger process dominates for core holes in the ~ 1 keV range and the short electron mean free path makes this technique very surface sensitive.

Fig. 2.11 shows a schematic energy diagram of Auger process. Here, E_1 is the binding energy of the core level, E_2 and E_3 are binding energies of the higher lying core or valence levels, and $E_F = 0$ is the Fermi energy. The Auger process is usually dominating for the electron core level energy range of few KeV. The kinetic energy E_k carried away with Auger electron is given by the equation:

$$E_k = E_2 - E_1 + E_3 - e\Phi \quad (2.15)$$

where Φ is the work function of the sample. As we see E_k is fully characteristic of the atomic levels of a given material and its detection uniquely determines the atomic species, which provides a way to monitor the surface composition and cleanliness of the sample. Furthermore the ratios of the intensities of Auger electron peaks can provide

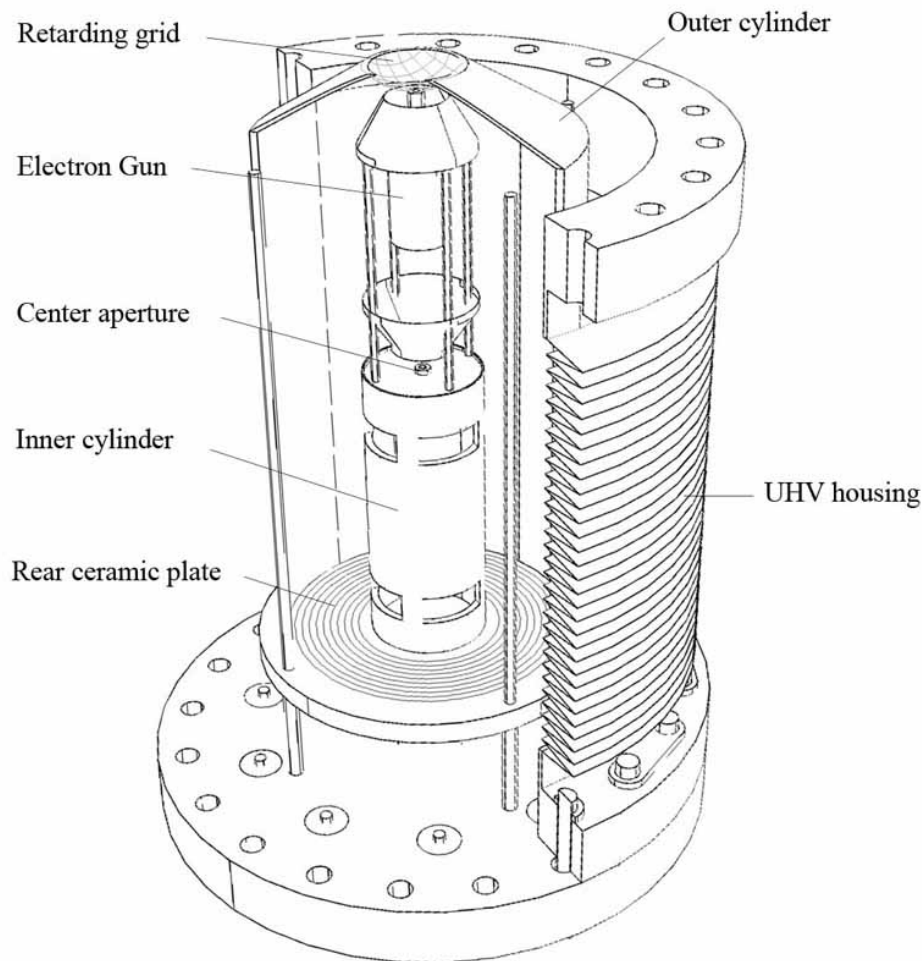


Figure 2.13: A schematic drawing of a double-pass cylindrical mirror analyzer (CMA).

a rough quantitative determination of the amount of surface elements. A particular Auger transition is described according to a spectroscopic three-letter notation. For example, the $L_{2,3}M_{4,5}M_{4,5}$ Auger transition of copper corresponds to an initial $2p$ core excitation, the filling of the remaining hole by a $3d$ electron, and the emission of another $3d$ electron as the Auger electron. Figure 2.12 shows Auger spectrum of clean Cu(100), where one can see characteristic copper $L_{2,3}M_{4,5}M_{4,5}$ transitions: Here the first letter indicates core hole origin, the second letter - origin of the relaxing electron and the

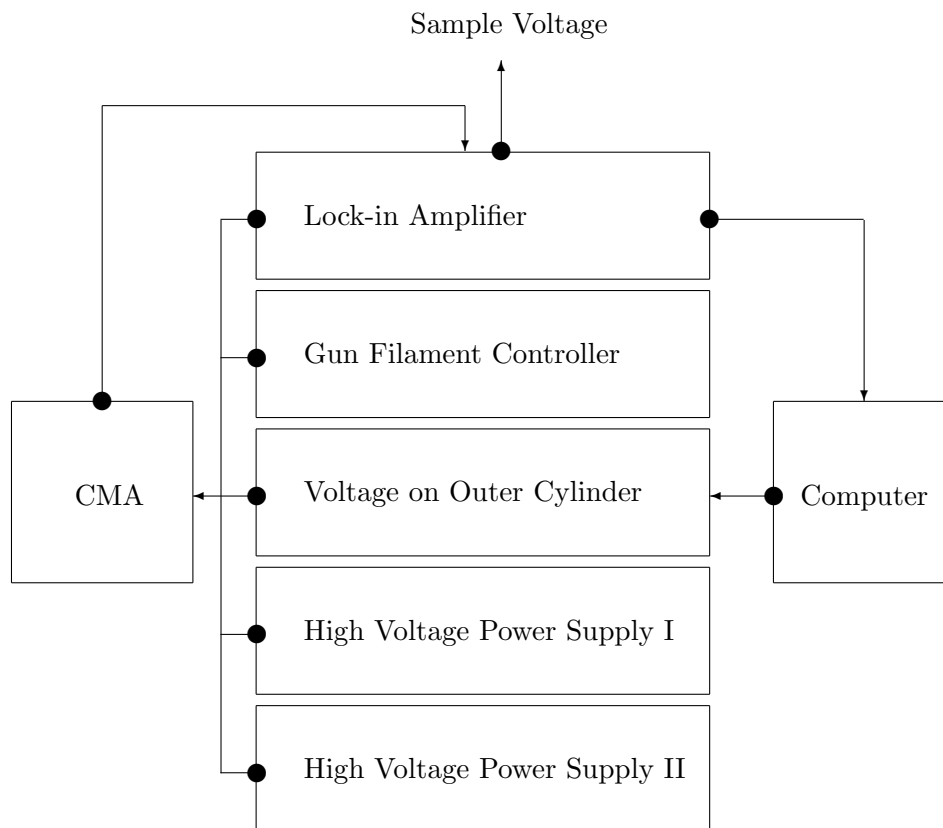


Figure 2.14: Schematics of Auger experimental setup

third letter - origin of the second hole (Auger electron).

A typical AES measurement uses an electron gun that directs the high-energy electrons at the sample. The energies of the resulting Auger electrons are then filtered and extracted by employing a double-pass cylindrical mirror analyzer (CMA) consisting of two concentric cylinders, a schematic drawing of which is shown in Fig. 2.13. The CMA working principle is based on electrostatic deflection of charged particles. Namely, its inner and outer cylinders are set to specific voltages so that only particles with certain energy can pass through the narrow aperture and reach the channeltron electron multiplier. An Auger electron energy spectrum can be obtained by ramping the negative voltage on the outer cylinder, while inner cylinder is grounded, and counting number of electrons at each particular energy. The Auger signal adds on a large background

of inelastically scattered electrons, which are produced from initial core excitation. In order to extract the Auger signal from this large background, a small sinusoidal voltage ($V=V_0 \sin \omega t$) is applied to the sample. This modulates the energy of Auger electrons and changes the current $I(E)$ reaching the channeltron, which can be written as Taylor expansion:

$$I(E + eV_0 \sin \omega t) = I(E) + eV_0 \sin \omega t \left(\frac{dI(E)}{dE} \right) + \dots \quad (2.16)$$

Since the energy distribution of inelastically scattered electrons is a relatively weak function of energy, they will contribute only to the constant background term in the Taylor expansion of the signal $I(E)$. A lock-in amplifier is used to measure the component of the current oscillating with frequency ω and its output gives the first derivative of the electron intensity as function of energy. This amplifies the signal proportional to the Auger electron intensity.

Figure 2.14 shows the schematic layout of the AES experimental setup. A double-pass CMA with the computer controlled outer cylinder voltage is installed in the UHV chamber. The oscillating component of the measured signal is decoupled from the electron multiplier and detected using the lock-in amplifier, which then outputs results to the computer. The amplitude of the modulation is chosen to yield a compromise between sensitivity and resolution.

2.4.6 Scanning tunnelling microscopy (STM)

One of the great advantages of scanning tunnelling microscopy (STM) is that it can provide direct, real space images of the surface, as well as probe the samples locally, unlike most surface science experimental techniques, which usually give very little information about the short-range order.

The operating principle of the STM, a detailed description of which can be found elsewhere [69, 70, 71], is based on the quantum mechanical phenomenon of tunnelling.

The tunnelling effect is the transmission of electrons through a vacuum barrier between two conductors when they are very close together. During its operation, the STM uses a

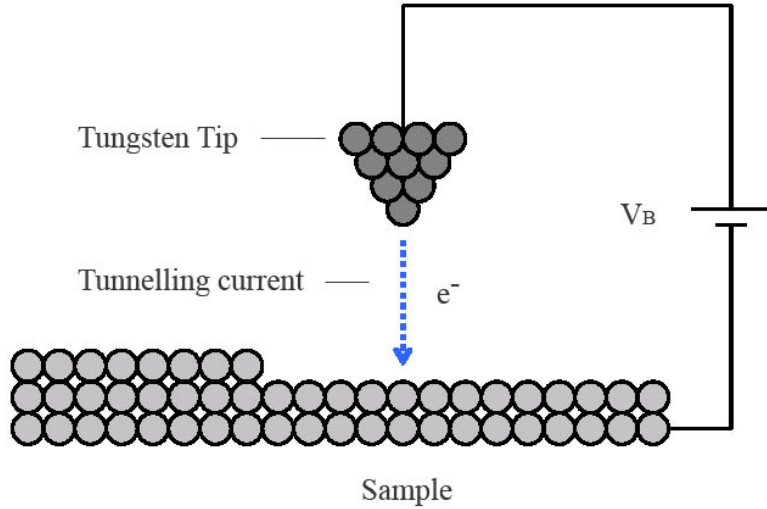


Figure 2.15: A schematic figure of an STM [2]

finely sharpened tungsten tip that is brought few Å away from the surface of the sample as it seen in the schematic diagram of Fig. 2.15. The tip position is controlled by a piezoelectric transducer, which is a ceramic positioning device that expands or contracts in response to an applied voltage. When the tip and the sample are connected with a voltage source, a small tunnelling current flows between the tip and sample surface. This current can be measured, and since its magnitude strongly depends on the distance between the tip and the surface⁴, the STM can be used to image surfaces of conducting materials with the atomic-scale resolution.

The experimental procedure for the STM measurements is the following: The initial approach of a tungsten tip to the sample takes place using coarse tip control electronics. Once tunnelling is established, the piezoelectric transducers are employed to move the tip in all directions. The special arrangement of transducers enables one to control the

⁴In the constant-current scanning mode the tip expected to follow the surface height to 0.1 Å or better [70]

motion of the tip with very high precision ($\pm 1 \text{ \AA}$). As the tip is moved laterally across the surface, the density of states, and therefore the tunnel current changes. This change in current, or the change in tip position can be measured, depending on the STM operation mode. Two modes are usually used in STM, called constant-height mode and constant-current mode, respectively. In the constant current mode, a feedback mechanism moves the tip up and down to maintain a constant tunnelling current, which leads to a height variation and the tip topography across the sample gives a constant charge density surface. In constant-height mode, the voltage and height are both held constant while the current changes. This leads to an image made of current changes over the surface, which can be related to charge density again. Scanning with constant-height mode is faster, as the piezoelectric movements require more time in constant-current mode than the voltage response in constant-height mode.

Due to the extreme sensitivity of the tunnel current to height, proper vibration isolation is very important for obtaining the reasonable results. In order to achieve this, a special spring systems should be used to keep the STM free from vibrations. Additionally, mechanisms for reducing tiny eddy currents that can affect tunnelling current should also be implemented. Maintaining the tip position with respect to the sample, scanning the sample in raster fashion and acquiring the data are all computer controlled. Various image processing software is also used for enhancing the obtained results.

The STM measurement described in this thesis were performed in a separate chamber consisting of a UHV Omicron VT Scanning Probe Microscope connected with UHV sample transfer to a sample preparation/analysis chamber. All STM measurements were performed at room temperature and images shown in this thesis were taken at positive or negative $\sim 2 \text{ V}$ tip bias and $\sim 1 \text{ nA}$ tunnel current, in a constant current tunnelling mode.

2.5 Summary

We have grown clean and well-ordered ultrathin metal films inside the ultrahigh vacuum chamber (UHV) chamber in the Laboratory for Surface Modification at Rutgers University. This custom built chamber contains different experimental tools for sample preparation, film growth and characterization. The preparation of a clean Cu(100) surface was done with sputtering and annealing techniques, and surface cleanliness was checked using Auger electron spectroscopy (AES) and the low energy electron diffraction (LEED) techniques. Iron, cobalt, nickel and copper thin-films were deposited using water cooled electron beam metal evaporation sources and film thickness was monitored with quartz crystal microbalance (QCM). Further analysis of MQW systems were accomplished by measuring unoccupied electronic structure using inverse photoemission (IPE) spectroscopy and different molecular adsorbates were probed with Fourier transformed infrared spectroscopy (FTIR), temperature programmed desorption (TPD) and scanning tunnelling microscopy (STM) experiments.

Chapter 3

Unoccupied states of fcc-Co/Cu(100) and CO chemisorption

3.1 Introduction

Obtaining an atomistic understanding of molecule-surface interactions is one of the main goals of surface science [72]. Studies of these interactions on well-characterized surfaces are typically limited to the high symmetry, low index surfaces of bulk single crystals that can be prepared in ultrahigh vacuum. In recent years, however, there has been considerable progress in the growth of epitaxial metal overlayers on metal substrates where the overlayer is several monolayers thick and is stabilized in a new crystalline phase [73]. With such systems, one can study surface phenomena of a crystal structure that does not exist for isolated single crystals at room temperature. Epitaxial films of this type often grow pseudomorphically, where the metastable phase adopts the crystal structure and in-plane lattice parameter of the underlying substrate. The metastable phase of the crystal structure occurs in many metallic alloys when a system reaches its equilibrium but is susceptible to fall into a lower-energy minimum with changing external conditions, such as temperature. In other words it is a local stability point of a system at a local (but not global) minimum of a potential and it lasts for a relatively long period of time. As the surfaces of such metastable structures have different interatomic spacings and local coordinations than that of the bulk single crystal surface, new molecule-surface bonding properties may be found. Quantum size effects (QSEs) play an important role in these systems, establishing the unusual properties

these structures exhibit. As we already have pointed out in Chap. 1, QSEs, namely the metallic quantum well (MQW) states are the key to understanding the giant magnetoresistance (GMR) effect. For epitaxial Co films on Cu(100), due to the contribution of the electrons from the Co $3d$ orbitals to the density of the states (DOS) at the Fermi level, the electronic structure is very complicated.

In this chapter, we will investigate the unoccupied electronic structure of the fcc-Co/Cu(100) system and CO chemisorption properties on it. The Co/Cu(100) system is an interesting example of a metastable structure, where the system forms metallic quantum well (MQW) states in the Co overlayer that change energy with overlayer thickness. These states are spin polarized and, in contrast to the more commonly studied Cu, Ag, or Au, the MQW states reside 1 eV or more above the Fermi level. Such high-lying MQW states are close in energy to the lowest unoccupied molecular orbital (LUMO) of the adsorbed species. In the case of CO, a typical test molecule in chemisorption studies, the LUMO is derived from the CO $2\pi^*$ orbital and plays a crucial role in backdonation of charge from the metal to the molecule when the chemisorption bond is formed. Therefore, varying the energy separation between MQW states and the CO $2\pi^*$ level may provide a new way to modify the strength of bonding between an adsorbate and the MQW surface.

The adsorption properties of the fcc-Co/Cu(100) system are studied with a variety of surface sensitive techniques, focussing on the influence of this metastable phase of Co on the CO adsorption properties [74]. The results will be compared to CO adsorption on the (0001) and (10 $\bar{1}$ 0) surfaces of single crystal hcp-Co [75], as well as Co monolayers grown on other metal substrates [76, 77, 78]. We have used inverse photoemission (IPE) spectroscopy to probe the electronic structure above the Fermi level, temperature programmed desorption (TPD) to obtain information about desorption rate as a function of temperature and Fourier transformed infrared (FTIR) spectroscopy to measure the vibrational frequencies of the adsorbed CO molecule and thus extract information

about molecule-metal interaction dynamics.

We compare the adsorption behavior of the fcc-Co(100) surface when it is exposed to CO at room temperature (RT) and at ~ 110 K. In both cases, CO adsorbs molecularly on the metal surface, but the FTIR spectra and TPD data show marked differences for low temperature and room temperature CO adsorption. In general, we find a desorption temperature that is significantly lower than what is reported in the literature for CO adsorbed on the low-index surfaces of hcp-Co [79], but there is also a dependence upon film thickness. Our results show important similarities and differences with recent studies [80, 81] of CO adsorption on another metastable system: fcc-Fe films grown on Cu(100).

3.1.1 Geometric structure

Before moving on to our study on the unoccupied electronic structure of ultra-thin cobalt films, it is worthwhile to give some of the basic knowledge about the differences between cobalt single crystal and thin film cobalt grown on Cu(100). It is well known that the equilibrium crystal structure of Co is a hexagonal closed packed (hcp) structure at room temperature. When grown on Cu(100), epitaxial Co films adopt a face centered cubic (fcc) crystal structure (Fig.3.1) of underlying substrate, which is strained to accommodate the $\sim 2\%$ in-plane lattice mismatch with the substrate. The resulting fcc-Co(100) surface is distinct from any hcp-Co surface.

Figure 3.1 shows the direct lattice of the fcc structure, bulk Brillouin zone and the surface Brillouin zone as a projection of the bulk Brillouin zone along the [001] direction. The critical points of the surface Brillouin zone are labeled as $\bar{\Gamma}$, which probes the Γ -X direction and \bar{X} , which projects to the L point of the bulk Brillouin zone. The unoccupied electronic structure of fcc-Co/Cu(100) has been studied with IPE [82, 83], and all features of the IPE spectra are well understood.

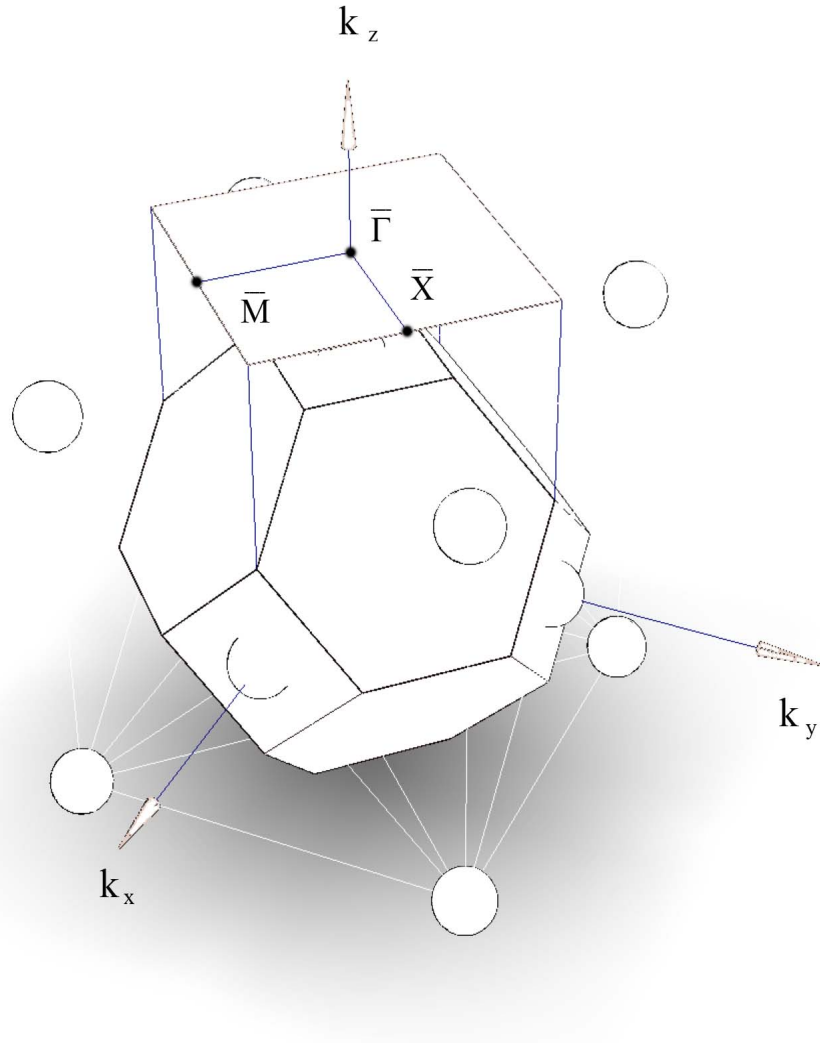


Figure 3.1: Direct lattice, reciprocal lattice and special points of the surface Brillouin zone (SBZ) of the face center cubic (fcc) crystalline structure.

3.2 Experimental Aspects

Our measurements were conducted using an ultra high vacuum (UHV) chamber that is equipped with a number of surface analytical techniques, primary of which are: Temperature programmed desorption (TPD), inverse photoemission (IPE), Fourier transformed infrared (FTIR) spectroscopy and low energy electron diffraction (LEED). The main

chamber, described in more detail elsewhere [84], also includes a load lock for rapid sample introduction, a standard ion source for sputter-cleaning the sample, electron beam metal evaporation sources, and a quartz crystal microbalance (QCM) to measure film thickness. The crystal monitor was calibrated using Rutherford backscattering spectrometry (RBS). The FTIR spectrometer (Nicolet model 752) employed an MCT detector and spectra were obtained in the frequency range of 4000-1000 cm^{-1} . In all cases, the reported spectra are an average of 1000 scans.

Inverse photoemission is an important technique for investigating electronic structure above the Fermi level [85, 86, 87]. All spectra reported here were obtained in the isochromat mode. A well collimated, monoenergetic electron beam, produced by an electron gun of the Stoffel-Johnson design [57], was directed towards the sample at normal incidence. Photons emitted from the sample were collected by a SrF_2/I_2 Geiger-Mueller (GM) tube that is sensitive to a narrow band of photon energies centered at $\hbar\omega = 9.5$ eV with resolution of $\Delta E = 400$ meV. A spectrum was obtained by sweeping the incident electron energy in the range from 5 eV to 15 eV and monitoring the intensity of photons at this fixed frequency.

The single crystal Cu(100) substrate was cleaned by cycles of sputtering (1 keV Ne^+ ions) and annealed to 750 K until we observed the expected IPE spectra from clean Cu(100) [83, 88] and a well-defined LEED pattern as shown in figure 3.2

Co was deposited using an electron beam evaporation source that employs high purity (99.995%) Co metal. The pressure during Co evaporation was typically 8×10^{-10} torr. The Co thickness was measured using the QCM which was mounted just below the sample and calibrated with Rutherford backscattering spectrometry to an accuracy of 0.1 ML. After depositing the desired number of Co monolayers at room temperature, the sample was annealed at 440 K for two minutes. In subsequent steps, the sample was never heated above this temperature. The absence of a strong 170 K desorption feature in CO TPD measurements, and the lack of a $c(2 \times 2)$ overlayer pattern in our

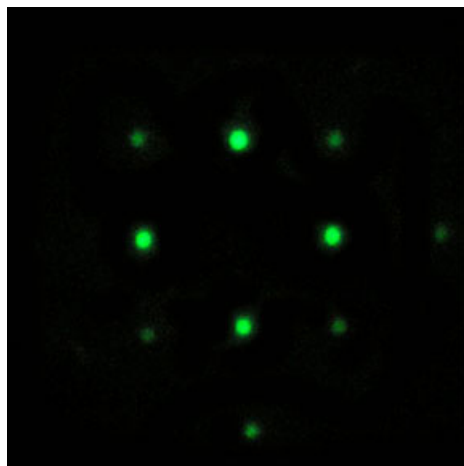


Figure 3.2: LEED pattern obtained at 68 eV from the clean Cu(100) surface.

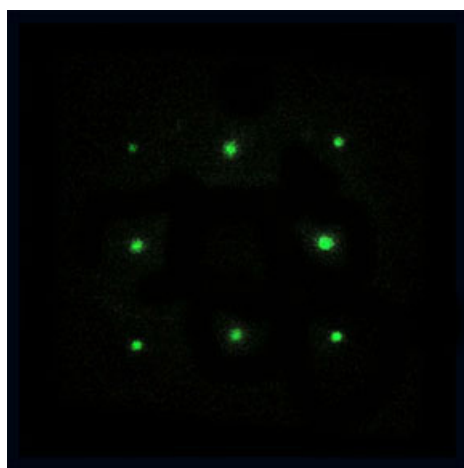


Figure 3.3: LEED pattern obtained at 68 eV from a 5 ML fcc-Co/Cu(100) MQW surface.

CO/Cu(100) LEED images indicates that after this procedure, the Cu coverage on the surface was very small¹ ($\Theta_{Cu} \ll 0.05$ ML). Exposure of the Co surface to CO, either with the sample at low temperature (~ 110 K) or at room temperature, was achieved by backfilling the chamber with CO gas at a fixed pressure in the range of $1 - 5 \times 10^{-9}$ torr. The total exposure was 1 Langmuir [L] ($1\text{L} = 1 \times 10^{-6}$ torr·s). Both the FTIR and TPD spectra show no significant changes above 0.5 L exposure, suggesting that a 1 Langmuir exposure to CO gas represents saturation coverage at both low and room temperatures.

3.3 Unoccupied States of fcc-Co/Cu(100)

The LEED pattern obtained from the surface of the 5 ML fcc-Co/Cu(100) system is shown in figure 3.3. The spots are slightly sharper than those from the Cu(100) surface in figure 3.2, in part owing to the higher Debye temperature of Co.

Figure 3.4 shows a series of IPE spectra obtained from the clean Cu(100) surface (bottom curve), and from fcc-Co films on the Cu(100) surface for Co MQW thickness ranging from 1 to 12 monolayer (ML). The dominant feature in inverse photoemission spectrum obtained from Cu(100) is a bulklike transition into copper *sp* states. There is another well defined peak near ~ 4.2 eV, This feature is associated to a well known Cu(100) image potential state [62, 63]. Image potential state appears when an electron approaches a metal surface and it's screened by the conduction electrons of the metal. A positive charge inside the metal forms a mirror image of an electron with a positive charge. An attractive potential between the electron and its positive image inside the metal leads to a potential well formation in between the repulsive barrier associated with a bulk band gap on the crystal side, and the imagelike part of the surface barrier on the vacuum side. The bound states confined in the well are called image potential

¹When a 5 ML Co film was intentionally annealed a higher temperature (*e.g.*, 550 K), or if a small amount (~ 0.05 ML) of Cu was deposited on the surface, exposure to 1L of CO at 110 K yielded a well-defined $c(2 \times 2)$ LEED pattern and a pronounced desorption feature at 170 K (See section 3.4.1)

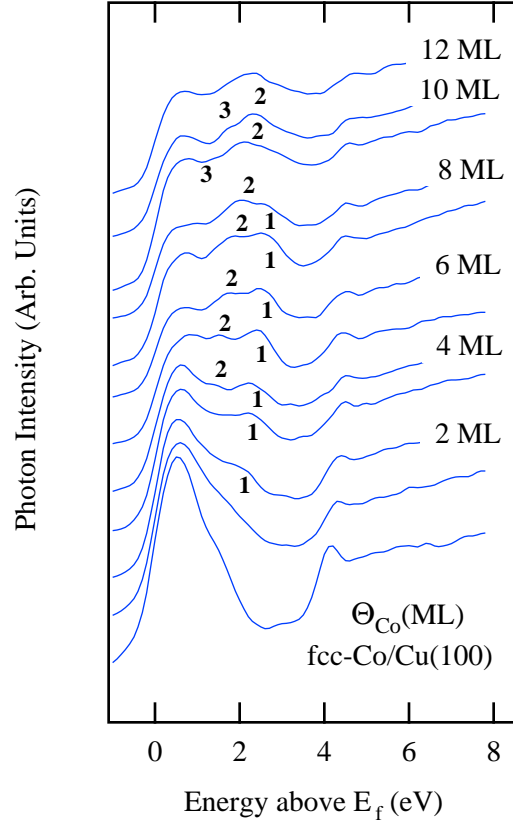


Figure 3.4: IPE spectra of clean Cu(100) and fcc-Co/Cu(100) for different Co thickness. Numbers indicate different MQW state features.

surface states, which normally are unoccupied. Image-potential states should occur on all metals, provided they are located energetically within a gap of the projected bulk-band structure. This gap prevents the electrons from penetrating into the crystal and traps them outside the surface [89]. The position of the image potential state in the IPE spectrum is very sensitive to the composition of the top layer, and to surface order and flatness, as a result, it is a very good qualitative assessment of surface quality [90]. For all thin film experiments reported in this thesis, we started by obtaining a high quality² IPE spectrum of clean and well ordered Cu(100) single crystal surface first to ensure the consistency in our energy calibration. As we deposit cobalt layers,

²Under definition of a “high quality” Cu IPE spectrum we imply a well defined main *sp* transition peak with high count rate, a sharp image potential state and a lower background *etc.*

the sp transition feature from Cu(100) is quenched and a cobalt minority spin indirect transition into d state appears in spectrum. According to Ref.[83] empty d states exist only for the minority spin cobalt and no direct transitions are allowed as a result of selection rules and energy conservation. Although indirect transitions are still possible and have a quite high intensity because of high density of empty d states near the Fermi level.

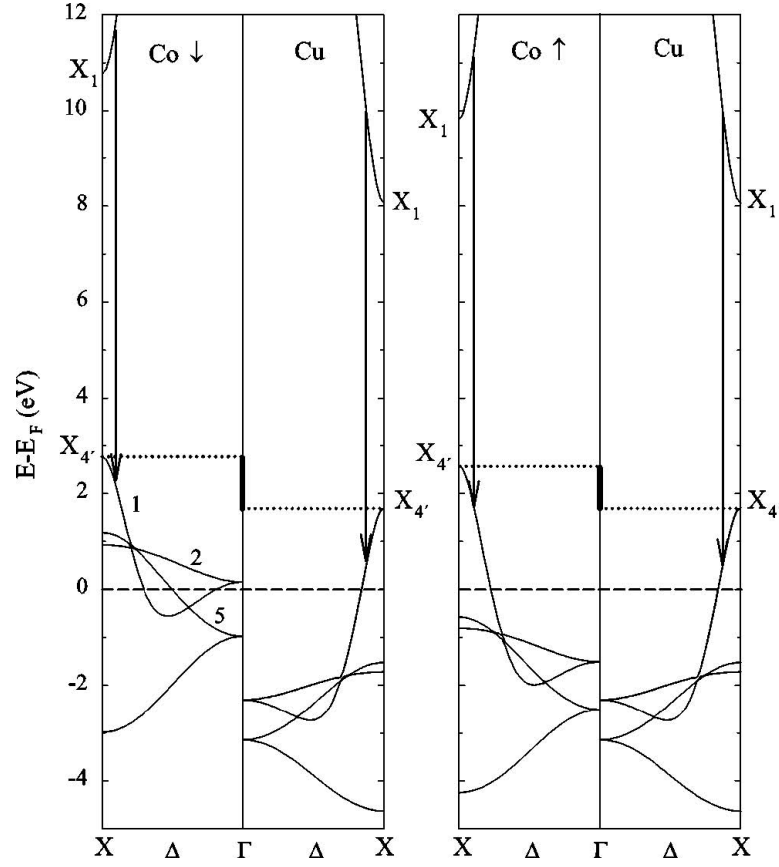


Figure 3.5: Comparison of energy bands $E(\mathbf{k})$ along the $[100]$ direction ΓX for minority and majority spin cobalt and copper. Vertical arrows indicate direct optical transitions relevant in IPE measurements [83]

For a Co film thickness of 2 ML, a new feature, labeled (1), is observed at 2.1 eV above the Fermi level, and this feature moves towards higher energy as the overlayer thickness increases until 9 ML where it no longer is distinct. At a Co thickness of 4 ML, a second feature, (2), appears at 1.4 eV above E_F , also moves to higher energy

with increasing Co thickness, and is observed at 2.4 eV for a 12 ML thick film. At 9 ML and above, a third feature is also seen. Features (1), (2), and (3) are identified as MQW states of the Co overlayer, and the behavior of these spectral features agrees with what was found in an earlier study of this system [83]. As expected, these MQW states are the result of cobalt bulklike *sp* band quantization. Figure 3.5 shows a spin resolved comparison of the calculated energy band along the [100] direction for fcc-Co and Cu [83]. As we see from the figure, along the [100] direction, from $X_{4'}$ to X_1 the bulk electronic structure exhibits a Shockley inverted energy gap for electron momenta. The values of $X_{4'}$ and X_1 points of Cu are 1.8 eV and 8.1 eV respectively. Electron transitions occur near the X point and for features (2) and (3) the energy is lower than for the Cu $X_{4'}$ point (figure 3.5), so in this case we do not have true MQW state, but a quantum well resonance overlapping with substrate bulk state continuum. Although a number of MQW states are seen, as they all occur well above E_F , they have little influence on the density of states at the Fermi level. The image potential state for cobalt thin films also shifts to slightly higher energy as work function changes cobalt films compared to copper.

Figures 3.6 (a), and 3.6 (b) show a series of IPE spectra obtained from a 2 and 5 ML fcc-Co MQW system when the surface is exposed to increasing amounts of CO at a temperature of ~ 110 K. Compared to the clean spectrum, we find that the characteristic MQW states appear to be strongly suppressed upon exposure to CO. An energy shift of this sort was observed for CO adsorption on other MQW systems [91] and is attributed to changes in the surface potential. When the sample has received a CO exposure of 0.2 L, the MQW states are no longer observable and emission from the unoccupied Co $3d$ levels [83] just above the Fermi level is more easily seen. Upon increasing exposure, a strong but broad feature centered at 4.4 eV above E_F is seen. This is attributed to emission from the CO $2\pi^*$ level, similar to what is observed for molecular CO adsorption on other transition metal systems [92, 93].

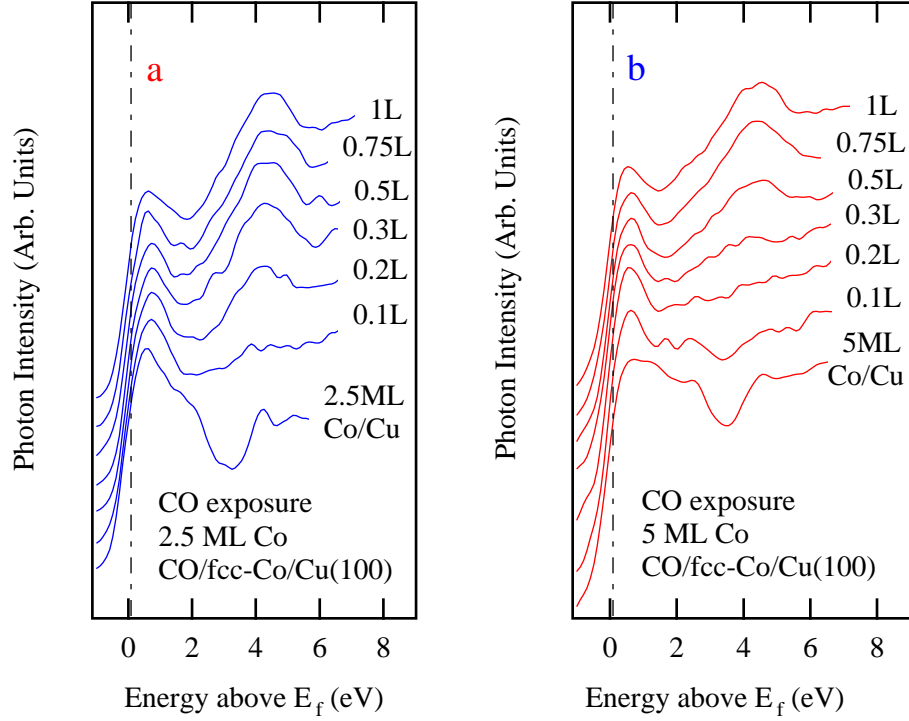


Figure 3.6: IPE spectra from the CO/ n -ML fcc-Co/Cu(100) system for different CO exposures at a temperature of 110 K.

3.3.1 Phase Accumulation Model (PAM)

An important aspect of the MQW system is the change in the energy and the number of quantized electronic states that occurs when the thickness of the MQW layer is varied. As expected from a simple square well problem, the energies of the states move downward and a new bound state may appear near the top of the well with the increasing width of the well. In the transition metal systems under consideration here, the \mathbf{k} vector of the MQW states is nearly at the Brillouin Zone boundary. As a result, when increasing the film thickness, the boundary conditions can be satisfied by a state with one additional node and with a slightly larger \mathbf{k} vector. Therefore, the MQW states, characterized by the quantum number $\nu = m - n$, (where m is the number of ML, and n is the number of nodes), moves to higher energy with increasing film thickness.

The Phase Accumulation Model (PAM) has been proved to be a very simple and successful approach to model electron confinement, simulate density of states and understand the formation of MQW states [94]. The idea behind the PAM is that an electron will be confined in thin film if following criteria is met: the total phase accumulated by the electron wave function in a round trip of the well is an integer multiple of 2π . The total phase includes the phase shifts upon reflection from the interface between the film and the substrate and/or vacuum, and the phase accumulated in a round trip of the film:

$$\Delta\varphi_V + \Delta\varphi_C + 2mak_{\perp} = 2\pi n, \quad (3.1)$$

where $\Delta\varphi_C$ and $\Delta\varphi_V$ are the phase shifts upon reflection from the vacuum-film interface and the film-substrate interface, respectively, and the term $2mak_{\perp}$ is the phase accumulated inside the cobalt film layer, where a is the thickness of one monolayer of the cobalt film (1.8 Å), m is the number of monolayers, n is an integer and k_{\perp} is the electron's momentum perpendicular to the surface. The variables $\Delta\varphi_V$, $\Delta\varphi_C$ and k_{\perp} are all functions of energy. Having all three phase terms expressed as the function of energy with the same energy reference ($E_F = 0$ in my case), we can rearrange equation 3.1 as:

$$2mak_{\perp} = 2\pi n - \Delta\varphi_V + \Delta\varphi_C, \quad (3.2)$$

and calculate the MQW state energies by graphically solving equation 3.2. MQW states disperse up with film thickness, which can also be understood through the simple math shown below, where we substitute m and n in Eqn. 3.2 with $m+1$ and $n+1$ respectively:

$$2(m+1)a(k_{\perp} + \Delta k_{\perp}) = 2\pi(n+1) - \Delta\varphi_V + \Delta\varphi_C \quad (3.3)$$

By subtracting equation 3.2 from equation 3.3, we will get:

$$\Delta k_{\perp} = \frac{\pi - ak_{\perp}}{(m+1)a} = \frac{1}{m+1}(k_{BZ} - k_{\perp}) \quad (3.4)$$

Here, $k_{BZ} = \pi/a$ is the k value at the Brillouin Zone boundary. In our case, since $k_{\perp} < k_{BZ}$, equation 3.4 should always give out a positive value. That is to say, the

energy of a MQW state moves up with increasing film thickness. The spectra in fig. 3.4 clearly illustrates this behavior in a series of inverse photoemission spectra. The features indicated by the tick marks (1), (2), (3) are MQW states. We see that the energy of a given state increases with increasing thickness, saturating at ~ 2.8 eV above the Fermi level, which is the band edge (the X_1 point) of cobalt. Figure 3.7 illustrates the phase changes in the PAM.

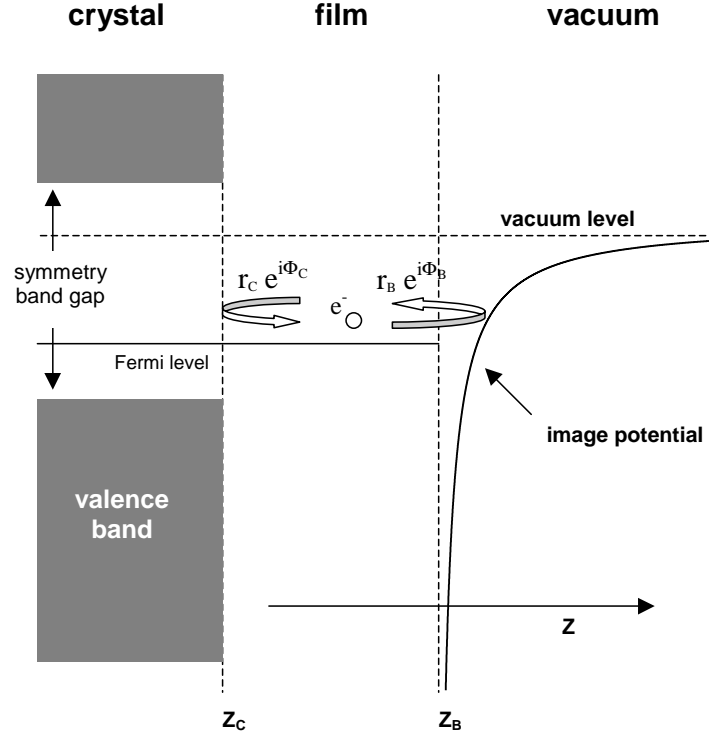


Figure 3.7: Schematic drawing of PAM model [95]

To solve the PAM Eqn. 3.2 we first need to calculate the phase shift terms $\Delta\varphi_V$, $\Delta\varphi_C$ and $2mak_\perp$ as a function of energy. Here $\Delta\varphi_V$ can be calculated within the WKB approximation [96] and is given by the following expression:

$$\Delta\varphi_V = \pi \left[\frac{3.4 \text{ (eV)}}{E_V - E} \right]^{1/2} - \pi \quad (3.5)$$

where $E_V \sim 5$ eV is the vacuum level energy of cobalt relative to Fermi level. In order to simplify the PAM calculation we ignore small changes in work function with increasing

film thickness. $\Delta\varphi_C$ is the phase shift upon reflection from the Cu(100) substrate, and the following equation has been widely used [97, 98, 94] to calculate $\Delta\varphi_C$ for different MQW systems:

$$\Delta\varphi_C = \begin{cases} -\pi & E < E_L \\ 2 \arcsin [(E - E_L)/(E_U - E_L)]^{1/2} - \pi & E_L < E < E_U \\ 0 & E > E_U \end{cases} \quad (3.6)$$

where E_U and E_L represent the upper and lower edges of the band gap. For fcc-Co/Cu(100) case, the band gap corresponds to the energy difference between the copper X'_4 and X_1 points. The corresponding calculated values of E_L and E_U for Cu(100) are 1.8 eV and 8.1 eV with respect to Fermi level. Within the framework of a two-band nearly free electron (NFE) model approximation [99], from which equation 3.6 was derived, the phase $\Delta\varphi_C$ changes by π each time it traverses the given band gap [100, 101]. In other words for band gaps which occur higher in energy, the phase $\Delta\varphi_C$ would be modified by the multiples of π depending on the hierarchy and order of bands. As we see the band gap we are dealing with is the Shockley-inverted gap above the X'_4 band edge of copper, unlike the case in Ag/Fe(100) [94] or Cu/Fe/Cu(100) [30] system, where the band gap of interest was the hybridization gap below the X'_4 point. Considering this fact as an influential factor on phase shift, Eqn. 3.6 will be rewritten with an additional π as follows:

$$\Delta\varphi_C = \begin{cases} 0 & E < E_L \\ 2 \arcsin [(E - E_L)/(E_U - E_L)]^{1/2} & E_L < E < E_U \\ \pi & E > E_U \end{cases} \quad (3.7)$$

In order to get an expression for energy-momentum dispersion we can apply the two-band nearly free electron (NFE) model in our calculations. The conditions under which two-band NFE model works are close to conditions where MQW states usually occur, e.g. when momentum k is close to the single bragg plane.

The energies in the two-band NFE model are given by the equation:

$$\text{Det} \begin{pmatrix} (\hbar^2/2m_e^*)\mathbf{k}^2 - E & V_g \\ V_g & (\hbar^2/2m_e^*)(\mathbf{k} - \mathbf{g})^2 - E \end{pmatrix} = 0 \quad (3.8)$$

where \mathbf{g} is a reciprocal lattice vector, m_e^* is an effective mass of electron and $2V_g$ is a band gap. In one dimensional case, when \mathbf{k} is perpendicular to the film, it is easier to solve 3.8 by substituting

$$k \longrightarrow \frac{g}{2} - q. \quad (3.9)$$

After some simplification eq. 3.8 can be written in the following form:

$$\left(\frac{\hbar^2}{2m}\right)^2 \left\{ (A - qg)(A + qg) \right\} - V_g^2 = 0 \quad (3.10)$$

where

$$A = q^2 + (g/2)^2 - 2mE/\hbar^2. \quad (3.11)$$

Solving quadratic equation with respect to q^2 gives:

$$q^2(E) = \frac{2m}{\hbar^2} \left\{ E + E_g - \sqrt{4EE_g + V_g} \right\}. \quad (3.12)$$

In this notation

$$E_g = \left(\frac{\hbar^2}{2m}\right) \left(\frac{g}{2}\right)^2. \quad (3.13)$$

Recall that while solving equation 3.8 we changed variables (see eq. 3.9). Now going back to the old k , we get our final expression:

$$k(E) = \sqrt{\frac{2m}{\hbar^2}} \left(\sqrt{E_g} - \sqrt{E + E_g - [4EE_g + V_g]^{1/2}} \right). \quad (3.14)$$

Using the formula derived above for energy-momentum dispersion and the same $\Delta\varphi_C$ and $\Delta\varphi_V$ expressed as a function of energy, we can get a graphical solution to eq. 3.2. Figure 3.8 shows the graphical solution to equations 3.2 for a series of integer m and n values. In each of these graphs the thicker (red, if in color) curves show the energy dependence of the $2mak_{\perp}$ component of the phase for different film thicknesses

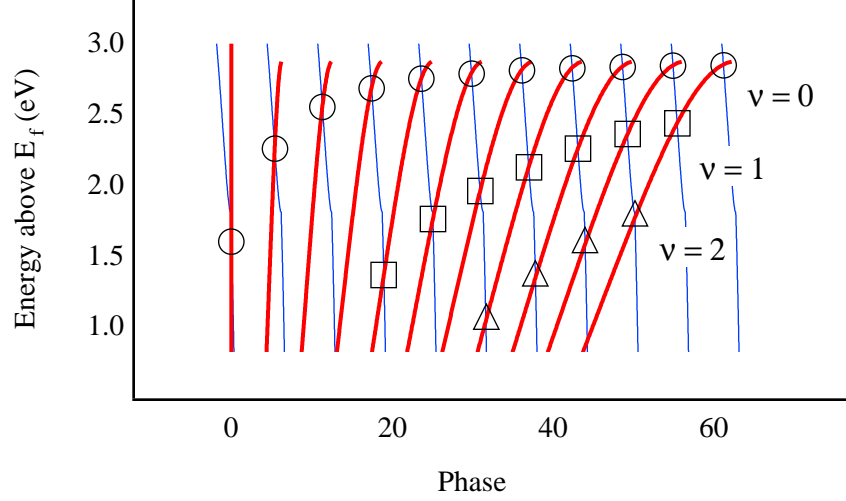


Figure 3.8: PAM calculation results: phase vs energy for different thicknesses and wavefunction nodes

(m ML), while the thinner (blue, if in color) curves show the sum $(2\pi n - \Delta\varphi_V + \Delta\varphi_C)$. The crossing points of the two sets of curves yield the energies of the MQW states. The MQW states are categorized according to the difference between the number of atomic layers in the film m and the number of nodes in the wavefunction within the film perpendicular to the surface (which equals n). From figure 3.8, we can see three different quantum well states labeled as $\nu = 0$ (circles), $\nu = 1$ (boxes) and $\nu = 2$ (triangles) respectively. We compare the PAM calculation results with our IPE spectra by plotting the energies of different calculated MQW states together with experimental MQW IPE peaks *vs.* film thickness, as illustrated in figure 3.9. As we see from figure 3.9, MQW states with lower energy (features indicated by solid boxes and triangles) are consistent with the $\nu = 1$ and $\nu = 2$ PAM calculated MQW states, which move up in energy with increasing cobalt film thickness. The high energy feature (solid circles) from IPE measurements which corresponds to $\nu = 0$ state, does not agree with PAM calculated results very well. The calculated result suggests flat dispersion for thicker films, while measurements show upward dispersion in energy. At this point subtle analysis using more complex theoretical models than the NFE approximation is required to get better

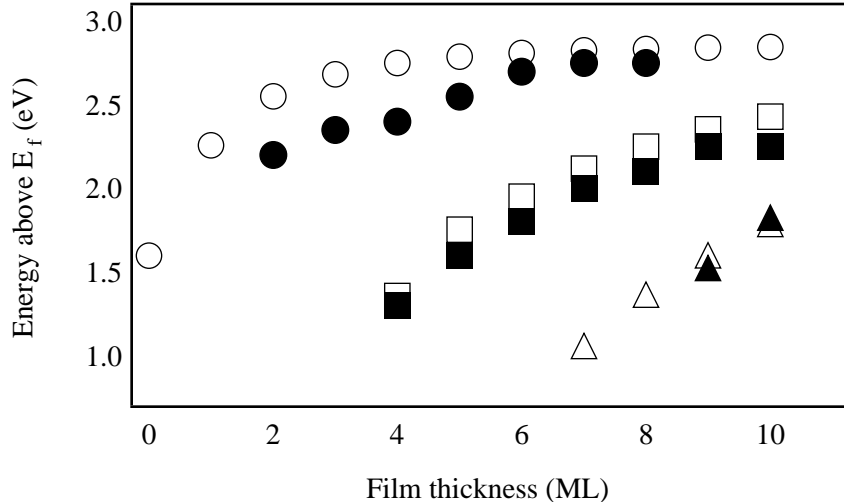


Figure 3.9: Comparison between the PAM calculation results and the IPE experimental results: solid circles, squares and triangles correspond to experimental values for $\nu = 0$, $\nu = 1$ and $\nu = 2$ respectively. Open circles, squares and triangles represent corresponding PAM calculated values.

agreement with experimental results.

3.4 CO adsorption: Results and Discussion

Although a detailed understanding of CO bound to a transition metal surface would require first principles electronic structure calculations, the essential aspects of the bond can be understood using the Blyholder model [102, 103, 104]. In this picture, the CO-transition metal (TM) bond is mediated by charge donation from the 5σ orbital of the molecule to the metal, accompanied by backdonation from the d -levels of the metal to CO $2\pi^*$ molecular level. As the $2\pi^*$ orbital is antibonding with respect to the carbon - oxygen bond, this backdonation causes a redshift in the frequency of the C-O stretch vibrational mode. This redshift is an indicator of CO bond strength on particular sites, i.e. farther the frequency is redshifted from unsupported CO molecule vibrational mode, stronger is a molecule-metal bond, so the intermolecular CO stretch frequency gives an idea about the type of adsorption site occupied by the molecule.

In general there is an additional coverage dependant shift of the CO vibrational frequency. It is important to understand that the CO molecule vibrational frequencies supported by transitional and/or noble metal surfaces partially lose their localized character due to the interaction between the molecules. Such collective behavior of vibrational excitations of the adsorbed molecules resembles the phonon modes in solids and can be described by a wave vector \vec{q} and interaction potential $U(\vec{q})$. In the present work we assume that the vibrating CO molecules interact with each other through their oscillating dipole fields, which is frequently called a dipole-dipole interaction. Within this assumption theoretical calculations have been conducted, giving expressions for $U(\vec{q})$ and infrared light reflectance $\Delta(\omega)$ [105, 106]. The predicted change in frequency $\Delta\omega$ is positive, which implies upward shift in frequency with increasing CO coverage. Although the theory of dipole-dipole interactions gives the correct direction of frequency shift for most instances, quantitative theory predictions are somewhat small compared to experimentally observed ones [107, 108]. To improve quantitative results the theory can be corrected within the framework of the Blyholder model mentioned above, saying that there will be increased competition for back-donating metal electrons to the CO $2\pi^*$ between increasing numbers of adsorbed molecules. This will reduce the occupancy of the CO $2\pi^*$ orbital for individual molecules and give rise to additional blueshift in vibrational frequency, often referred to in the literature as "chemical shift" [109].

Infrared spectroscopy measurements indicate that CO adsorption on this surface is more complicated than the IPE results might suggest. Figure 3.10 shows a series of FTIR spectra in the region of the CO stretch vibration for the 5 ML Co/Cu(100) MQW system as a function of increasing CO exposure. For the lowest exposures, the spectrum is dominated by a peak at 1974 cm^{-1} and a small shoulder at 1936 cm^{-1} . As the CO exposure increases through 0.15 L, the intensity of the high frequency peak increases and its frequency shifts to $\sim 1998\text{ cm}^{-1}$ in a monotonic fashion. At an exposure of 0.2 L, the main peak has shifted to 2005 cm^{-1} and becomes asymmetric with intensity

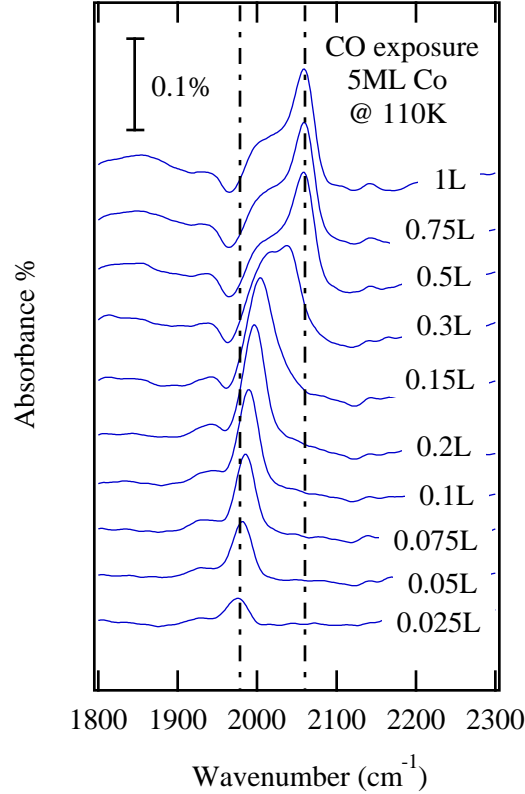


Figure 3.10: FTIR spectra from the CO/5 ML fcc-Co/Cu(100) system for different CO exposures at a temperature of 110 K.

extending to 2025 cm^{-1} . By an exposure of 0.3 L, the absorption feature becomes broad and extends to higher wave numbers, having a well-defined peak at 2038 cm^{-1} and a shoulder with a local maximum near 2000 cm^{-1} that appears to contain several overlapping features. At exposures of 0.5 L and higher, the spectrum is dominated by a peak at 2060 cm^{-1} with a broad shoulder extending from $\sim 2000\text{ cm}^{-1}$ to $\sim 2030\text{ cm}^{-1}$. From these measurements it appears that for exposures above 0.2 L, CO is adsorbed in more than one bonding configuration.

Temperature programmed desorption measurements are also consistent with the presence of multiple bonding configurations at higher CO exposures. Fig. 3.11 shows two CO TPD spectra from the 5 ML Co/Cu(100) system after exposure to 1 L CO at 110 K. Curve (a) was obtained by performing TPD immediately after CO exposure.

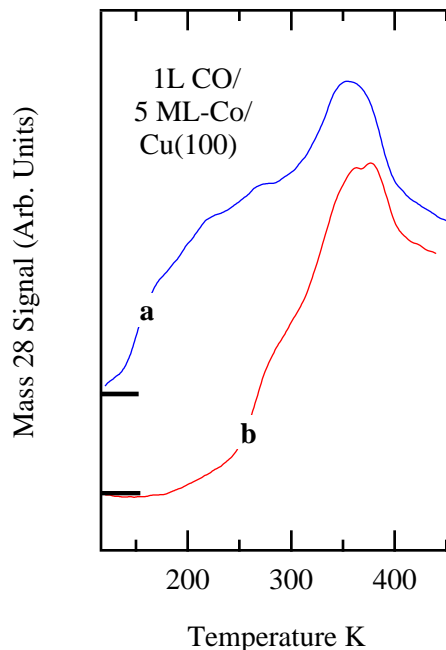


Figure 3.11: TPD spectra from CO adsorbed at 110 K onto 5 ML fcc-Co/Cu(100) film: (a) 1 L exposure at 110 K (b) after annealing to 250 K and returning to 110 K.

The spectrum is peaked near 355 K, but also contains a broad shoulder on the low temperature side with a threshold below 200 K, with an indication of weak local maxima near 220 K and 265 K. The appearance of the low temperature desorption features suggest that the high frequency (*i.e.*, above $\sim 2000\text{ cm}^{-1}$) features in the FTIR spectra for higher exposures are associated with CO weakly bound to the surface while the lower frequency feature corresponds to a more strongly bound state.

To explore this possibility, we investigated how the FTIR and TPD spectra change upon annealing to intermediate temperatures. Figure 3.12 shows two FTIR spectra in the frequency range of the CO stretch mode. Spectrum (a) is the 1 L spectrum of figure 3.10. Spectrum (b) was obtained after annealing the sample to 250 K and then returning it to 110 K. It is clear that upon this treatment, the high frequency feature at 2060 cm^{-1} is removed and the plateau at lower wavenumbers is replaced by a well-defined peak at 2027 cm^{-1} . After collecting these IR data, TPD spectrum (b) of figure 3.11 was obtained. Now, the onset of desorption occurs above 250 K, a

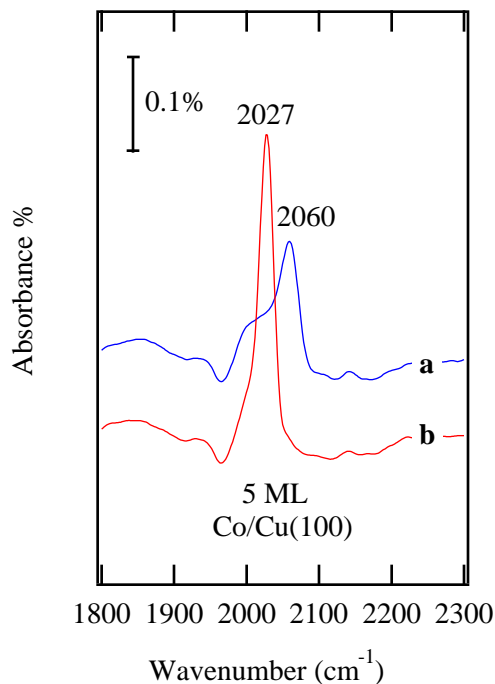


Figure 3.12: Infrared spectra of CO adsorbed on 5 ML fcc-Co/Cu(100): (a) 1 L exposure at 110 K (b) after annealing to 250 K and returning to 110 K.

weak shoulder is present between 275 K and 300 K, and the high temperature peak seen in TPD curve (a) remains. This comparison clearly shows that the 2060 cm^{-1} peak, as well as some of the plateau emission, seen in the FTIR spectra from the surface exposed to CO at 110 K (Fig. 3.10 and Fig. 3.12), are associated with weakly bound CO that produces the low temperature desorption features in TPD curve (a) of figure 3.11. Comparison with measurements from single crystal Co surfaces, and the trends as a function of Co thickness, indicate that the TPD spectra are dominated by desorption from Co. However, we cannot rule out that there is some contribution to the desorption threshold below 200 K seen in curve (a) of figure 3.11 from a very small amount ($\ll 0.05\text{ ML}$) of Cu on the surface of the films.

To compare the nature of the bonding after a room temperature (RT) anneal to direct deposition of CO at room temperature, FTIR spectra as a function of CO exposure with the sample held at RT were obtained. These spectra are shown in figure

3.13. Similar to what was observed for the sample at 110 K, a single feature at 1972 cm^{-1} is seen at low exposure. As the exposure increases, this peak shifts to higher frequency, saturating at 1983 cm^{-1} at 0.5 L exposure. The spectrum for 1 L exposure is essentially identical to that obtained at 0.5 L exposure.

The infrared spectra of figure 3.10 clearly indicate that there are multiple bonding configurations for CO on the fcc-Co(100) surface at low temperatures. The two vibrational features observed at 1936 cm^{-1} and 1974 cm^{-1} for the 0.025 L spectrum most likely correspond to adsorption at terrace bridge and atop sites, respectively. Studies

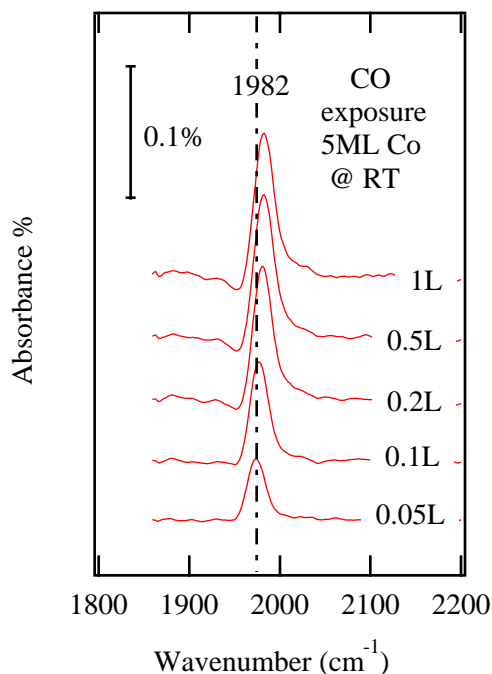


Figure 3.13: Infrared spectra of CO adsorbed on 5 ML Co/Cu(100) surface at room temperature.

of the vibrational properties of Co carbonyls find a vibrational frequency of 1973 cm^{-1} for the carbon-oxygen stretch mode in the CoCO molecule [110]. This is also similar to the C-O stretch frequency for atop adsorption of CO on the $(10\bar{1}0)$ surface of hcp-Co, which is found at 1972 cm^{-1} at low coverages [79]. In contrast, the corresponding value for the symmetric mode of the $(\text{Co})_2\text{CO}$ molecule is found 19 wavenumbers lower at

1953 cm^{-1} [110]. While this shift is somewhat smaller than found for the 1936 cm^{-1} mode observed on this surface, we assign this low frequency mode to bridge bonding sites on the terraces.

An alternative interpretation could be that the 1936 cm^{-1} mode arose from CO bound to step edges. However, such bonding modes are typically red-shifted from terrace modes by much larger amounts than the 37 cm^{-1} we find here. For example, studies of the vicinal Ni surface find the C-O stretch mode at 1865 cm^{-1} [111], some 154 cm^{-1} below the atop terrace site mode which occurs at 2019 cm^{-1} in that system. We therefore rule out bonding at step edges as the origin of the 1936 cm^{-1} mode.

In the low coverage limit, for both low temperature and room temperature adsorption, the FTIR spectra of CO on fcc-Co(100) shows a single feature near 1975 cm^{-1} associated with CO bound at terrace atop sites. The small shift to higher wavenumber with increasing exposure is attributed to dipole-dipole interaction among the molecules on the surface [106, 105]. A similar effect is observed for CO adsorption on the hcp-Co(10 $\bar{1}$ 0) surface, where the frequency of the atop site shifts from an initial value of 1972 cm^{-1} to 1994 cm^{-1} for exposure of 0.35 L.

When the fcc-Co(100) surface is exposed to CO at levels greater than 0.2 L, new features are observed in the vibrational spectrum. Initially the CO stretch absorption broadens to higher wavenumber, eventually developing a well defined feature at 2060 cm^{-1} for exposures of 0.5 L and higher. Comparison with the $\text{Co}(\text{CO})_2$ molecule, which is predicted to have a symmetric stretch at 2070 cm^{-1} [112], suggests a possible origin for this mode.

From these data we arrive at the following model for adsorption of CO on the fcc-Co(100) surface at low temperatures: At low exposure, adsorption is primarily on the atop site, although a small fraction of bridge bonding is also present. With increased exposure up to $\sim 0.2\text{ L}$, additional CO molecules are primarily accommodated at atop sites and are in close proximity giving rise to the dipole shift. No evidence

for a superstructure is seen in the LEED pattern after 0.2 L CO exposure, so it is unclear whether local order is present. Therefore, if CO forms islands with a local $c(2\times 2)$ symmetry, as is often found for CO adsorption on other transition metal (100) surfaces, then the islands are of very limited extent. For low temperature exposures greater than 0.2 L, weakly bound configurations form at the surface, as indicated by the presence of higher frequency CO stretch modes. These molecules presumably bind at non-ideal sites, perhaps near the boundary of any small adsorbate islands. At higher exposures (≥ 0.5 L) the mode at 2060 cm^{-1} is very close to the calculated stretch frequency of the $\text{Co}(\text{CO})_2$ molecule [112], suggesting that a subset of the CO molecules may enter a compressed phase where more-than-one CO is bound to a given Co surface atom. For low temperature adsorption on the hcp-Co($10\bar{1}0$) surface, a compressed phase on the terrace, where a higher surface concentration of molecules is accommodated by tilting the axis of the molecule away from the surface normal, is thought to give rise to a $\sim 20\text{ cm}^{-1}$ shift to higher frequency, from 1967 cm^{-1} to 1984 cm^{-1} [79].

Upon annealing the surface to 250 K, desorption features below this temperature are removed from the TPD spectrum and the 2060 cm^{-1} vibrational mode is replaced by a single strong feature at 2027 cm^{-1} in the IR spectrum. This feature has a very similar lineshape to the 1983 cm^{-1} peak found for the room temperature FTIR spectrum near saturation. Comparing the TPD spectra (a) and (b) of figure 3.11 suggests that about half of the CO adsorbed at low temperatures remains on the surface after annealing to 250 K, which is approximately the coverage upon room temperature adsorption. We interpret this behavior as the removal of the weakly bound species leaving only terminally bonded CO.

The adsorption of CO on metastable fcc-Co differs from adsorption on the high symmetry surfaces of hcp-Co in several ways. TPD spectra from the hcp-Co($10\bar{1}0$) surface exposed to CO at 150 K, exhibit three well-defined features occurring at 232 K, 340 K and 396 K [79, 113]. When the same surface is exposed to CO at RT,

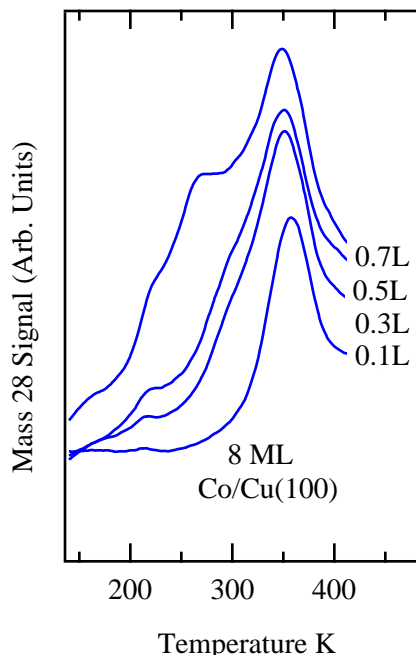


Figure 3.14: TPD spectra from CO adsorbed onto 8 ML fcc-Co/Cu(100) film for different exposures at 110 K.

only the 340 K and 396 K features are observed, and their lineshapes are less well-defined. For the fcc-Co(100) surface studied here, TPD spectra from CO adsorbed at low temperatures contain a broad low temperature feature with an indication of peaks at 220 K and 275 K, as well as a high temperature desorption feature centered at about 355 K. Temperature Programmed desorption (TPD) confirmed that observed infrared frequency features are rising with increasing the CO coverage. As in the FTIR spectra weak bonding configurations associated with low desorption temperature peak appear above 0.3 Langmuir (L) CO coverage.

Figure 3.14 shows TPD spectra for 8 monolayer cobalt film grown on Cu(100) for different exposures below saturation exposure of CO gas. The two low temperature features at 220 K and 275 K are absent from the spectra below 0.3 L coverage and only the main TPD peak is present at 375 K. This last feature appears at a significantly lower temperature than that found for the surfaces of hcp-Co, indicating that CO binds to the terraces of metastable fcc-Co more weakly than it does to the single crystal Co

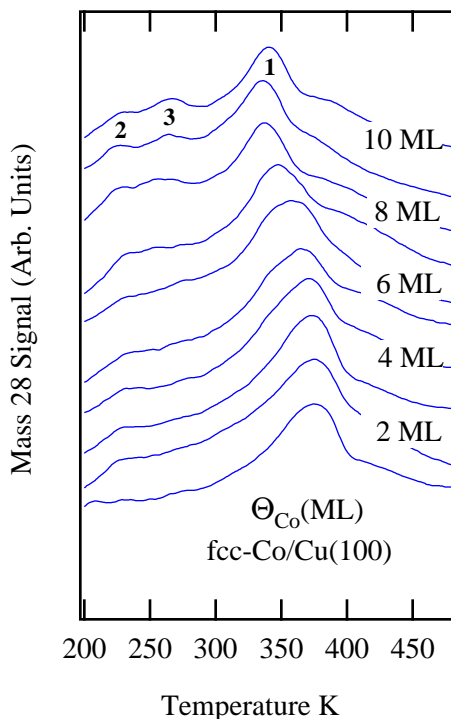


Figure 3.15: TPD spectra from CO adsorbed at 110 K onto n -ML fcc-Co/Cu(100) films: cobalt film thickness changes from 1 ML to 10 ML. All spectra taken for sample initially cooled at or below 120 K.

surface. Upon closer inspection of cobalt films of different thicknesses (Fig. 3.15), this high temperature peak appears to be a superposition of two features, one near 345 K and the other near 375 K. Depending on thin film thickness these features become more or less intense. The study of the system for different thicknesses revealed a CO TPD peak at 345 K for fcc-Co films thicker than 5 ML, and a peak near 375 K for desorption from films thinner than 5 ML, seen in figure 3.15. These differences are likely the result of the strained fcc-Co of the very thin films relaxing to unstrained fcc-Co for thicker films [74], with the 5 ML film supporting both relaxed and unrelaxed regions.

Finally, we note CO chemisorption has also been studied on the surface of another metastable film: fcc-Fe/Cu(100) [80, 81, 114]. In that case, adsorption at low temperatures results in adsorption first at bridge sites, and then at atop sites. Similar to what was observed here for the CO/fcc-Co(100) surface, in the Fe case, the molecules revert

to a single atop site after annealing. Moreover, similar to the Co/Cu(100) system, the Fe overlayer undergoes an fcc \rightarrow fct phase transition when the film thickness is increased from 4 ML to 5 ML. In that case, it is observed that there is a minor change in the CO stretch vibrational frequency from 2032 cm^{-1} to 2038 cm^{-1} at saturation coverage [81]. In our case, we do not observe such a minor change in frequency when the Co film relaxes.

3.4.1 Cu segregation on Co surface

The growth mode of a thin film in the thermodynamic limit is determined by the surface free energies of the substrate (σ_s), the overlayer (σ_f), the interface energy between the film and the substrate (σ_i) and the energy of strain (σ_e). Depending on the relative values, the system will try to minimize its total energy. This leads to the several thin film growth modes, which are categorized as follows: an overlayer film grows layer-by-layer (Frank-Van der Merwe (FM) growth), an overlayer grows 3-D islands immediately upon contact (Volmer-Weber (VW) growth), or an overlayer grows layer-by-layer for the first few monolayers and transits to 3-D islands growth upon reaching a critical film thickness (Stranski-Krastanov (SK) growth) [115]. Layer by layer growing mode (FM growth) is possible if the following equation is satisfied:

$$\sigma_f - \sigma_s + \sigma_i - \sigma_e < 0 \quad (3.15)$$

In the case of ultrathin CO films on Cu(100), the Co(100) surface has higher surface free energy ($\sigma_f \sim 2.71 \text{ J/m}^2$) than Cu ($\sigma_s \sim 1.94 \text{ J/m}^2$). In addition to this it has been shown that the heat of mixing Co-Cu interface is endothermic, and so free energy at the Co/Cu interface σ_i would add positive weight to the left side of equation 3.15. According to the theory, cobalt films should have a VW growth mode, however, for Co films grown at room temperature, SK growth mode is usually observed in experiments. When cobalt is deposited on a Cu(100) surface, since Cu(100) has lower

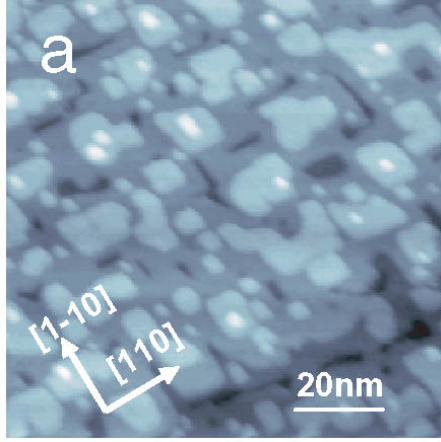


Figure 3.16: STM image of cobalt thin film grown on Cu(100)

free surface energy than Co(100), it is expected that Cu atoms may form a layer on top of the Co film, or the Cu atoms may form a surface alloy with Co atoms. In order to achieve this Cu atoms should overcome a diffusion barrier and append to the top of the surface. This can be realized by increasing the surface temperature and/or number of defect sites [116]. In this subsection we investigate the question about the temperature and conditions during which copper enrichment happens at the surface. It is well known that the hetero-epitaxial growth of a material on a surface of a certain crystalline substrate can be pseudomorphic when the lattice parameters involved are not too different from each other. Although Co has a different crystal structure than Cu at room temperature Co/Cu(100) is still a good epitaxial system since both of metals have small (about 2%) lattice mismatch ($a_{Cu} = 3.61 \text{ \AA}$, $a_{Co} = 3.56 \text{ \AA}$). Moroni et al. have performed a scanning tunneling microscopy (STM) study on the growth and morphology of ultrathin cobalt films on Cu(100)[78, 117]. In their paper W. Weber et al. show that for the Co/Cu(100) system, critical thicknesses were found between 10 and 20 ML, depending on the substrate temperature during growth. Below this thickness cobalt forms an incomplete monolayer, while starting the next monolayer formation. The incomplete top layer is distorted and the average lattice constant is modified at the surface. Annealing the film at a temperature of 440 K smooths the film surface

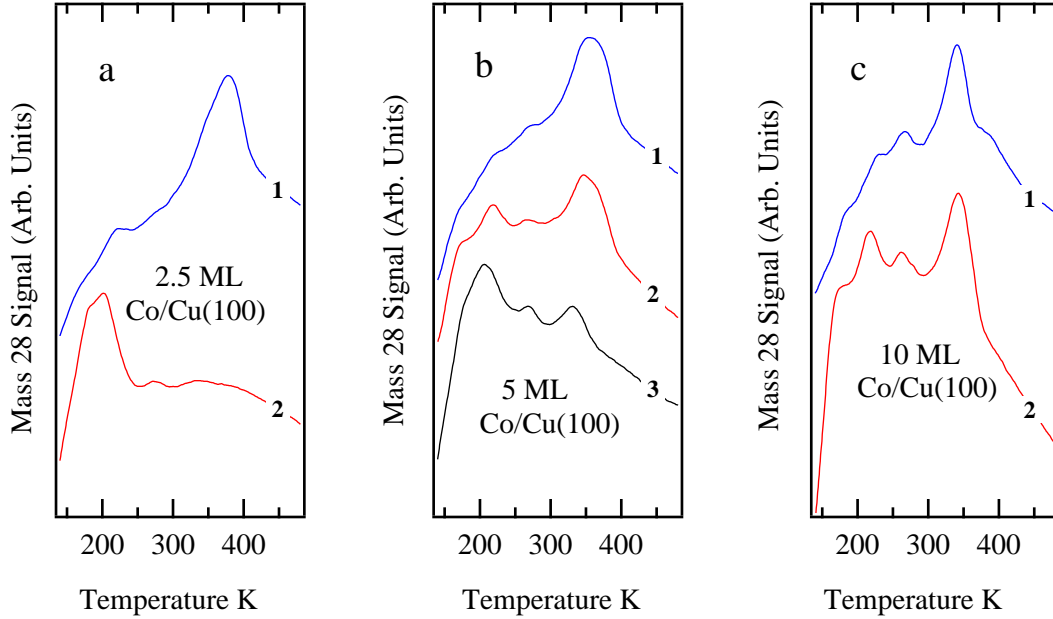


Figure 3.17: High temperature annealing effect (550 K, 3 min) on 2.5 ML (a), 5 ML (b), 10 ML (c) fcc-Co/Cu(100) films. Curves noted by (1) represent cobalt films before annealing (blue, if colored), curves noted by (2) represent cobalt films before annealing (red, if colored), curve (3) for 5 ML film enriched by $\sim 5\%$ Cu

without any significant Co-Cu inter-diffusion.

To investigate annealing effect further, we did additional TPD measurements, where we performed 550 K annealing of Co thin films grown on Cu(100). From these experiments we can clearly see that upon annealing to a higher temperature than 440 K, namely to 550 K, copper diffusion happens to the surface to some extent. Figure 3.17 represents cobalt films before high temperature (550 K) anneal if these curves (blue, if colored) are noted by (1). After annealing to 550 K, the intensities of desorption features at 180 K and 220 K grow significantly, which is an indication that some copper is present on the surface (Fig. 3.17 (2)). This assumption was also confirmed by LEED analysis where we were able to see characteristic $c(2 \times 2)$ pattern upon 0.3 Langmuir CO adsorption, invisible otherwise on a CO covered cobalt surface. In order to further test these conclusions we intentionally deposited about 5% of a monolayer of copper on clean cobalt film. The TPD result indicated in curve 3.17 (3) for a 5 ML film has a

very similar lineshape as the annealed curves 3.17 (2). For further surface analysis we have collected Auger spectra as well, but it turns out to be poor technique for detecting the sub-monolayer amounts of copper and shows the same Co-Cu signal strength ratios before and after annealing.

3.5 Summary

The unoccupied electronic states and chemisorption properties of the fcc-Co/Cu(100) MQW system were investigated using inverse photoemission spectroscopy (IPE), temperature programmed desorption (TPD) and reflection-absorption infrared (FTIR) spectroscopy. Well-defined Co MQW states are observed between 1 eV and 2.5 eV above the Fermi level, and thus do not cause any significant modulation of the density of states near the Fermi level. The CO $2\pi^*$ is observed centered at ~ 4.4 eV above E_F . Upon exposure of the surface to 1 L of CO at 110 K, TPD data shows three desorption peaks centered at 220 K, 265 K and 355 K. The low temperature peak at 220 K is associated with a high frequency C-O stretch vibrational mode that is attributed to either frustrated adsorption or a compressed CO phase at high coverages. After annealing the surface to 250 K, the 2060 cm^{-1} CO stretch vibrational mode disappears from the IR spectrum, and a single mode at 2027 cm^{-1} remains. Subsequent TPD measurements show that only the high temperature desorption peak is seen after the intermediate temperature annealing. We propose that after annealing to intermediate temperatures, the CO bound at low symmetry sites is desorbed and only atop CO remains.

From our results, we conclude that Co films grow layer-by-layer on Cu(100) at room temperature. Upon annealing cobalt surface to higher temperature, namely to 550 K, copper diffusion happens to the surface to some extent. It is worth noting that similar phenomena have been observed in the Ni/Cu(111) system [118], where the CO TPD spectrum from an annealed (500 K for about 5 min) 1 ML Ni/Cu(111) film shows higher

intensity of Cu-site desorption, as compared to that of the Ni-site desorption. This has been believed to indicate a strong copper enrichment during the annealing.

Chapter 4

Unoccupied electronic structure and CO chemisorption on the Ni/Cu(100) system

4.1 Introduction

As we have already discussed in the previous chapter, ultrathin, epitaxial films of cobalt grown on nonmagnetic substrates, such as copper, are interesting examples of bimetallic systems, which reveal physical properties often not present in single crystal materials. From the technological point of view such complexity of bimetallic systems has very practical applications outlined in the introductory chapter 1.

Another important example of transition metal-noble metal bimetallic system is ultrathin nickel films grown on Cu(100) substrate. Nickel stands next to copper in periodic table and crystallizes in the face centered cubic (fcc) structure with a lattice parameter of 3.52 Å. Having the same crystal structure, and slightly different lattice parameter as copper ($\Delta a \sim 2.5\%$), under certain conditions nickel can be grown pseudomorphically on copper for thicknesses of more than ten monolayers. The lateral expansion imposed by pseudomorphic growth distorts the Ni(100) lattice tetragonally, with sufficient strain present in nickel film to accommodate the in-plane lattice parameter of Cu(100) [119].

The tetragonal distortions have been reported by Müller [120] during their studies of epitaxial Ni films grown on Cu(100) using quantitative LEED structure determinations. The measurement results show that the structural parameters of the films with different thicknesses up to 11 ML are almost identical. These studies were further confirmed by a more detailed quantitative LEED analyzes performed later by the same group [121, 119].

Nickel films of seven different thicknesses in the range of 1-11 ML were examined with LEED, and a pseudomorphic growth mode, where the lateral lattice parameter of the nickel film is enlarged to that of the Cu substrate, was confirmed. It turns out that for epitaxial Ni films on Cu(100) the tetragonal distortion is homogeneous and thickness-independent [119], in contrast with the fcc-Fe/Cu(100) or Co/Cu(111), where much more prominent structural complexity has been seen.

Unlike copper, nickel is strongly magnetic due to the partially unoccupied $3d$ states near the Fermi level. As in case of Co/Cu(100), the Ni/Cu(100) system is an example of a metastable structure where the system forms metallic quantum well (MQW) states in the Ni overlayer that change energy with overlayer thickness. These states do not appear to be the dominant features near the Fermi energy and reside 1 eV or more above the Fermi level, in contrast to the more commonly studied Cu, Ag, or Au MQW states. In this respect the Ni/Cu(100) system is very similar to the Co/Cu(100) MQW system.

In this chapter, we will discuss the unoccupied electronic structure of the Ni/Cu(100) system and CO chemisorption on it, which has been studied in our group previously [1]. Inverse photoemission (IPE) experiments and CO adsorption studies provide valuable information about nickel thin film electronic structure and morphology. Temperature programmed desorption (TPD) and Fourier transformed infrared (FTIR) spectroscopy methods are employed in chemisorption experiments. We compare the adsorption behavior of the Ni/Cu(100) surface when it is exposed to CO at room temperature (RT) and at ~ 110 K. In both cases CO adsorbs molecularly on nickel surface and the infrared absorbance as a function of energy is measured for low and room temperature. In combination with TPD measurements, FTIR spectroscopy gives valuable information about the bonding sites of adsorbed species. Our main focus of CO adsorption on the Ni/Cu(100) system is the influence on the CO adsorption of the underlying copper substrate. The results will be compared to CO adsorption on the Ni(100) surface

[4, 122].

4.2 Experimental Aspects

The experimental procedure is similar to that of described in chapter 3.2. We prepared the Ni/Cu(100) MQW system by depositing nickel films on a clean Cu(100) single crystal and performed experiments *in situ* using the ultra-high vacuum (UHV) chamber described in detail in Sec. 2.2. Nickel and cobalt electron beam evaporation sources were provided in the same chamber with the similar routine for the thin film deposition. Surface analytical techniques used to study Ni/Cu(100) system include: Temperature programmed desorption (TPD), inverse photoemission (IPE), Fourier transformed infrared (FTIR) spectroscopy.

Nickel was deposited using an electron beam evaporation source that employs high purity (99.995%) metal. The pressure during nickel evaporation was typically 1×10^{-9} torr. The Ni thickness was measured using the QCM which was mounted below the sample and calibrated with Rutherford backscattering spectrometry to an accuracy of 0.1 ML. After depositing the desired number of Ni monolayers at room temperature, the sample was annealed at 450 K for 5 minutes. This procedure smooths the nickel film surface without significant substrate inter-diffusion, which has been confirmed in their research by Shen et al. [123]. However, care is needed when annealing thinner films ≤ 2 ML, since earlier studies [1] indicate copper surface segregation. In subsequent steps, the sample was never heated above this temperature.

Exposure of the Ni surface to CO, either with the sample at low temperature (~ 110 K) or at room temperature, was achieved by backfilling the chamber with CO gas at a fixed pressure in the range of $1 - 5 \times 10^{-9}$ torr. The total exposure was 1 Langmuir [L] ($1\text{L} = 1 \times 10^{-6}$ torr·s). Both FTIR spectroscopy and TPD show no significant changes above this exposure, which corresponds to a CO coverage below $\theta = 0.5$ ML [4, 124]. After IPE measurement of both the clean Cu(100) substrate and thin-film Ni/Cu(100)

MQW, FTIR spectra have been taken for CO uptake in the frequency range of 4000-1000 cm^{-1} . In all cases, the reported spectra has been collected as an average of 1000 scans, with the resolution of 4 cm^{-1} . TPD spectrum is obtained by monitoring the CO signal while ramping the sample temperature at a constant rate of 1 K/s.

4.3 Unoccupied electronic structure of the Ni/Cu(100)

Before discussing our electronic structure studies of epitaxial nickel films, it is worthwhile to briefly review the band structure of single crystal Ni(100). There has been significant effort dedicated to single crystal nickel electronic structure research both above and bellow the Fermi level using different spectroscopy methods [126, 89, 127, 128, 129].

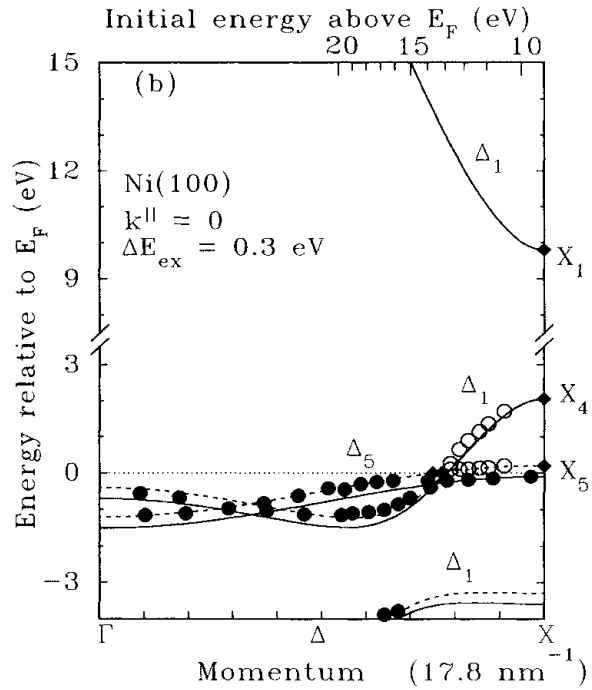


Figure 4.1: Calculated Ni(100) band structure in Γ - Δ - X direction. Solid and open circles indicate photoemission and inverse photoemission experimental results respectively [3].

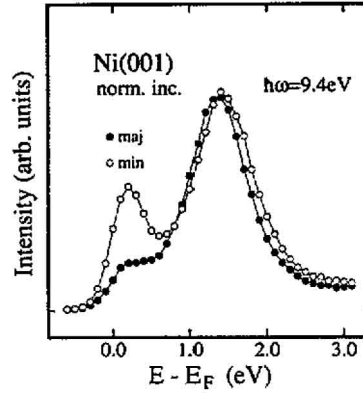


Figure 4.2: Spin resolved IPE spectra from the Ni(100) single crystal at a normal incidence. Both minority (open circles) and majority spin (solid circles) spectra are plotted as a function of energy above the Fermi level [125].

The calculated band structure of Ni(100) along the Γ - Δ -X direction¹ is shown in figure 4.1 [3]. As in the case of cobalt the bulk electronic structure of nickel exhibits a Shockley inverted energy gap along the [100] direction, spanning from $X_{4'}$ to X_1 . The values of $X_{4'}$ to X_1 are 2.8 eV and 9.8 eV respectively with respect to the Fermi energy.

Figure 4.2 shows a spin resolved IPE results for the single crystal Ni(100) surface [125]. As we see from the figure, there are two features in the spectrum: The main feature, which is observed for both minority and majority spin electrons around 1.5 eV above the Fermi level E_F , represents direct sp electron transitions. There is a second feature, which is mostly present for minority spin electrons, resulting from indirect transitions to an unoccupied d-band of nickel and lying very close to the Fermi energy. This observation is in accordance with the calculated band structure shown in figure 4.1, where only the minority spin electron band rises above the Fermi level towards the X point. Apart from these two peaks in the spectrum, a sharp image potential state is also observed at about 4.3 eV above E_F [126]. As we see these spectral features are similar to ones obtained for fcc-Co/Cu(100) system.

¹Geometric structure on fcc lattice and main crystallographic directions are discussed in chapter 3. See figure 3.1 for more detail

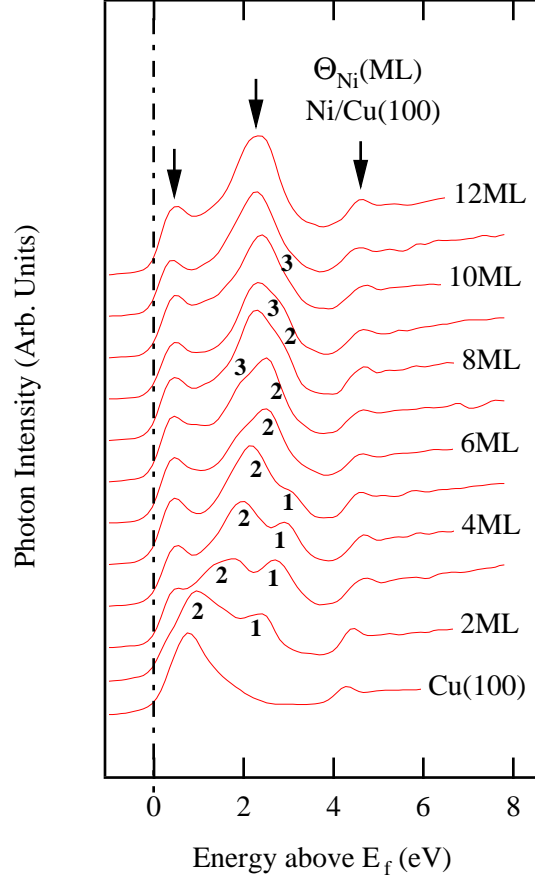


Figure 4.3: IPE spectra from the Ni/Cu(100) system. Each spectrum is plotted as a function of energy above the Fermi level and corresponds to a different Ni film thickness (as labeled on the right) with the thickness increasing toward the top of the figure [1].

In figure 4.3 the unoccupied electronic structure of the Ni/Cu(100) system is represented by the series of normal incidence IPE spectra from Ni films of different thickness, deposited on the Cu(100) substrate [1]. The clean Cu(100) surface shows two main features as we already noted in chapter 3.3; a bulklike *sp* transitions just above the Fermi level and an image potential state around 4.2 eV. After depositing a few monolayers of Ni, the corresponding IPE spectrum changes: a weak shoulder appears near E_F , which represents indirect transitions to unoccupied d-band of nickel, while the Ni *sp* transitions show up at ~ 2 eV above E_F . This feature together with indirect nickel d-band transitions are fingerprints of nickel presence on the copper surface. Both of these

features and the image potential state at 4.3 eV are indicated with downward pointed arrows in figure 4.3. It is interesting to notice that the thin film nickel *sp* transitions appear to have ~ 0.5 eV higher energy compared to the single crystal Ni *sp* feature as shown in figure 4.2. Besides these peaks, there are other features which do not exist in clean Ni(100) spectra and change energy for nickel films of different thickness. They are noted with numbers 1, 2, 3 in the spectra and we identify them as MQW states moving up in energy with increasing Ni film thickness, as seen on figure 4.3. The dispersion energy range observed in Ni/Cu(100) system is wider than the offset between the Cu and Ni X'_4 points, which is about 0.5 eV [125]. This is an indication that true metallic quantum well states, as well as resonances, are forming inside the nickel film.

The phase analysis model (PAM) (3.3.1) was used to compare the experimental results with this simple theoretical model. The MQW states are categorized by number $\nu = m - n$ as the difference between the number of layers in the film m and the number of nodes in the wavefunction n , perpendicular to the nickel film surface. As in the case of cobalt, in the Ni/Cu(100) MQW system the band gap we are dealing with is the Shockley-inverted gap above the X'_4 point of copper, and Eqn. 4.1 will have same expression as before:

$$\Delta\varphi_C = \begin{cases} 0 & E < E_L \\ 2 \arcsin [(E - E_L)/(E_U - E_L)]^{1/2} & E_L < E < E_U \\ \pi & E > E_U \end{cases} \quad (4.1)$$

The calculation results are plotted in figure 4.4. As we see from the figure, the $\nu = 0$ feature at higher energy (indicated by (1) in fig.4.3) is consistent with the $\nu = 0$ PAM calculated MQW state and moves up in energy with increasing nickel film thickness, although we do not see the saturation at X'_4 point where IPE peak simply disappears. The $\nu = 1$ and $\nu = 2$ features in IPE spectra were difficult to resolve, due to the presence of the strong *sp* transition peak in the spectra. The PAM calculated MQW states can

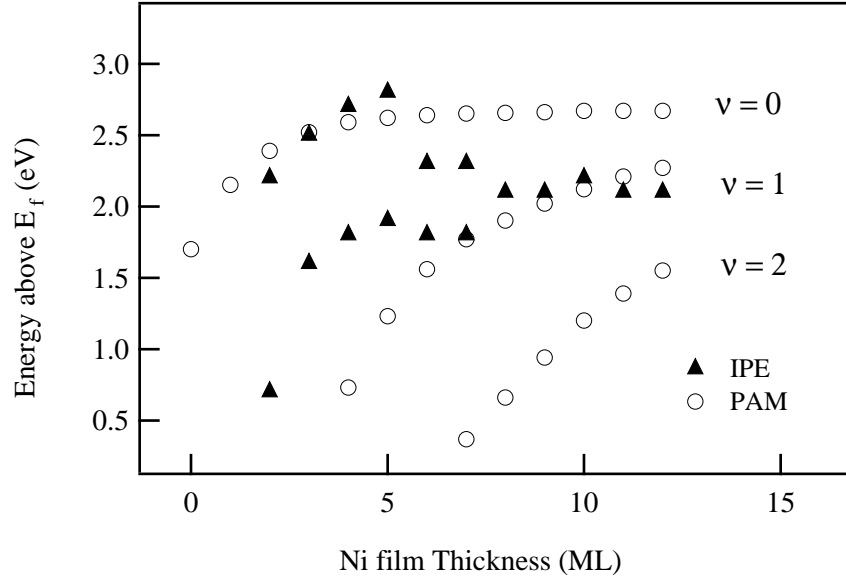


Figure 4.4: Comparison between the PAM calculation results and the IPE experimental results: solid triangles correspond to experimental values obtained from IPE. Open circles represent corresponding PAM calculated values [1].

account for lower energy $\nu = 1$ and $\nu = 2$ features, but the agreement is not quite good, as we see from figure 4.4. Carbon monoxide adsorption studies on Ni/Cu(100) show that unoccupied surface resonance existing in Ni/Cu(100) MQW system couples with and enhances bulklike *sp* transitions [1].

Figure 4.5 (a) shows a series of the normal incidence IPE spectra obtained from a n ML Ni/Cu(100) MQW system when the surface is exposed to 1L of CO at a temperature of ~ 110 K. It has been shown that the characteristic features to shift in energy Compared to the clean spectrum [1]. For example, the energy of the feature induced from a *d*-band transition of nickel is slightly higher for CO covered Ni films than for the clean Ni films (~ 0.1 eV). The origin of this shift is attributed to changes in the surface potential. Besides this energy shift, IPE spectra indicate changes associated with a significant reduction or increase in density of unoccupied electronic states. In order to have a better view about how CO adsorption changes the unoccupied electronic structure of Ni films, we plot a series of spectra where IPE spectra from a clean Ni film

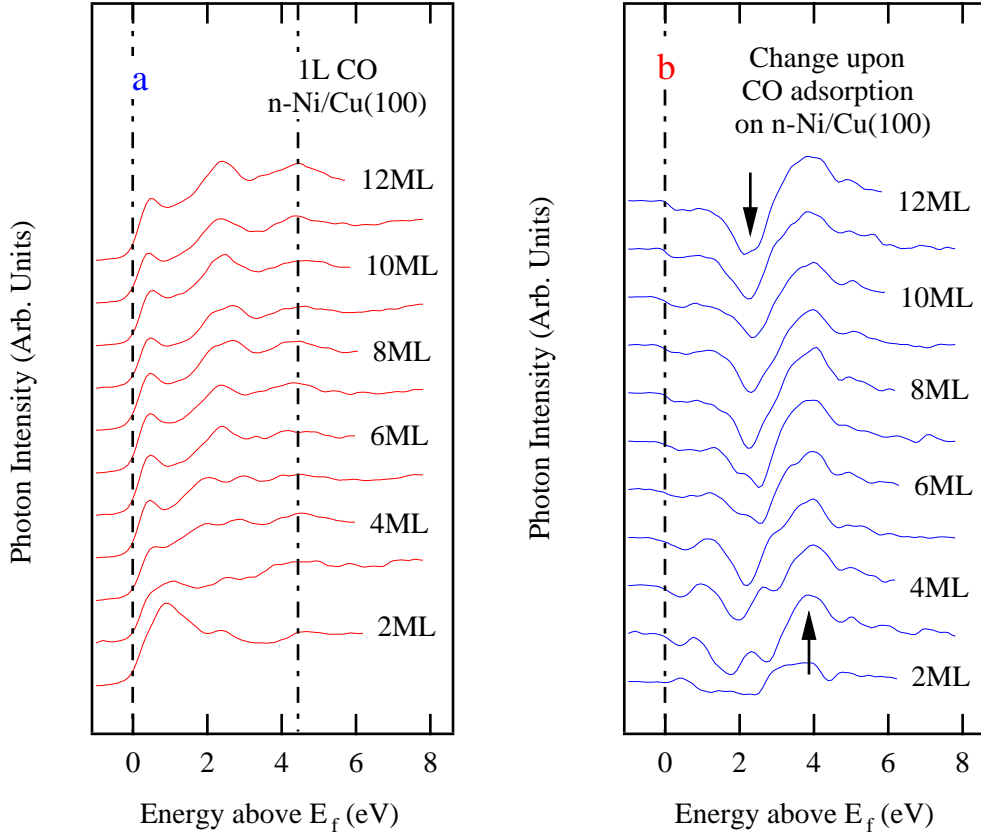


Figure 4.5: IPE spectra from 1L CO/n-ML-Ni/Cu(100)[1]

is subtracted from CO covered Ni film IPE spectra, as seen on figure 4.5 (b). There are two main features in spectra plotted on figure 4.5 (b): a large negative feature in the region between $\sim 1.9 - 2.1$ eV above the Fermi level, indicated with downward arrow, and a large positive excursion around 4 eV above the E_F , indicated with upward arrow. This last feature near 4 eV above the E_F is associated with the CO $2\pi^*$ antibonding orbital [37], which we also observe in IPE spectrum of CO covered fcc-Co/Cu(100) MQW system.

A major reduction of IPE intensity around 2 eV above the E_F upon CO adsorption is indicative of Ni related feature, which is rather sensitive to surface quality. Based on this observation, one might consider either a surface state or surface resonance as the origin of surface sensitive feature at ~ 2 eV above the E_F . It is well known that

surface states are formed at sharp interfaces of solid materials and represent the special solutions of Schrödinger equation, which are localized at the interfaces and decay fast into the bulk. The true surface states are characterized by energy bands that reside in the forbidden energy gap. At energies where a surface and bulk state are degenerate, surface and the bulk states can mix, forming a surface resonance. Such state is no longer localized at surface and propagates deep into the bulk, although it retains an enhanced amplitude near the surface. Since the feature observed in IPE spectrum of Ni thin films appears to have same energy as nickel bulk *sp* bands, we can conclude that it is a surface resonance rather than a surface state [129]. So the main feature in Ni/Cu(100) IPE spectra around 2 eV above the Fermi level is rising from unoccupied surface resonance coupled with the Ni bulk bands.

4.4 CO adsorption on Ni/Cu(100) system

CO adsorption on single crystal nickel surfaces has been investigated extensively [4, 130, 122, 131] using different experimental techniques, but less attention has been paid to thin-film Ni grown on other transition metal substrates such as copper. In the following section we will try to address to some open questions and somewhat complete the previous IPE and TPD studies of Ni thin films in our group [1]. As we already discussed in chapter 3, the essential aspects of the CO-transition metal bond can be understood in terms of the Blyholder model [102, 103, 104]. The basic ideas of this model, which are proven to work for different transition metal surfaces and particularly for cobalt, also work in case of nickel, as we see in the discussion below.

In the introduction we pointed out the similarities and differences between Ni/Cu(100) and Ni(100) systems, and the need to compare experimental results obtained for thin-film nickel and the single crystal Ni(100) surface. We start our discussion with single crystal Ni(100). It is well known that CO adsorbs molecularly on Ni(100) and occupies

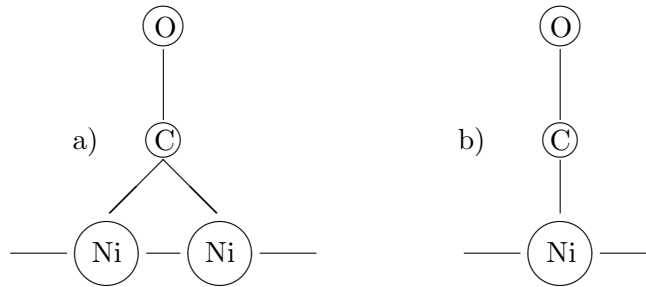


Figure 4.6: CO adsorption sites on a Ni(100) surface: (a) bridge site and (b) atop site.

mostly atop and bridge sites (see figure 4.6), where occupancy of each site strongly depends on the coverage and temperature of the supporting surface. In their research, Lauterbach et al. [4] showed that the atop site C-O stretch frequency changed from 2016 cm^{-1} to 2048 cm^{-1} depending on the CO coverage: increase of atop site occupation would lead to a blueshift in the C-O vibrational frequency as predicted from theoretical models [102, 106]. The stretch frequency also changed for CO bound at a bridge site from 1885 cm^{-1} to 1925 cm^{-1} with increasing CO coverage. Moreover, it

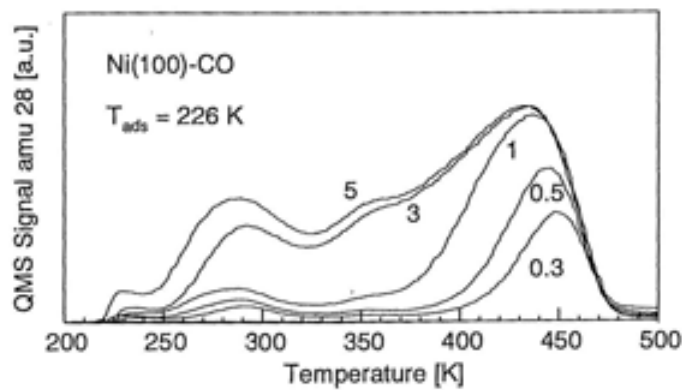


Figure 4.7: Series of TPD spectra taken after exposing increased amounts of CO from 0.3 L to 5 L to clean single crystal Ni(100) surface at different temperatures [4].

turns out that the bridge sites are favored over atop sites at low temperature. After

heating the substrate, the atop site becomes more populated than the bridge site, and this process is found to be reversible with the temperature. As we will see below, this trend is also true for the epitaxial Ni films grown on Cu(100).

TPD measurements [4] report three different peaks at 280, 360 and 445 K respectively, when exposing increasing amounts of CO to clean Ni(100) surface. The series of TPD spectra are shown in figure 4.7. The amount of CO exposure is indicated by the appropriate number on each curve in units of Langmuir ($1 \text{ L} = 1 \times 10^{-6} \text{ Torr} \cdot \text{Sec}$). Similar results are reported by Goodman et al. [130, 131]. In the paper of Yates et al. [122] they looked at CO^{18} isotope desorption from the Ni(100) surface, while impinging the same surface with various incident fluxes of CO^{16} . In this case, different TPD peaks were observed at 240, 290, 350 and 440 K. Using the CO^{18} isotope in the experiments revealed that intermolecular interactions do not involve CO dissociation-recombination processes, rather than the displacement of a molecule as a whole. The measurements also confirm that contamination of the Ni(100) surface with other gases has a great effect on lineshape of the CO TPD spectra. For most of the co-adsorbed species the CO atop site desorption temperature decreases, caused by adsorbate-adsorbate interactions, except the case of CO and H co-adsorption, where hydrogen forces the predominant CO adsorption to be at bridge sites and increases the desorption temperature [130].

As we have seen in section 4.3, thin-film nickel has a more complex electronic structure compared to single crystal Ni(100). The main complications arising from MQW states and the existence of a surface resonance for nickel films as thick as 12 ML. In order to investigate CO covered thin-film nickel surfaces with a greater depth, we performed studies of CO/Ni/Cu(100) system using FTIR spectroscopy.

Figure 4.8 shows a series of FTIR spectra in the region of the CO stretch vibration for the 7 monolayer Ni/Cu(100) MQW system as a function of increasing CO exposure. For the lowest exposures, the spectrum is dominated by a peak at 1886 cm^{-1} , which we associate to CO bonding to bridge site. As the CO exposure increases, the intensity

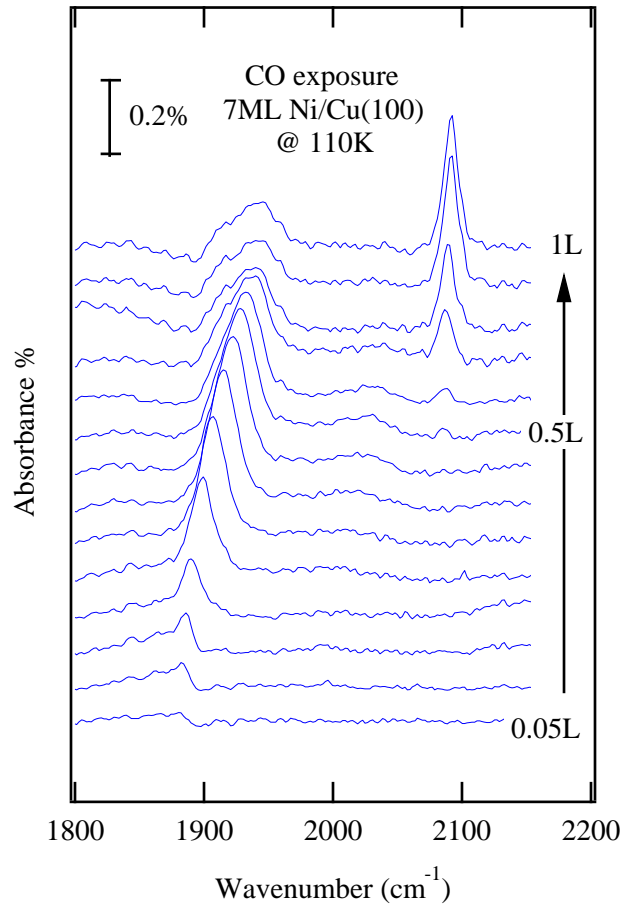


Figure 4.8: FTIR spectra from the CO/7 ML Ni/Cu(100) system for different CO exposures at a temperature of 110 K.

of the peak increases and its frequency shifts to $\sim 1934 \text{ cm}^{-1}$ in a monotonic fashion. Besides this low frequency peak there is a weak and broad feature around 1998 cm^{-1} and its intensity grows slightly with increasing exposure, while its energy blueshifts up to $\sim 2027 \text{ cm}^{-1}$. This peak represents the atop site CO vibrational mode. After reaching an exposure of 0.5 L, a new absorption feature appears in spectrum, having a well-defined peak around 2090 cm^{-1} . At exposures of 0.5 L and higher, the spectrum is dominated by this peak, while the lower energy features seem to be suppressed considerably. The origin of this feature is less clear and it was also seen for single crystal Ni(100) surface. It looks similar to the so called compressed phase observed in FTIR spectra of cobalt

thin-films, which we discussed in the previous chapter.

Temperature programmed desorption measurements confirm the presence of multiple bonding configurations. Figure 4.9 shows different CO exposures for the 10 ML Ni/Cu(100) MQW system. For low exposures, we only see a single desorption feature at ~ 425 K, which is consistent with FTIR result and corresponds to bridge bonded CO. Increasing the CO gas exposure up to 0.5L leads to the appearance of a shoulder around 350 K, which we associate with terminally bonded CO, and two small peaks at 230 K and 280 K, resulting from the desorption of weakly bound species. The appearance of the low temperature desorption peaks in TPD spectra suggest that the high frequency (*i.e.*, ~ 2090 cm $^{-1}$) feature in the FTIR is coming from these CO species that are weakly bound to the surface.

Fig. 4.10 represents the results of TPD measurements from 1L CO adsorbed onto the Ni/Cu(100) system with different nickel film thickness. On the 2ML, 4.5ML and 7.5ML Ni films, CO was exposed at 110 K and on the 5ML film exposure was performed at room temperature (RT). All films have similar desorption peak temperatures and we do not observe a thickness dependance of the 420 K feature, as it has been seen for fcc-Co films grown on Cu(100). In that case cobalt films thicker than 5 ML had a lower desorption temperature for terminally bonded CO as compared to films thinner than 5 ML (see ch. 3.4). This can be explained by the homogeneous tetragonal distortion of fcc structure of nickel films of different thicknesses [119], where for nickel films the tetragonal distortion is thickness-independent having unrelaxed regions for Ni films up to 11 ML. In addition to this, the desorption temperature of bridge bonded CO from the Ni/Cu(100) system is ~ 20 K lower than desorption temperature from Ni(100) for the same coverage of CO. It seems that for Ni films under tensile strain, the available electron density for $2\pi^*$ back donation is lower than that of the corresponding unstrained film; according to the “pillow model” suggested by Kampshoff et al. [132]. In that model the available electron density of a strained metal surface for back donation to the CO

$2\pi^*$ orbital is a linear function of the strain. If the film atom density is lower (tensile strain) the electron density also decreases and reduces back donation effect to CO $2\pi^*$. As a consequence, tensile strain would result in the weaker overall bonding of CO to the metal surface. The effect is stronger for bridge bonded CO compared to terminally bonded CO, since electron depletion would occur in-between the Ni atoms. The TPD experiments confirm this statement showing a ~ 30 K decrease of the TPD peak at 420 K of bridge bonded CO adsorbed on n-ML Ni/Cu(100) system as compared to the TPD peak at 450 K of similar CO species adsorbed on single crystal Ni, while the atop bounded CO TPD shoulder at ~ 350 K remains practically unchanged.

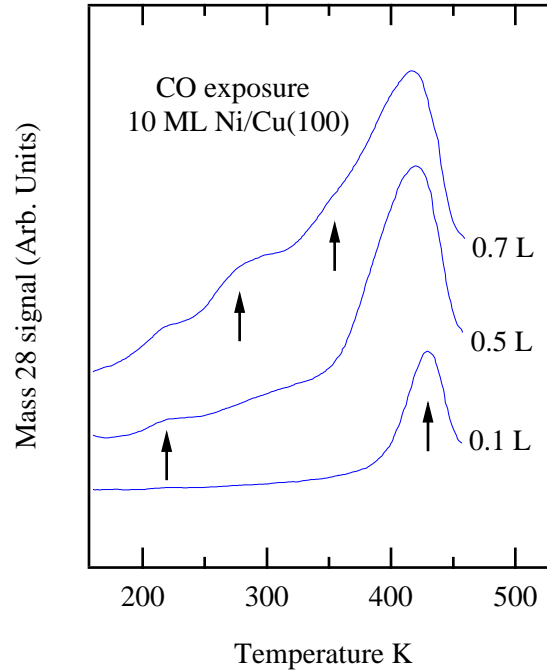


Figure 4.9: TPD spectra from different CO exposures onto 10ML Ni/Cu(100) film at 110 K. Features on the figure are indicated with arrows.

In order to explore connections between TPD and FTIR features further, we investigated how these spectra change upon annealing to intermediate temperatures. Fig. 4.11 shows FTIR spectra of 1 L CO/7 ML Ni/Cu(100) system in the frequency range of the CO stretch mode. Each subsequent spectrum was obtained after annealing the

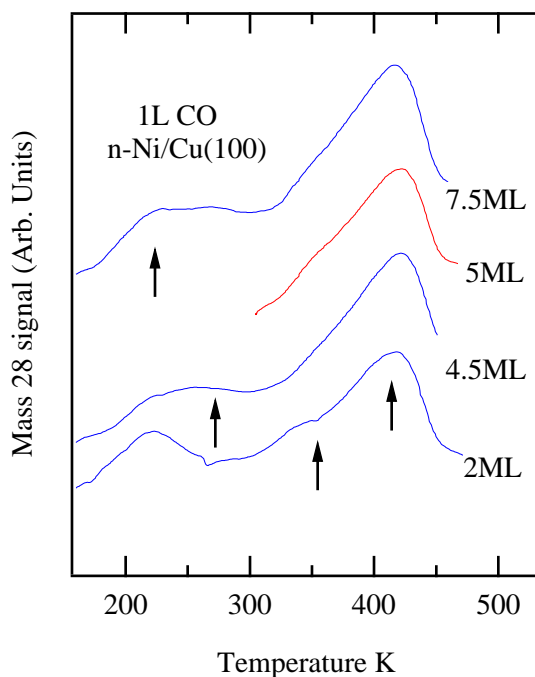


Figure 4.10: TPD spectra from 1L CO adsorbed onto n-Ni/Cu(100) film: On 2ML, 4.5ML and 7.5ML films, CO exposed at 110 K, and on 5ML film at room temperature.

nickel film to some pre-defined temperature and returning it to 110 K, after which infrared spectra were taken. Upon annealing to 200 K, the infrared spectrum stays practically unchanged, only the feature associated with the bridge site becomes sharper than before, as the wide feature is replaced by a well-defined peak at 1948 cm^{-1} . This is indicative of better ordering with increased mobility of CO molecules, while temperature was held at 200 K for a few minutes. Annealing to 250 K desorbs most of the weakly bound CO species, as indicated by the disappearance of the corresponding high frequency vibrational features from the spectrum, and by the increase of bridge vibrational mode intensity further. Annealing to 350 K results in dramatic changes in the spectrum: the atop site CO with a vibrational mode at $\sim 2059\text{ cm}^{-1}$ gets highly populated and well-ordered, while the bridge-bonded CO vibrational mode reduces its response greatly as seen in the FTIR spectra on figure 4.11. It is clear that the top sites are favored over a bridge sites above room temperature, after the film supporting

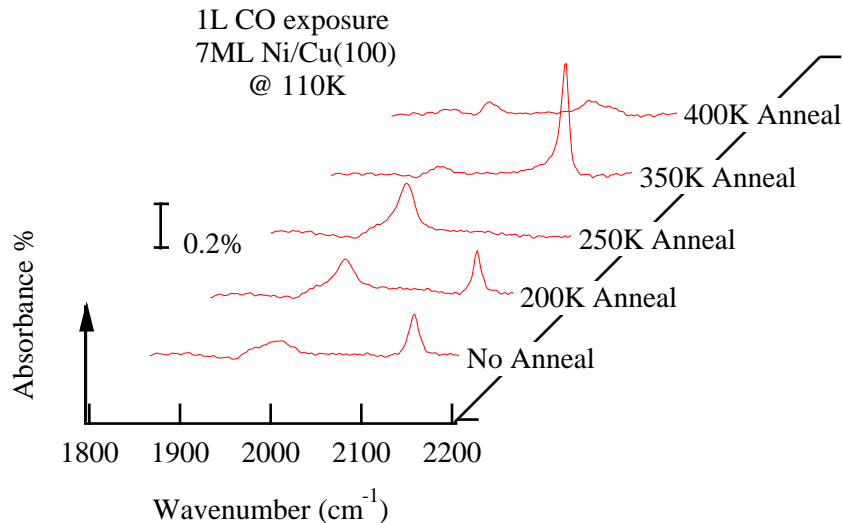


Figure 4.11: FTIR spectra from the CO/7 ML Ni/Cu(100) system annealed to intermediate temperatures: all spectra were taken at 110 K for substrates annealed to 200 K, 250 K, 350 K and 400 K

the CO molecules passes through a threshold or so called activation temperature, found by Lauterbach *et al.* [4] for CO covered Ni(100) single crystal. This suggestion is confirmed by FTIR spectra as a function of CO exposure obtained for the sample held at room temperature. These spectra are shown in fig. 4.12 (a). Similar to single crystal Ni(100), shown in figure 4.12 (b), two vibrational modes are seen: The first feature is rather weak and it is seen at low exposure at $\sim 1890 \text{ cm}^{-1}$. As the exposure increases, this peak shifts to higher frequency, reaching its maximum at 1925 cm^{-1} for 1 L exposure. This feature we associate to CO bound to bridge site. The second feature is CO adsorbed to atop sites and appears at 2015 cm^{-1} . It is a much more prominent peak than bridge bonded CO, quickly saturating at 2050 cm^{-1} with increasing CO coverage. As we already discussed, the shifts to higher wavenumber with increasing exposure are attributed to dipole-dipole interaction among the molecules on the surface [106, 105]. The final stage of annealing at 400 K desorbed most of the terminally bonded CO, in

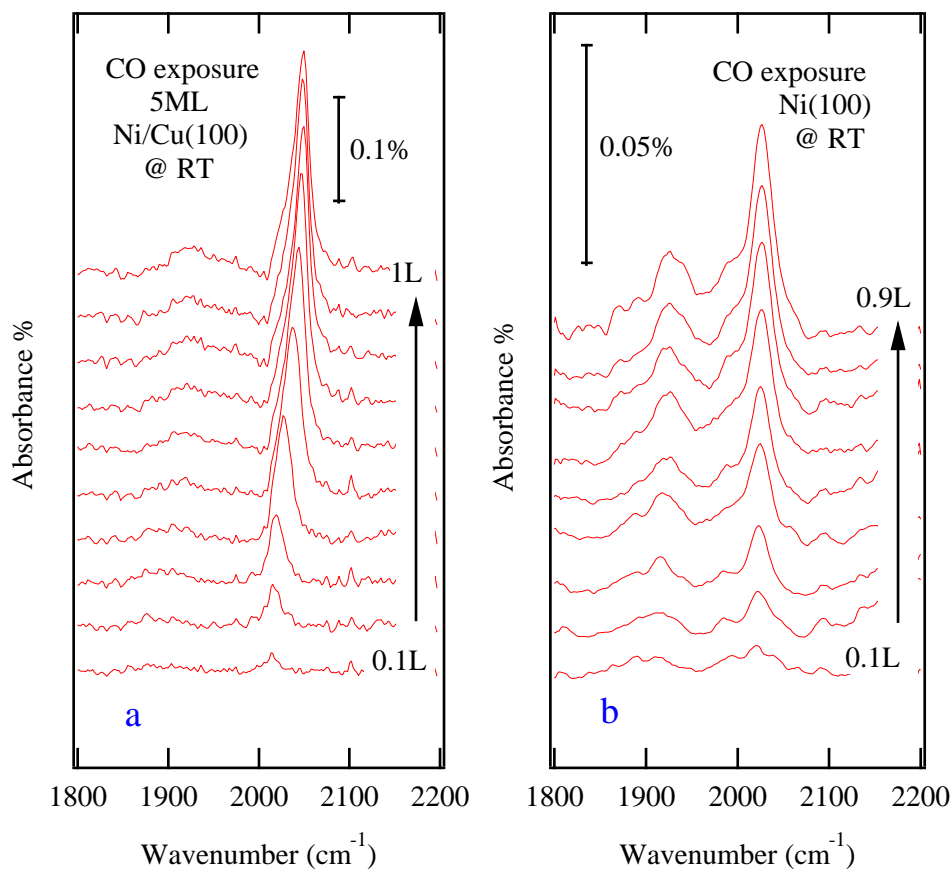


Figure 4.12: FTIR spectra from the Ni(100)(a) and CO/5 ML Ni/Cu(100) (b) for different CO exposures obtained at room temperature.

accordance with TPD results (Fig. 4.10, and Fig. 4.9), where a shoulder near ~ 350 K represents the atop CO desorption peak. The FTIR spectrum of CO/7 ML Ni/Cu(100) system annealed at 400 K (Fig. 4.11) shows that the remaining CO is adsorbed on both bridge and atop sites as expected, considering the low activation temperature for bridge-atop site transition and the elapsed time between heating and cooling the sample.

In many ways the adsorption of CO on epitaxial nickel films on copper is very similar to CO adsorption on the single crystal Ni(100) surface. The TPD spectra from the Ni/Cu(100) surface exposed to CO at 110 K exhibit a broad low temperature feature with an indication of peaks at 230 K and 280 K, a well-defined feature occurring

at ~ 420 K and a shoulder at ~ 350 K. This is close to TPD results obtained from CO covered Ni(100) single crystal surfaces. The only difference comes from the tensile strain which reduces the TPD peak of bridge bonded CO at about 20 K, for the Ni film surfaces studied here.

4.5 Summary

The unoccupied electronic states and chemisorption properties of the Ni/Cu(100) MQW system were investigated using inverse photoemission spectroscopy (IPE), temperature programmed desorption (TPD) and reflection-absorption infrared spectroscopy (FTIR). Ni films were grown layer-by-layer on a Cu(100) substrate at room temperature. Well-defined nickel MQW states are observed between 1 eV and 2.8 eV above the Fermi level, which were compared to phase accumulation model (PAM) calculational results. Discrepancy between the observed and calculated MQW state energies suggests that another feature, identified as surface resonance, exists in Ni/Cu(100) system above the Fermi level. The CO $2\pi^*$ is observed centered at ~ 4.4 eV above E_F .

CO chemisorption has been studied on the surface of Ni/Cu(100). Unlike the fcc-Co/Cu(100) case, at low temperatures and low exposure, adsorption is primarily on the bridge site, with a little atop adsorption. With increasing exposure additional CO molecules are accommodated on these sites close to each other giving rise to the dipole shift upward in energy. For low temperature exposures greater than 0.5 L, weakly bound configurations form at the surface, as indicated by the presence of higher frequency CO stretch modes. Similar weakly bound CO species were found in case of fcc-Co/Cu(100) where molecules presumably bind at non-ideal sites near the boundary of any small adsorbate islands and form a compressed phase where more-than-one CO is bound to a given cobalt atom (Chapter 3). The molecules revert from bridge site to a single atop site after annealing supporting Ni film above room temperature (RT).

Upon exposure of the surface to 1 L of CO at 110 K, TPD data show desorption peaks centered at 230 K, 280 K, 350 K and 425 K. These features are similar to TPD features observed for single crystal Ni(100). The bridge bonded CO desorption temperature peak for Ni/Cu(100) system is about 30 K lower than the corresponding peak for Ni(100), which can be explained by tensile strain present in nickel thin films within the framework of "pillow model" [132]. The low temperature peaks 230 K and 280 K in TPD spectra are attributed to either frustrated adsorption or a compressed CO phase at high coverage. After annealing the surface to 250 K, the 2090 cm^{-1} CO stretch vibrational mode disappears from the IR spectrum, indicating the removal of weakly bound CO species on the metal surface, while bridge bonded CO feature grows sharp. Subsequent annealing above room temperature reveals atop site preference over the bridge site, also confirmed by FTIR experiments done at RT.

Both Ni/Cu(100) and Co/Cu(100) systems show no evidence of MQW states affecting CO chemisorption unlike CO/Cu/fcc-Fe/Cu(100) MQW system, where correlation between the CO desorption temperature and unoccupied density of states (DOS) at E_F , modulated by MQW states crossing the Fermi level, has been seen [30, 28]. There are couple of reasons that explains this: First of all, on these transition metal based systems, the MQW states appear higher in energy with respect to the Fermi level, which makes it impossible to see any periodic modulations at E_F as well as periodic changes in CO-metal bond strength do to the presence of MQW states in unoccupied *sp* band of a transition metal. Secondly, CO-Ni and CO-Co bonds are much stronger than CO-Cu bond, where the contribution to CO-metal bond from partially occupied *d* bands is rather strong. As a consequence the overall effect of MQW states, which energetically reside at the unoccupied metal *sp* band, are relatively weak and difficult to observe in experiment. The obtained results suggest that more pronounced quantum size effects may be observed for weakly chemisorbed systems, where CO bonds to noble and near noble metals, such as Pt, Pd, Ag, Au.

Chapter 5

CO and dimethyl disulfide (DMDS) chemisorption on the Cu/fcc-Fe/Cu(100) system

5.1 Introduction

In the last two chapters we discussed fcc-Co/Cu(100) and Ni/Cu(100) transition metal/noble metal quantum well systems and CO chemisorption properties on them. Although we saw some differences associated with the thin film morphology and changes in crystal structure due to the underlying substrate, no apparent evidence has been observed which would indicate that metallic quantum well (MQW) states affect CO chemisorption. It seems that strong CO chemisorption on these systems compared to CO chemisorption on noble metal films such as copper is greatly overwhelming quantum size effects (QSE) caused by changes in the electronic structure. On the other hand, the impact of QSEs on the chemisorption has been observed for the Cu/fcc-Fe/Cu(100) system. Previous studies of copper thin films grown on fcc-Fe substrate film, carried out in our group, provide experimental evidence that the interaction between CO molecules and Cu surface can be manipulated by employing the MQW states [30]. Moreover, one can distinguish between structural and electronic effects in the molecule-surface interaction, as the electronic density of states of these systems vary as a function of thin-film thickness, while their surface geometric structure remains unchanged.

The experimental evidence that the electronic density of states can be altered with MQWs is supported by theoretical calculations. In cluster model calculations for Cu(100) [39], the unoccupied copper *sp* electronic states near E_F are thought to be

important contributors to the CO chemisorption on Cu(100) surface together with the occupied d -band states. The IPE spectroscopy studies of the copper thin films grown on fcc-Fe/Cu(100) substrate indicate the presence of unoccupied MQW states in spectra, associated with the quantization of the copper sp band [30]. As a result, modification of CO chemisorption properties due to the presence of MQW states in the density of states (DOS) at E_F is expected. Indeed, temperature programmed desorption (TPD) measurements of the Cu/fcc-Fe/Cu(100) system revealed that the peak desorption temperature, T_d , undergoes systematic changes as a function of copper thickness: T_d has a local maximum at thicknesses where a MQW state crosses the Fermi level, and is reduced for thicknesses in between. In addition to this overall reduction of the T_d of CO from the Cu overlayers is observed compared to T_d of CO on the single crystal Cu(100) surface. The last effect is similar to what we have already seen in case of Ni/Cu(100) MQW system and it is attributed to compressive strain in the copper overlayer, which we will discuss in more detail below.

As modern applications demand nanostructures that are increasingly small and thin, electronic QSEs become inevitable in many physical and chemical processes. The ultimate goal here is to turn these seemingly unfavorable effects into an advantage. The results obtained for the Cu/fcc-Fe/Cu(100) system suggest a way to tailor molecule-surface interactions using MQWs. Apart from the chemisorption strength, control of molecule-metal adsorption properties opens great possibilities to modify many parameters in the process, such as surface photochemistry and molecular self-assembly, which may prove particularly interesting in the case of thiols and related organic materials. There has been considerable interest in so-called self-assembled monolayers (SAMs) [133], which form from organic thiols on noble metal surfaces. This formation is a result of strong affinity between the thiol head groups and the Cu atoms, after which the hydrocarbon tail stabilizes into a monolayer. Within this chapter chemisorption properties of two different test molecules will be discussed: One of them is carbon

monoxide, adsorption properties of which long has been investigated on this particular system, and we will provide additional experimental evidence of QSEs affecting the chemisorption properties. Another example to probe molecule-surface interactions is the dimethyl disulfide (DMDS) molecule, consisting of two sulfur atoms and methyl radicals - $(\text{SCH}_3)_2$. DMDS is a simple example of an organic thiol, a class of molecules that exhibit self-assembly properties on metal surfaces. There are experimental and theoretical indications that an antibonding sulfur $3p$ - copper ($3d$, $4s$) hybrid state is in the same energy range where MQW states are seen in photoemission spectra [134], which suggests modifications of molecular adsorption on the surface by MQW states may be possible.

5.2 Experimental Aspects

The experimental procedure involves routine sputter-annealing cycles to prepare the clean Cu(100) surface inside the ultra-high vacuum (UHV) chamber with base pressure $\sim 1 \times 10^{-10}$ torr. Iron films were deposited afterwards using an electron beam evaporation source that employs a high purity (99.995%) metal slug. Subsequent copper deposition was carried out by resistive heating, where copper wire is wrapped around a tungsten filament and pre-melted into a small ball by passing current through the filament 2. The sublimation rate this way is lower than in case of e-beam heating, but provides stable copper flux and operates at lower pressures, typically on the order of 5×10^{-10} torr. The prepared surface was then studied by different surface analytical techniques, including temperature programmed desorption (TPD), inverse photoemission (IPE), Fourier transformed infrared spectroscopy (FTIRS), and scanning tunnelling microscopy (STM).

The Cu thickness was measured using the quartz crystal microbalance (QCM). After depositing the desired number of Cu monolayers at room temperature, the sample

was annealed at 380 K for 2 minutes in order to get smoother surface. The sample was allowed to cool down while taking the IPE spectra. After collecting the IPE spectra and performing LEED measurements, which are good experimental techniques to characterize the prepared surface, the clean Cu surface was exposed to predefined amounts of CO gas or DMDS vapor.

The CO gas adsorption procedure is identical to one described in chapters 3 and 4. The total exposure was 1 Langmuir [L] ($1 \text{ L} = 1 \times 10^{-6} \text{ torr}\cdot\text{s}$). DMDS vapor gas exposure on the prepared Cu/fcc-Fe/Cu(100) surface at room temperature was achieved using 99% pure liquid substance in a pyrex ampoule, which was further purified by freezing-pumping-heating cycles. Molecules were introduced in main chamber through the leak valve¹. The total exposure was 10 Langmuir [L] ($1 \text{ L} = 1 \times 10^{-6} \text{ torr}\cdot\text{s}$).

FTIR spectra were taken in the frequency range of 4000-1000 cm^{-1} . In all cases, the reported spectra are an average of 1000 scans, with a resolution of 4 cm^{-1} . A TPD spectrum is obtained by monitoring the corresponding mass signal while ramping the sample temperature at a constant rate of 1 K/s.

5.3 IPE spectra of the Cu/fcc-Fe/Cu(100) and CO chemisorption

IPE and CO chemisorption studies on the Cu/fcc-Fe/Cu(100) MQW system have drawn considerable attention in recent years due to the apparent QSEs observed on that system. IPE measurements have been performed by various groups and are available in the literature [135, 15, 28]. Figure 5.1 presents typical IPE spectra obtained at normal incidence from the Cu/fcc-Fe/Cu(100) system for a series of Cu overlayer thicknesses. The IPE spectrum from Cu(100) is the uppermost spectrum of the Fig. 5.1, which exhibits several well known features: a bulklike *sp* transitions just above the Fermi

¹The dimethyl disulfide (DMDS) SAMs formation is possible from both liquid and gas phase deposition, where gas phase deposition can be conducted in ultra high vacuum (UHV) environment, proven to remove solvent effects from the system

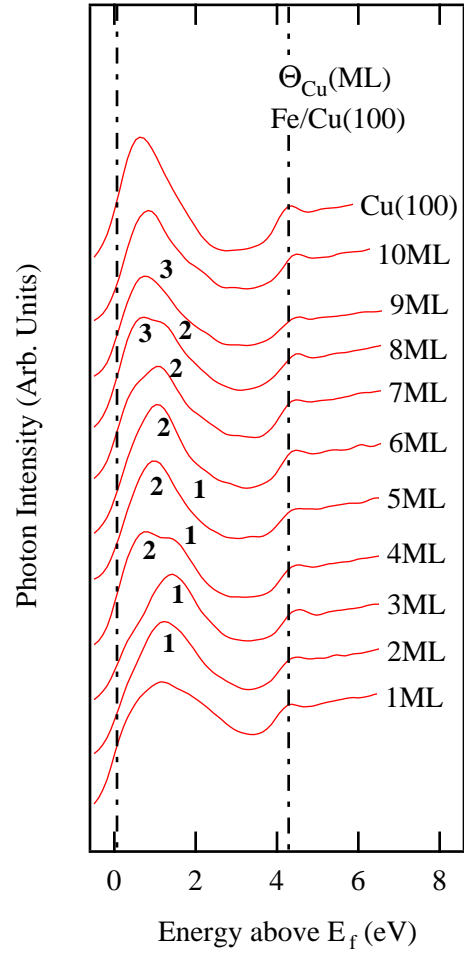


Figure 5.1: IPE spectra from the Cu/fcc-Fe/Cu(100) system. Each spectrum is plotted as a function of energy above E_F and corresponds to a different Cu film thickness (as labeled on the right) with the thickness increasing toward the top of the figure.

level and an image potential state around 4.2 eV. In addition to this, the spectra from the Cu overlayers exhibit a well-defined features, labelled by the numbers 1,2,3, which disperse upward in energy as we increase the copper layer thickness. These features are associated with copper quantum well states resulting from quantization of the unoccupied Cu *sp* band. Unlike the case of cobalt and nickel, discussed in chapters 3, 4, MQW states in Cu periodically cross the Fermi level, causing the IPE intensity at E_F to modulate substantially. According to figure 5.1, the first MQW state crosses E_F at about 4 ML Cu thickness² and increases IPE intensity at E_F . Increasing the Cu thickness farther would cause IPE intensity to reduce at E_F , while MQW moves upward in energy, until about 8 ML copper film thickness, where another MQW state crosses the Fermi level. The MQW state dispersion with thickness saturates at about 2 eV above the E_F , reaching the $X_{4'}$ -point of the Cu band structure along the (100) direction.

In order to investigate how MQW states affect CO chemisorption, TPD measurements were performed by Danese et al. [28] on Cu/fcc-Fe/Cu(100) system using CO as a test molecule. Analysis of the obtained TPD spectra revealed several interesting results. First of all, compared to single crystal Cu(100), the desorption temperature peak T_d is lower for all the Cu thicknesses of MQW system. This reduction of T_d is attributed to the changes in the d-band structure of thin-film copper. As we have already discussed in previous chapters, the description of the CO-transition metal bond is based on the Blyholder model [102, 103, 104], and it can be viewed as a donation of charge from the CO 5σ orbital, which is the highest occupied molecular orbital (HOMO) of CO molecule, to the metal, followed by electron backdonation into the CO $2\pi^*$, the lowest unoccupied molecular orbital (LUMO). Unlike most transition metals CO bonds weakly onto copper surface, and in this case charge donation from the CO 5σ orbital

²Critical thickness reported in reference [30] is 5 ML rather than 4 ML. This divergence can be attributed to the discrepancies in QCM thickness calibration.

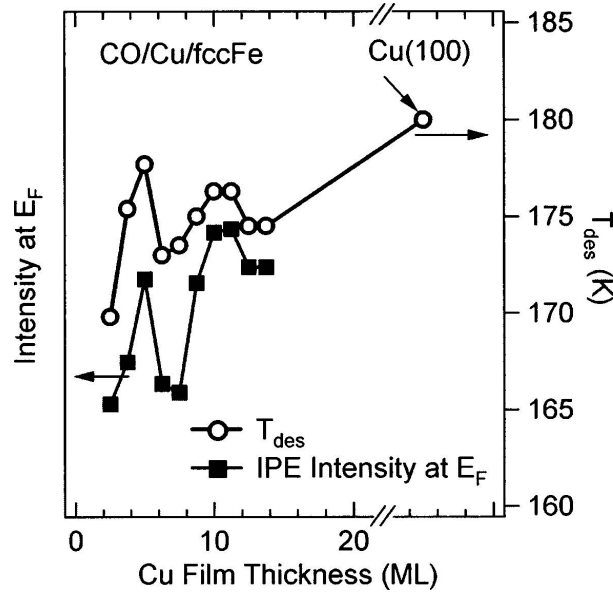


Figure 5.2: Plot of T_d (open circles) and $I(E_F)$ (solid squares) as a function of copper film thickness. They exhibit a local maximum near 5 ML followed by a subsequent decline and a second maximum near 10 ML [28].

does contribute considerably in CO-metal bonding, while backdonation into the CO $2\pi^*$ is relatively weak. Moreover, the Cu sp band is predicted to dominate over the d-bands in the electron backdonation from copper to CO $2\pi^*$ orbital [39]. The changes in the d-band structure of the copper film makes the electron donation from CO 5σ orbital more difficult. As a result the weaker bonding of CO to the thin film surface is expected compared to the single crystal Cu(100). More rigorous treatment of CO interaction with MQW system requires first principles calculations, which predict a shift in the centroid of the metal d-band. Photoemission studies of the Cu/fcc-Co/Cu(100) system [136] also revealed changes in the copper d-band, moving it slightly away from E_F with increasing copper thickness, suggesting weakening of the CO - metal bond.

The most important observation from Fig. 5.2 is that T_d is not the same for all MQW thicknesses, but rather it oscillates as a function of copper film thickness. In their research Danese et al. [28] have found that the IPE intensity at E_F and T_d are

highly correlated. In Fig. 5.2, the IPE intensity at E_F and values of T_d are plotted as a function of Cu overlayer thickness and show this correlation. As we see from the figure T_d is at maximum when IPE intensity at the Fermi level peaks up and vice versa. According to these experimental results and theoretical considerations, although the Cu d -levels play an important role in the CO bonding to the surface and overall shift in T_d , it is the unoccupied sp states at E_F which are responsible for T_d oscillations observed in Cu/fcc-Fe/Cu(100) MQW system as outlined in the introductory section 5.1.

In order to further investigate CO covered thin-film copper surfaces grown on iron, we performed FTIR spectroscopy studies. It is well-known that when adsorbed on the

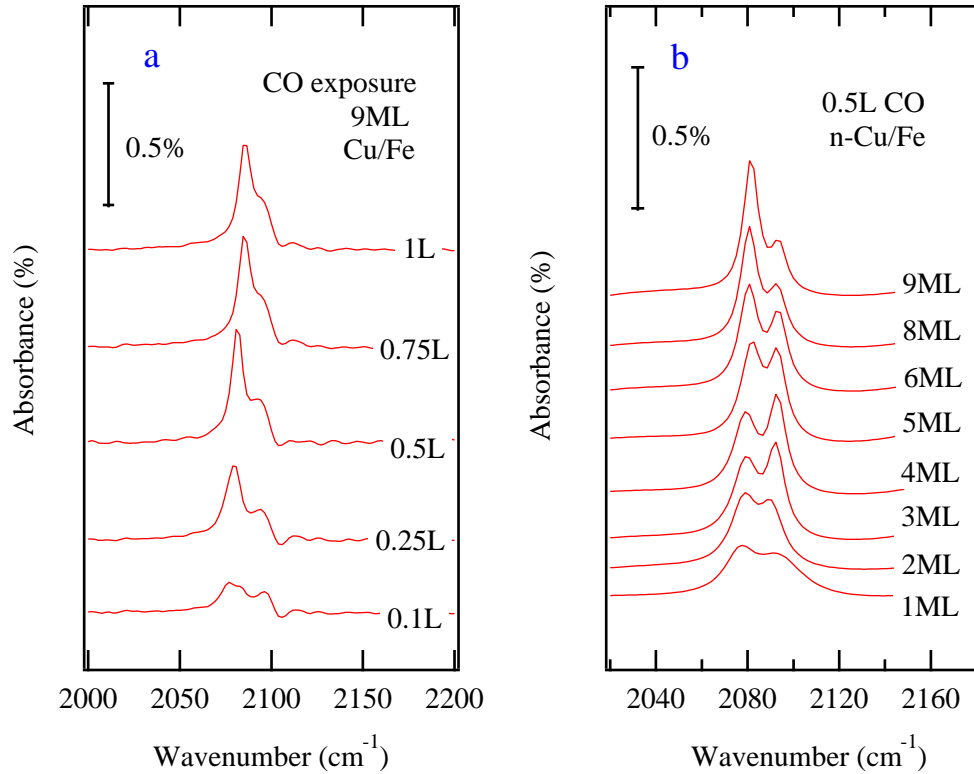


Figure 5.3: FTIR spectra obtained from Cu/fcc-Fe/Cu(100) system: (a) shows FTIR spectra of CO covered 9 ML Cu film at different exposures at 110 K, (b) shows FTIR spectra obtained from 0.5 L CO covered Cu films of different thickness at 110 K.

single crystal Cu(100) surface, CO forms a $c(2 \times 2)$ ordered structure and occupies mainly atop sites with the characteristic infrared band in the 2100 cm^{-1} region [137].

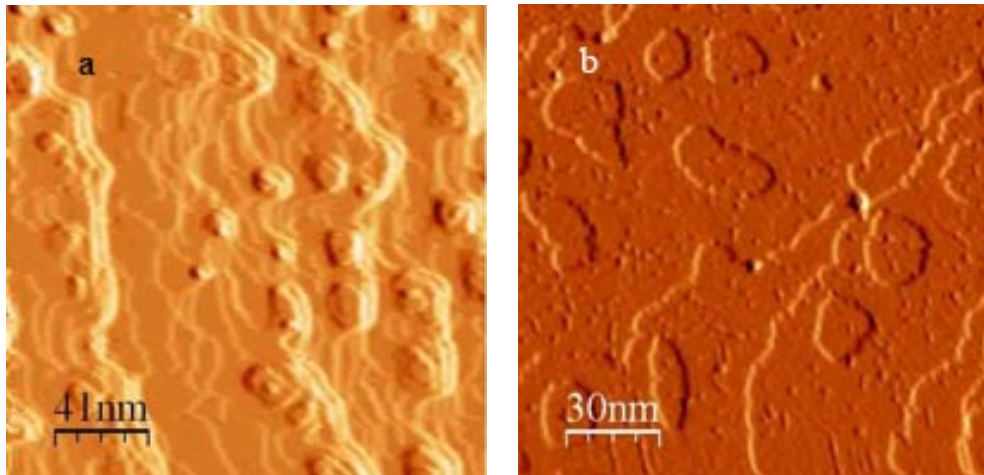


Figure 5.4: STM images of the Cu/fcc-Fe/Cu(100) surface: (a) shows image of 2ML Cu film (b) shows image of 4ML Cu film. All images were recorded at a sample bias of +1.5 V and a tunnelling current of 1 nA.

Figure 5.3 (a) shows a series of FTIR spectra in the region of the CO stretch vibration for the Cu/fcc-Fe/Cu(100) MQW system of different exposures: from 0.1 L up to 1 L, and Fig. 5.3 (b) shows a FTIR spectra of 0.5 L CO covered copper films of different thicknesses.

For all exposures, two features are observed in the FTIR spectrum: one is a peak at 2080 cm^{-1} , and the second peak at 2095 cm^{-1} . Experimental observations indicate that the high frequency feature survives after the copper substrate is annealed above 180 K, which is the desorption temperature of CO bonded at terrace sites [67]. Theoretical models [102, 103] also suggest that there is a charge donation from the CO 5σ orbital, which is antibonding with respect to the C-O bond, to the copper d -band, thereby making the C-O stretch vibrational mode stiffer upon adsorbing at copper step edges. Based on these experimental and theoretical considerations, we can associate the first peak at 2080 cm^{-1} with terminally bonded CO to the surface, and the second peak at 2095 cm^{-1} with CO bonded to step or defect sites previously identified for single crystal copper surfaces.

As we see from the Fig. 5.3, the higher energy mode grows into a shoulder with

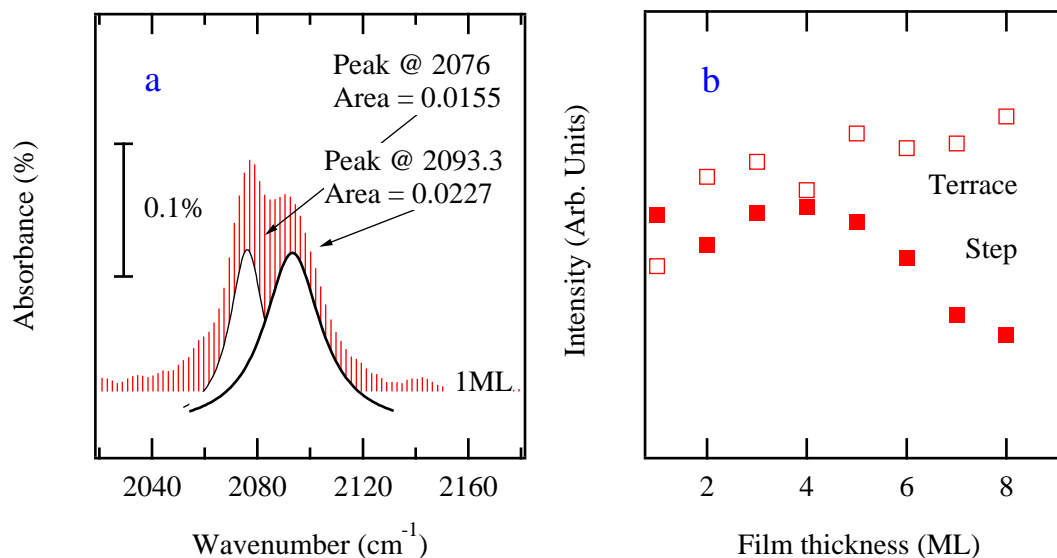


Figure 5.5: FTIR spectra peak intensities vs Cu film thickness for Cu/fcc-Fe/Cu(100) system: (a) shows the Lorentzian fit of FTIR spectrum obtained for 1 ML Cu film and (b) shows fitted terrace and step site intensities as a function of Cu film thickness

increasing exposure as the terminal site mode intensity increases and shifts to higher frequency. This blueshift in frequency is a result of the dipole-dipole interaction among the molecules on the surface, which was also observed for CO adsorption on single crystal Cu(100) surfaces [138, 139, 140]. The positive frequency shift with increased coverage seems to be the universal behavior for all metals considered in this thesis, the only difference is that the blueshift for copper is smaller compared to cobalt or nickel. This is because the chemical shift discussed in chapter 3 opposes the dipole-dipole coupling shift and reduces the overall blueshift in copper, whereas in the case of nickel and cobalt it was an additional contributor to the frequency blueshift. Again, this can be understood within the Blyholder model, where growing competition between increasing number of adsorbed molecules for donating 5σ electrons to metal reduces CO-metal bond and weakens the C-O stretch vibrational frequency, due to the slightly antibonding character of 5σ orbital.

In a quantitative spectral analysis carried out by Borguet et al. [67], site-specific concentrations of adsorbed CO molecules on the vicinal Cu(100) surface were computed. In that study the step site population accounted for only $\sim 7\%$ of the total number of CO molecules at saturation coverage, assuming that vibrational polarizabilities were equal for both types of molecules [141]. Despite such a relatively small concentration, the step-site CO contribution to the infrared absorbance signal is significant and accounts for $\sim 30\%$ of total FTIR intensity, as dynamical dipole coupling between step and terrace sites enhances the intensity of step-site CO molecules. Moreover, from Fig. 5.3 (b) we see changes in the relative terrace and step site intensities as a function of Cu film thickness. In order to get a quantitative assessment of this behavior, we performed the Lorentzian curve fit of each IR spectrum (Fig. 5.5 (a)) and analyzed the step and terrace CO intensities, which are plotted on figure 5.5 (b). For the specific thickness of 4ML Cu, where first MQW state crosses the Fermi level, the step-site intensity reaches its maximum and then diminishes with further increase in thickness. One might attribute this variation merely to changes in surface roughness, where increased number of step and defect sites increases FTIR intensity of CO vibrational mode, which is attributed to these sites. In order to check the validity of this assumption, we investigated the Cu/fcc-Fe/Cu(100) system using scanning tunnelling microscopy (STM). Figure 5.4 shows STM images of clean copper films of different thicknesses: 2 ML, with area of $41 \times 41 \text{ nm}^2$ (Fig. 5.4 (a)), and 4 ML, with area of $30 \times 30 \text{ nm}^2$ (Fig. 5.4 (b)), where flat terraces and mesas are seen separated by atomic height steps. As we see, the STM images obtained from different thicknesses of copper do not show a particularly rough surface for 4ML films. This rules out the possibility that the increase in FTIR intensity of CO step sites for a 4 ML film can be attributed to changes in Cu surface roughness.

From the analysis given above it is very suggestive that by modulating electronic structure, QSEs play an important role both in oscillating changes of TPD peak T_d and in bonding site absorbance intensities of FTIR spectra; a result of modulating

the CO-CO coupling on the Cu/fcc-Fe/Cu(100) surface. Although the specifics of how QSEs modify step and terrace absorbance intensities remains unclear and it requires better systematic analysis of CO/Cu/fcc-Fe/Cu(100) system. It was not accounted in this thesis due to the time limitations, but might be a future direction of research.

5.4 DMDS adsorption on Cu/fcc-Fe/Cu(100) system: results and discussion

In this section we will give a review of experimental results obtained from studies of dimethyl disulfide (DMDS) adsorption on single crystal Cu(100) as well as on Cu/fcc-Fe/Cu(100) MQWs. There is clear experimental evidence that upon adsorbing on the Cu(100) surface, the DMDS molecule splits into two methanethiol radicals via breaking the sulfur-sulfur bond [142]. Methanethiol is a model system of self-assembled monolayers (SAMs), the simplest molecule among alkylthiolates ($\text{CH}_3(\text{CH}_2)_n\text{S}-$) which has been the subject of many scientific investigations [143, 144]. From the technological

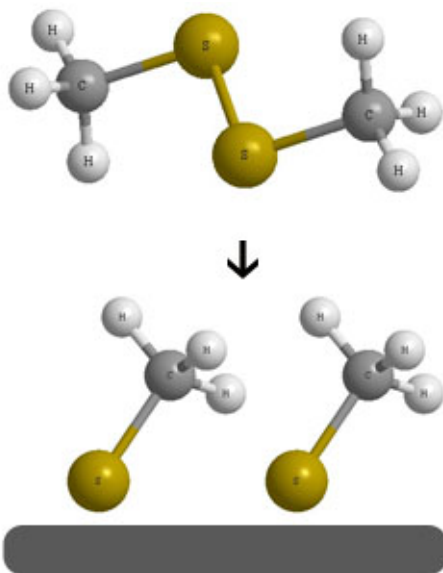


Figure 5.6: Schematic view of methanethiolate formation on Cu(100) surface. A strong S-Cu interaction splits the DMDS molecule into two and methanethiol radicals attach to copper.

point of view, SAMs are regarded as very important materials in the emerging field of molecular electronics [145, 146]. The use of different metal substrates as well as metal thin films including MQW structures can give important hints about the molecule-metal interaction mechanisms. Copper MQWs are good candidates for such investigations,

because Cu MQW states seem to overlap with sulfur-copper antibonding states, experimentally observed in the paper of Bussolotti et al. [134]. Moreover, to address the interface interaction mechanisms leading to self-assembly, detailed studies of the chemisorption processes of methanethiols offer good opportunity to understand other sulfur head group organic molecules, like aromatic benzene-thiolates. As already mentioned in case of DMDS adsorption on Cu at room temperature, the sulfur-sulfur bond breaks and the sulfur head group attaches itself to the Cu surface forming an ordered layers of methanethiolate. This process is demonstrated schematically on Fig. 5.6. Such decomposition of the DMDS molecule is reported for temperatures as low as 140

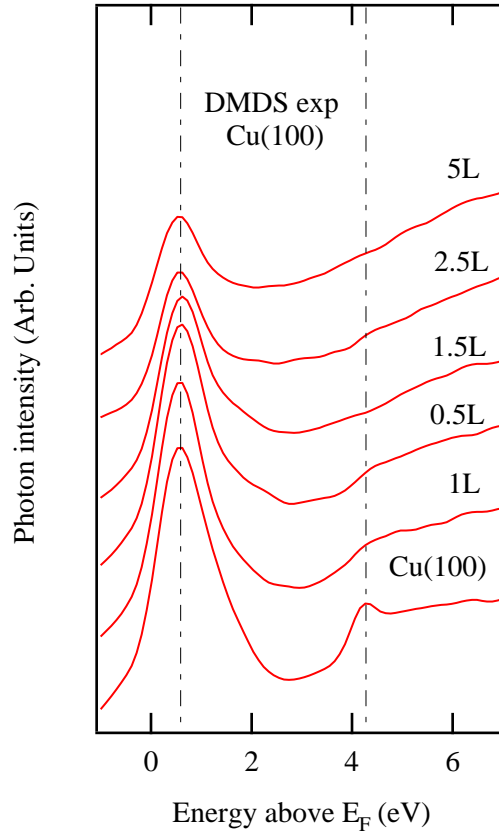


Figure 5.7: IPE spectra from the DMDS/Cu/fcc-Fe/Cu(100) system. Each spectrum is plotted as a function of energy above the Fermi level and corresponds to a different DMDS exposure.

K, although at 4.7 K, STM measurements revealed non-dissociative adsorption showing that the dissociation is a temperature-activated process [147]. Studies revealed that dissociative adsorption on copper is true for certain thiolates, but not always. For example the adsorption of benzenethiol on Cu(100) at room temperature is accompanied only by deprotonation of thiol head group [148].

5.4.1 Electronic structure

Inverse photoemission results from methanethiolate/Cu(100) surface are reported in Fig. 5.7. The figure shows a series of IPE spectra obtained from a Cu(100) when the surface was exposed to increasing amounts of DMDS at room temperature. Compared to the clean Cu(100) spectrum, the IPE spectra from DMDS-exposed Cu(100) surface are almost featureless. The unoccupied Cu *sp* state seems to be strongly suppressed upon exposure and the image state disappears even at low coverages of methanethiol, but no new features are observed. With increasing exposure, a very broad feature grows at about 5-6 eV above E_F , similar to what we have seen for the CO $2\pi^*$ level, but less well defined. In order to find out the origin of this feature and also get information about the occupied and unoccupied density of states (DOS) of this system, we performed density functional theory (DFT) calculations using the GAMESS package [149, 150] for both unsupported methanethiol and the methanethiol - single Cu atom system.

Figure 5.8 shows calculated DOS for methanethiol - single Cu atom complex. The red lines indicate corresponding energies of calculated orbitals, and the blue curve is the gaussian fit of the same orbital energies to reveal the characteristic spectral features of the system. From the plot we see the presence of two main occupied features near the Fermi level: one of them spans the energy range from -2.5 to -1 eV and represents an antibonding S 3*p* - Cu 3*d*_{*xy,yz*}, S 3*p* - Cu 3*d*_{*z*²} orbitals, while the second feature centers at -5.5 eV and represents S 3*p* - Cu 3*d*_{*xy,yz*}, S 3*p* - Cu 3*d*_{*z*²} bonding orbitals. The energy

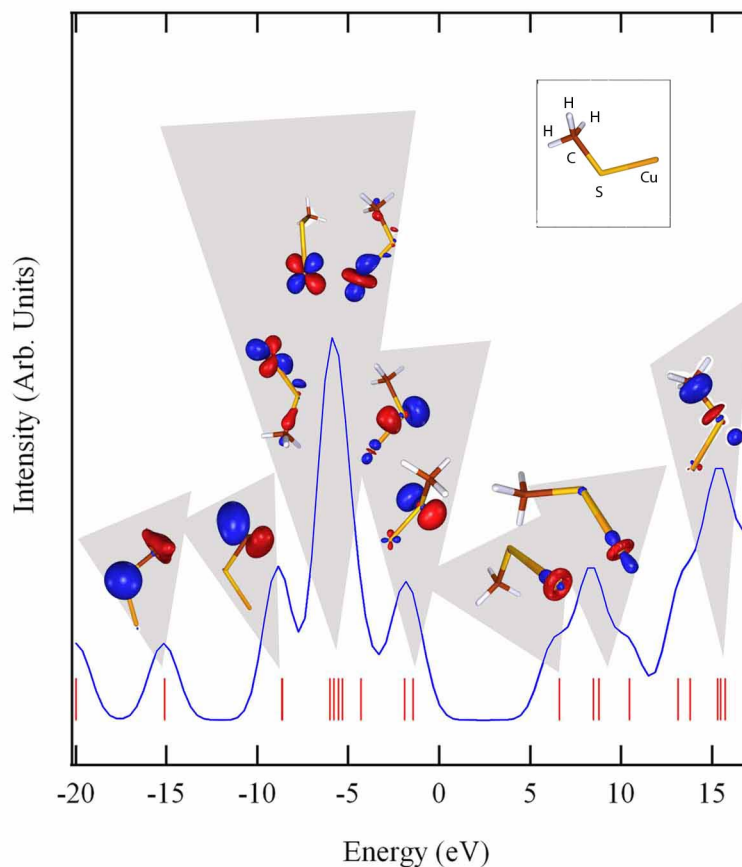


Figure 5.8: Calculated occupied and unoccupied density of states (DOS) for methanethiol - single Cu atom. The Fermi level is adjusted to match the experimental data

positions of each feature relative to Cu *d* bands which are located between -1.5 and -4 eV [151, 134] are also indicative of sulfur-copper bond formation, which has the antibonding state slightly above the Cu *d* band and the bonding state slightly below the Cu *d* band. The low energy occupied features at -9 eV and -15 eV in the Fig. 5.8 are associated with the carbon-hydrogen and sulfur-carbon orbitals respectively. The lowest unoccupied feature above 5 eV most likely corresponds to sulfur-copper hybrid state. Our calculated results are consistent with angle resolved ultraviolet photoemission spectroscopy (UPS) studies of methane-thiol/Cu(100) system by Bussolotti et al. [134], which revealed S-Cu related features in the photoemission spectra. Namely the comparison of different

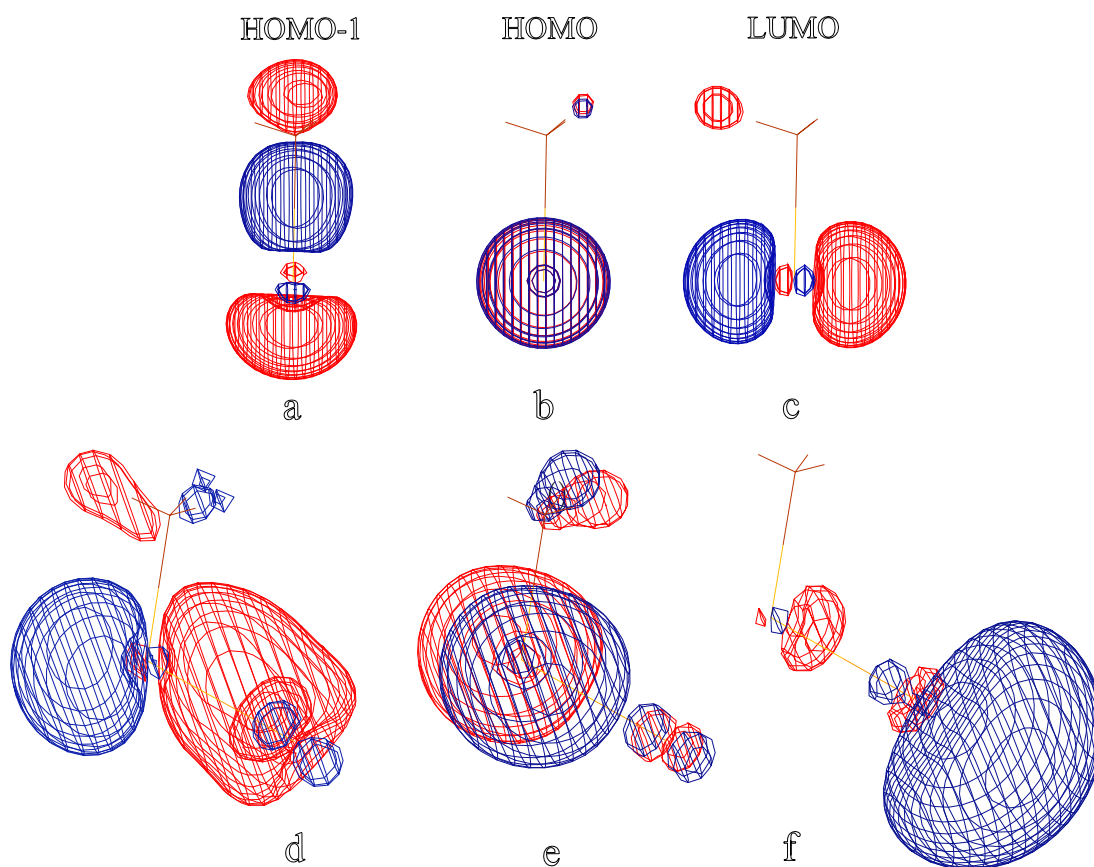


Figure 5.9: Electronic orbitals of unsupported methanethiol and methanethiol - single Cu atom system: a,b,c represent HOMO-1, HOMO and LUMO orbitals of unsupported methanethiol radical; d,e,f are HOMO-1, HOMO and LUMO orbitals of Cu-methanethiol respectively.

phases of methanethiolate to physisorbed and gas phase DMDS UPS spectra showed features in the -6 to -5 eV range below E_F attributed to bonding S $3p$ - Cu $3d/4s$ hybrid states and at ~ 1.5 eV an antibonding feature of the same S $3p$ - Cu $3d/4s$ origin.

Two main features can be seen in the unoccupied spectrum of calculated methanethiol - single Cu atom complex: The first feature is presented by sulfur-copper orbitals and it is positioned between 5 and 10 eV above the Fermi level. This explains the broad feature observed in experimental IPE spectra. The second feature is about 15 eV above the Fermi level and presents mostly the carbon-sulfur and hydrocarbon orbitals.

DFT calculations were performed for both unsupported methanethiol and methanethiol - single Cu atom system, to visualize the molecule-metal bonding character. Calculated orbitals are presented in figure 5.9, where 5.9 (a), 5.9 (b) and 5.9 (c) images correspond to HOMO-1, HOMO and LUMO orbitals of unsupported methanethiol molecule and 5.9 (d), 5.9 (e), 5.9 (f) images are HOMO-1, HOMO and LUMO orbitals of Cu-methanethiol respectively. Figures 5.9 (a) and 5.9 (f) show that the σ -like orbital of methanethiol (HOMO-1 5.9 (a)) donates its electrons to Cu d_{z^2} levels and becomes unoccupied (LUMO 5.9 (f)), while the π -like, initially empty orbital (LUMO 5.9 (c)) becomes hybridized with Cu $d_{xy,yz}$ state and becomes occupied (HOMO-1 5.9 (d)). This type of behavior is somewhat similar to CO-metal bonding character, where molecule-metal bond formation happened by electron donation from σ molecular orbital to metal and backdonation from metal to CO π orbital.

As we see this simple model of methanethiol - single Cu atom system can explain some experimentally observed features, namely the unoccupied feature at about 5 eV above E_F and occupied features below the Fermi level related to the carbon-sulfur bond. Of course, we are well aware of the fact that that molecule interacts with a periodic array of Cu surface atoms, not with just single Cu atom. Nevertheless, this model still gives a good qualitative understanding of the bonding of the methanethiol to the Cu surface and an account of the spectroscopic data obtained from it. As a consequence,

copper cluster or slab model DFT calculations are required in order to have better agreement with experimental results, but such elaborate calculations are beyond the scope of this thesis.

5.4.2 Geometric structure

STM and LEED studies of an alkylthiolate SAM formed on the Cu(111) surface revealed a strong tendency of the molecules to distort the local atomic arrangement of the Cu(111) surface and occupy hollow adsorption sites with four-fold coordinated symmetry [152]. This indicates a stronger adsorption of alkylthiols on the Cu(111) surface than on Au(111), where theoretical calculations indicate that bridge and fcc sites are more favorable for CO adsorption [153, 154, 155]. These theoretical calculations also predict a $\sim 53^\circ$ tilt of S-C bond from surface normal. Significant tilt of the S-C bond was also observed by Allegretti et al. [144] investigating benzenethiolate on Cu(100) with the photoelectron diffraction technique. It turns out that in the case of Cu(111), the strength of the sulfur-copper interaction can cause a local (100) surface reconstruction in order to satisfy the ideal adsorption geometry [152]. Scanning tunnelling microscopy (STM) measurements have shown that this reconstruction of the (111) surface is independent of the alkyl-chain length, which indicates that the sulfur atoms play dominant role in inducing a re-ordering of the copper surface, whereas alkyl-chains seem to play a minor role. As the reconstructed Cu(100) surface offers 4-fold binding sites, one can imagine that no re-ordering of Cu atoms is necessary on the single crystalline Cu(100) surface to accommodate the alkanethiolate adsorption. However, studies of the Cu(100) surface [156, 157] have shown a local rearrangement of the Cu(100) surface after the adsorption of the alkanethiolate of different chain length at room temperature. As the sulfur-reconstructed local (100) layer of Cu(111) surface has inter-atomic lateral spacing $\sim 14\%$ larger than on a Cu(100) surface [156, 157], adsorption onto Cu(100)

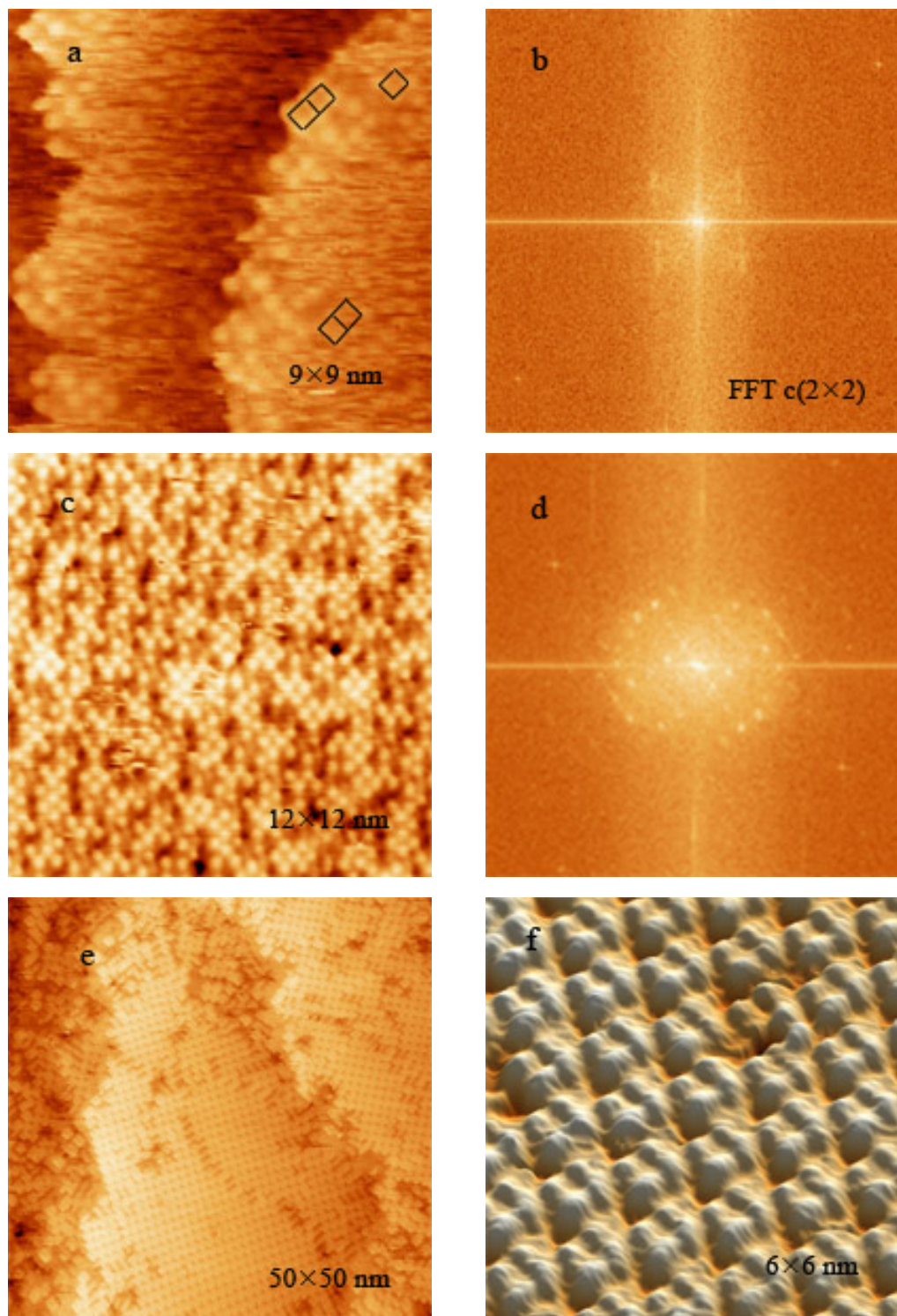


Figure 5.10: STM images of the DMDS/Cu(100) surface. (a) is an image of low coverage phase of DMDS/Cu, (b) is a FFT of (a). (c) is an image of DMDS/Cu surface at high coverage of DMDS, (d) is a FFT of (c). (e) shows STM image of annealed DMDS/Cu surface and (f) is a close-up image of (e).

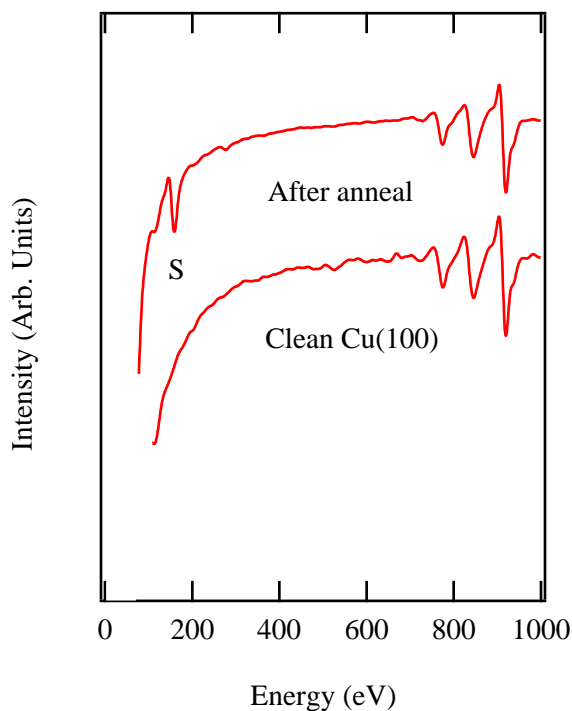


Figure 5.11: Auger spectrum obtained from annealed DMDS/Cu(100) and Cu(100) surfaces: Strong sulfur signal is present for DMDS/Cu(100) system

leads to a substantial adsorbate-induced surface stress. As a result, it is not possible to form a well-ordered $c(2 \times 2)$ thiolate overlayer on an extended Cu(100) surface. In fact, our STM study of methanethiolate on Cu(100) confirmed this assumption, revealing only small islands of ordered overlayer structure. Figure 5.10 shows STM images of the methanethiolate overlayers formed on Cu(100) surface after different DMDS exposures. Figure 5.10(a) was obtained for low exposures ($\sim 3L$). It shows small islands of ordered structures, as indicated with black squares, and it was recorded at a sample bias of -2 V and a tunnelling current of 0.8 nA. By measuring the distances between individual features and knowing orientation and lattice spacing of the Cu substrate, we could identify local $c(2 \times 2)$ ordering. Fig. 5.10 (b) is a Fourier transform (FFT) image of the Fig. 5.10 (a) that also confirms the $c(2 \times 2)$ ordering. The ordered regions of methanethiol are co-existing with areas of disordered clusters and apparent vacancies,

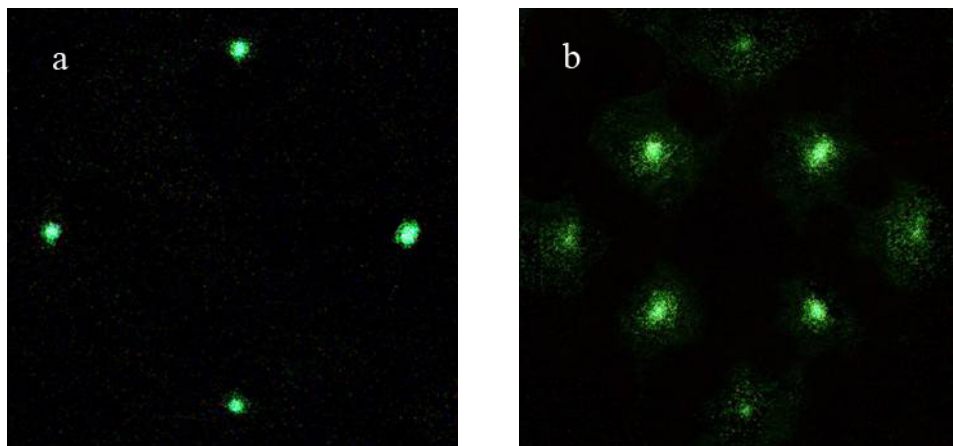


Figure 5.12: LEED image of the DMDS/Cu(100) surface: (a) shows image of Cu(100) (b) shows image of 3 L dimethyl disulfide on Cu(100)

which are expected to allow local strain and overall stress relief. This result is broadly consistent with STM studies of DMDS/Cu(100) system by Driver and Woodruff [157]. In the same paper, the STM images show a transformation into a well-ordered $c(2 \times 6)$ phase at sufficiently high adsorbate exposures on the (100) surface. Fig. 5.10 (c) show a STM image of well-ordered high coverage phase (~ 10 L) and Fig. 5.10 (d) displays its FFT. As we see from the image, high coverage phase is not a simple $c(6 \times 2)$ structure, but rather complicated state, alternative to the $c(6 \times 2)$ phase observed in the literature [157, 152, 144].

In their interpretation of the $c(6 \times 2)$ structure, Driver and Woodruff attributed this phase to the periodic buckling of the copper substrate caused by surface tension [157] followed by significant dissociation of methanethiolate and sulfide formation on the Cu surface. It has been suggested that at high coverage the local rearrangement of the surface can modify the strength of the sulfur-carbon bond, favoring its breaking and the coexistence of thiolate and sulphide species. In order to see the effect of dissociation on surface structure, we annealed the substrate up to 600 K. As a result a scission of the S-C bond and complete desorption of methane radicals has been observed. Figures

5.10 (e) and 5.10 (f) show STM images of the annealed methanethiolate films. Fig. 5.10 (e) reveals very well-ordered structure on Cu(100) surface, recorded at a sample bias of +1 V and a tunnelling current of 0.5 nA. Fig. 5.10 (f) shows a close-up image of Fig. 5.10 (e). This type of re-ordering is characteristic to sulfur induced reconstructed Cu(100) surfaces, also has been seen in STM measurements of H₂S covered Cu(100) single crystal [158]. To test this hypothesis we performing Auger electron spectroscopy (AES) measurements after annealing the Cu(100) substrate. AES indicates a strong sulfur signal after methane desorption at about ~ 450 K as seen on Fig. 5.11.

In addition to STM experiments we performed low energy electron diffraction (LEED) studies of DMDS/Cu(100) system. The LEED pattern of clean Cu(100) is presented in Fig. 5.12 (a), while Fig. 5.12 (b) shows the (2×2) reconstruction for a methanethiolate adsorbed on Cu(100). Our LEED results are in agreement with the STM observations at low coverage of methanethiol, also showing $c(2 \times 2)$ ordering, however we were unable to see a $c(6 \times 2)$ saturation structure at high coverage, as often reported from STM measurements [157, 152, 144]. With the increasing DMDS coverage, an increase in the diffused background obscured diffraction spots in LEED pattern, which are indications of diminishing order on the surface. Dissociation of methanethiolate via breaking the S-C bond and losing its methyl tail is highly possible, since DMDS is very fragile to electron beam damage and dissociates even under the presence of high energy UV radiation [159].

5.4.3 TPD and FTIR results

FTIR and TPD studies are our next experimental procedures to investigate DMDS adsorption on copper. The existing experimental results about the vibrational modes of gas phase dimethyl disulfide molecule and methanethiol/Cu(100) system are reported in Table 5.1 [160, 161]. There is a good agreement between the gas phase DMDS and

methanethiol/Cu(100) vibrational features, and from Table 5.1 one can identify S-C stretch ($\nu(\text{C} - \text{S})$), methyl rock ($\rho_r(\text{CH}_3)$), two methyl bends ($\rho_s(\text{CH}_3)$, $\rho_a(\text{CH}_3)$) and the C-H stretch ($\nu(\text{C} - \text{H})$) frequencies. A small difference has been seen for S-C stretch and CH_3 bend and rock frequencies, while C-H stretch frequency seems to be the same for both systems. This is slightly ($\sim 15\text{cm}^{-1}$) different from the C-H stretch frequency measured by us at saturation exposure, the coverage dependence of which we will discuss below.

Figure 5.13 (a) shows a series of FTIR spectra in the region of the C-H symmetrical stretch mode for the increasing exposure of DMDS vapor on a clean Cu(100) surface. For the lowest methanethiol coverages the spectrum is dominated by a peak at 2930 cm^{-1} , which gradually decreases in frequency as a function of increasing DMDS exposure to a value of 2915 cm^{-1} at saturation coverage, corresponding to a total of 3 L DMDS exposure. This type of behavior could be a result of dipole-dipole interactions between methanethiol molecules, similar to what we observed for the CO molecule adsorption on copper. The only difference now is that the frequency undergoes a redshift instead of a blueshift as was seen in the case of C-O stretch frequency. Figure 5.13 (b) shows an FTIR spectra at saturation coverage obtained for Cu/fcc-Fe/Cu(100) MQW system of various thicknesses. For all thicknesses the frequency of the C-H symmetrical stretch mode stays unchanged, while the width of the peak increases for thicker copper films. Lineshape changes can be indicative of vibrational lifetime change, which is dependent on molecule-molecule and molecule-surface interactions. Understanding of these interactions require further investigations of methanethiol/Cu thin film system. In particular, FTIR investigations of the S-C vibrational modes would be particularly fruitful, since S-C bond strength might be affected by changing sulfur-metal bond. The S-C stretch vibrational mode has low frequency ($\sim 680\text{ cm}^{-1}$) and so far we were limited by the type of FTIR detector, which can not detect the low frequency range of infrared spectrum.

Vibrational mode	Gas phase DMDS	methanethiol/Cu(100)@RT
$\nu(\text{C} - \text{S})$	690 cm^{-1}	680 cm^{-1}
$\rho_r(\text{CH}_3)$	952 cm^{-1}	960 cm^{-1}
$\rho_s(\text{CH}_3)$	1313 cm^{-1}	1320 cm^{-1}
$\rho_a(\text{CH}_3)$	1433 cm^{-1}	1450 cm^{-1}
$\nu(\text{C} - \text{H})$	2930 cm^{-1}	2930 cm^{-1}

Table 5.1: Vibrational modes of DMDS and methanethiol/Cu(100) system: data was obtained for gas phase DMDS using FTIR [161] and for methanethiol/Cu(100) using electron energy loss spectroscopy (EELS) [160].

As we have already discussed, DMDS adsorption on Cu(100) is dissociative at room temperature (RT) leading to the formation of methanethiol layer. Further heating of the copper substrate breaks the S-C bond and different types of hydrocarbons desorb from the surface. TPD measurements reported in literature [156] indicate a very broad desorption feature peaking at about 465 K, after which a sulfur contaminated Cu surface has been seen in Auger spectroscopy. In TPD studies of the methanethiol/Cu(100) system by Sexton and Nyberg [160] two desorbing species, methane and ethane, were observed at about 430 K, with no apparent H_2 desorption. From the stoichiometric equations they concluded that some carbon stays on the surface as traces of it has been seen in the experiment. In contrast, we do not detect a significant amount of carbon, apart from the small amount of ambient carbon, which is always present in the UHV system, but we see other desorbing hydrocarbons like ethylene, which were not reported in this previous study. It seems that methyl-methyl, methyl-hydrogen recombination processes are combined with other complicated reaction channels, where dehydrogenation of ethane and ethylene desorption occurs from the surface, without releasing molecular hydrogen.

A series of TPD spectra are given in figure 5.14 (a). The figure displays the methane desorption results of TPD measurements from 1 L DMDS adsorbed onto

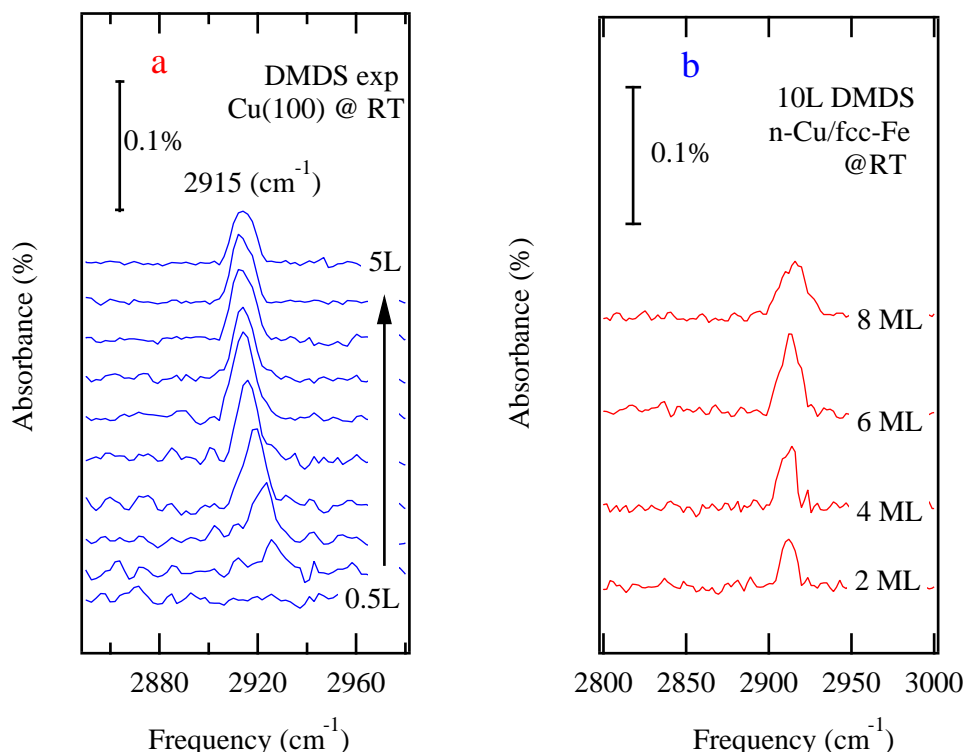


Figure 5.13: FTIR spectra from the DMDS/Cu/fcc-Fe/Cu(100) system at room temperature: a) represents spectra for different DMDS exposures on Cu(100), b) represents 5 L DMDS exposure on Cu/fcc-Fe/Cu(100) films of various thickness.

Cu/fcc-Fe/Cu(100) system. Copper films of different thicknesses were prepared at room temperature: the thickness of the copper film is indicated by the appropriate number on each curve. Although different hydrocarbons seem to desorb at same temperature, methane has been chosen as a probing desorption species because it gives a larger signal in the measured mass spectrum. As we see, thinner Cu films have a lower desorption temperature $T_d=385$ K for 1 ML Cu, compared to thicker films ($T_d=420$ K) and it is also lower than similar methane desorption peak from Cu(100) single crystal by ~ 30 K as seen in Fig. 5.14 (b). No apparent changes occur in the TPD feature for the Cu films thicker than 5 ML, moreover, T_d stays unchanged, but at a value different from that found for adsorption on the single crystal Cu(100) even for films as thick as 18 ML. The reduction of desorption temperature is an indication of underlying substrate

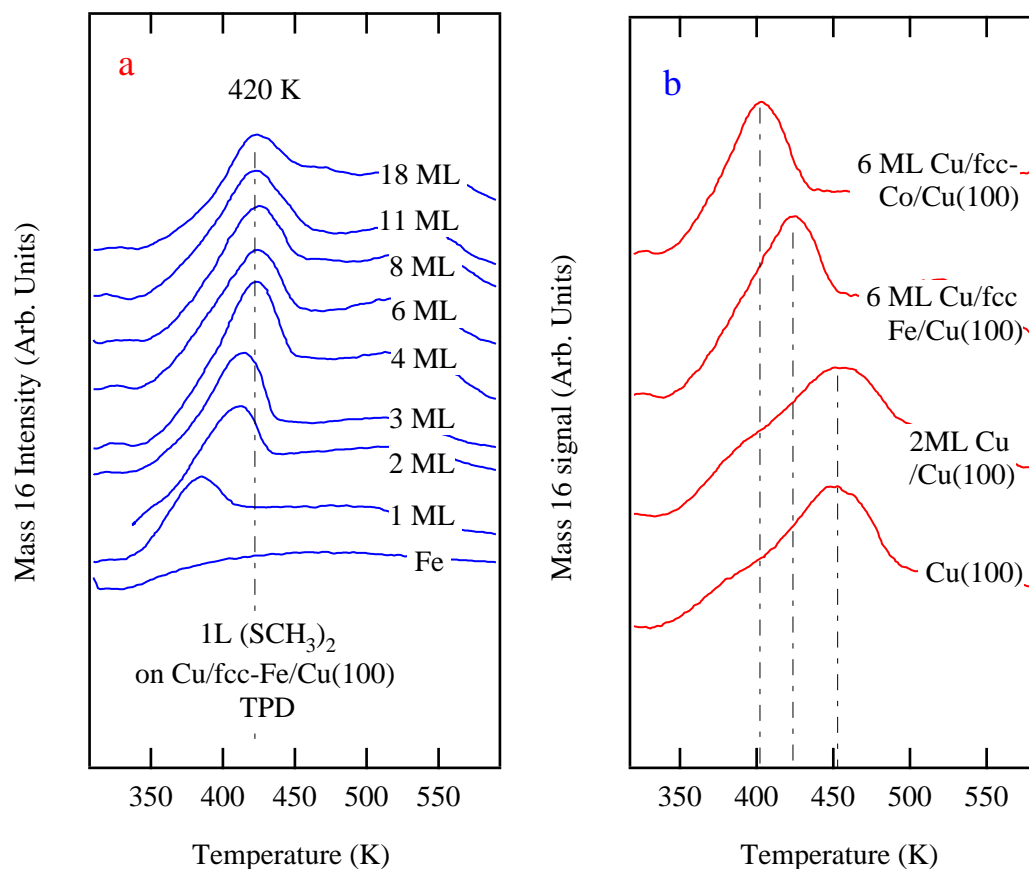


Figure 5.14: Methane desorption from the surface of the Cu films preexposed to DMDS: a) 1 L DMDS exposure on n-Cu/fcc-Fe/Cu(100) system; b) 1 L DMDS exposure on Cu films grown on different substrates.

effect, similar to what we observe in case of CO adsorption on the Cu/fcc-Fe/Cu(100) system (Sec. 5.3), when changes in the copper thin film d-band structure undermined the charge donation from CO 5σ orbital, resulting in the overall T_d reduction by ~ 7 K. This time the effect is stronger, due to the stronger SCH_3 -Cu interaction compared to CO-Cu. In order to further underline that this is a substrate effect, we grew Cu thin films on fcc-Co/Cu(100) and on Cu(100). The corresponding TPD curves are plotted in figure 5.14 (b). Methane T_d seems to be reduced even more for Cu/fcc-Co, while for Cu/Cu(100) it remains the same. The obtained result is somewhat expected, since the difference between the fcc cobalt and copper lattice parameters is bigger than difference

between copper and fcc iron. Finally, it is important to keep DMDS coverage low in order to avoid Cu surface buckling and other effects.

5.5 Summary

CO and DMDS chemisorption properties of the Cu/fcc-Fe/Cu(100) MQW system were investigated using inverse photoemission spectroscopy (IPE), temperature programmed desorption (TPD) and reflection-absorption infrared (FTIR) spectroscopy and scanning tunneling microscopy (STM).

As a result, modification of CO chemisorption properties due to the presence of MQW states was observed. For increasing thickness of Cu on the fcc-Fe/Cu(100) surface, MQW states periodically cross and modulate IPE intensity at Fermi level. Changes in the peak temperature of TPD spectra are correlated with these modulations of IPE intensity. In addition to this overall reduction of the T_d of CO from the Cu overlayers was observed compared to T_d of CO on the single crystal Cu(100) surface. The last effect is similar to what we have already seen in case of Ni/Cu(100) MQW system and it was attributed to compressive strain in the copper overlayer. FTIR shows two adsorption sites in CO spectra, which are identified as CO adsorbed on terraces and steps. Most interestingly, the modulating electronic structure affects terrace and step site absorbance intensities, suggesting the correlation between intensities of these two spectral features and MQW states crossing the Fermi level, which is a very interesting result requiring further more detail investigations.

Upon adsorbing on Cu(100) surface the DMDS molecule splits into two methanethiol radicals as the sulfur head group attaches itself on the Cu surface and forms ordered layers of methanethiolate SAMs. STM studies revealed different phases of ordered structures, which depend on the DMDS coverage. Electronic structure investigations show ~ 5 and 5.5 eV features attributed to bonding S $3p$ - Cu $3d/4s$ hybrid states and

~ 1.5 eV antibonding feature of the same S $3p$ - Cu $3d/4s$ origin. Methanethiol-Cu bond formation is a result of electron donation from S $3p$ - C $2p$ sigma orbital to Cu d_{z^2} -band and backdonation from Cu $d_{xy,yz}$ -band to S-C π . Overall reduction of the desorption temperature T_d of methane from the Cu overlayers grown on iron or cobalt was observed compared to single crystal Cu(100) surface, attributed to the underlaying substrate effects and changes in d-band structure of the copper overlayer.

Appendix A

List of Acronyms

AES	Auger electron spectroscopy
BZ	Brillouin Zone
CMA	Cylindrical Mirror Analyzer
CO	Carbon Monoxide
DMDS	Dimethyl disulfide
DOS	Density of States
E_F	Fermi energy
FTIR	Fourier transform infrared
GM	Geiger Müller
GMR	Giant magnetoresistance
HOMO	Highest occupied molecular orbital
IPE	Inverse photoemission
LEED	Low energy electron diffraction
LT	Low temperature
LUMO	Lowest unoccupied molecular orbital
ML	Monolayer
MQW	Metallic quantum well
PAM	Phase accumulation model
QCM	Quartz crystal microbalance
QSE	Quantum size effect
RBS	Rutherford backscattering spectrometry
RT	Room temperature
STM	Scanning Tunnelling Microscopy
TPD	Temperature programmed desorption
UPS	Ultra-Violet Photoemission Spectroscopy
UHV	Ultra High Vacuum
XPS	X-ray photoemission Spectroscopy

References

- [1] H. YAO, *Unoccupied electronic structure and CO chemisorption properties of ultrathin Ni films on Cu(100)*, PhD thesis, Rutgers University, 2006.
- [2] Materials Sciences Division of LBNL,
<http://physics.berkeley.edu/research/crommie/index.html>.
- [3] G. J. MANKEY, R. F. WILLIS, and F. J. HIMPSEL, *Phys. Rev. B* **48**, 10284 (1993).
- [4] J. LAUTERBACH, M. WITTMANN, and J. KUPPERS, *Surf. Sci. (Netherlands)* **279**, 287 (1992).
- [5] M. BAIBICH, J. BROTO, A. FERT, F. NGUYEN VAN DAU, F. PETROFF, P. ETIENNE, G. CREUZET, A. FRIEDERICH, and J. CHAZELAS, *Physical Review Letters* **61**, 2472 (1988).
- [6] P. ALLEN, *Solid State Communications* **102**, 127 (1997).
- [7] A. CHO and J. ARTHUR, *Prog. Solid State Chem. (UK)* **10**, 157 (1975).
- [8] M. WUTTIG and J. THOMASSEN, *Surface Science* **282**, 237 (1993).
- [9] J. CERDA, P. DE ANDRES, A. CEBOLLADA, R. MIRANDA, E. NAVAS, P. SCHUSTER, C. SCHNEIDER, and J. KIRSCHNER, *Journal of Physics: Condensed Matter* **5**, 2055 (1993).
- [10] T. CHIANG, *Surface Science Reports* **39**, 181 (2000).
- [11] A. DANESE, D. ARENA, and R. BARTYNSKI, *Progress in Surface Science* **67**, 249 (2001).
- [12] S. PARKIN, N. MORE, and K. ROCHE, *Physical Review Letters* **64**, 2304 (1990).
- [13] S. PARKIN, R. BHADRA, and K. ROCHE, *Physical Review Letters* **66**, 2152 (1991).
- [14] J. ORTEGA and F. HIMPSEL, *Physical Review Letters* **69**, 844 (1992).
- [15] J. ORTEGA, F. HIMPSEL, G. MANKEY, and R. WILLIS, *Physical Review B* **47**, 1540 (1993).
- [16] M. BAIBICH, J. BROTO, A. FERT, F. NGUYEN VAN DAU, F. PETROFF, P. ETIENNE, G. CREUZET, A. FRIEDERICH, and J. CHAZELAS, *Physical Review Letters* **61**, 2472 (1988).
- [17] J. BARNAS, A. FUSS, R. CAMLEY, P. GRUNBERG, and W. ZINN, *Physical Review B (Condensed Matter)* **42**, 8110 (1990).

- [18] C. TSANG, J. FONTANA, R.E., T. LIN, D. HELM, B. GURNEY, and M. WILLIAMS, *IBM J. Res. Dev. (USA)* **42**, 103 (1998).
- [19] C. TU, *Journal of Vacuum Science and Technology A (Vacuum, Surfaces, and Films)* **21**, 160 (2003).
- [20] T. CHIANG, *Chin. J. Phys. (Taiwan)* **43**, 154 (2005).
- [21] H. HONG, C.-M. WEI, M. CHOU, L. BASILE, H. CHEN, M. HOLT, and T.-C. CHIANG, *Physical Review Letters* **90**, 076104 (2003).
- [22] V. YEH, L. BERBIL-BAUTISTA, C. WANG, K. HO, and M. TRINGIDES, *Physical Review Letters* **85**, 5158 (2000).
- [23] S. CHANG, W. SU, W. JIAN, C. CHANG, L. CHEN, and T. TSONG, *Physical Review B (Condensed Matter)* **65**, 245401 (2002).
- [24] M. OZER, J. THOMPSON, and H. WEITERING, *Nature Physics* **2**, 173 (2005).
- [25] A. DANESE and R. BARTYNSKI, *Physical Review B (Condensed Matter and Materials Physics)* **65**, 174419 (2002).
- [26] P. ROUS, *Physical Review Letters* **83**, 5086 (1999).
- [27] L. ABALLE, A. BARINOV, A. LOCATELLI, S. HEUN, and M. KISKINOVA, *Physical Review Letters* **93**, 196103 (2004).
- [28] A. DANESE, F. CURTI, and R. BARTYNSKI, *Physical Review B (Condensed Matter and Materials Physics)* **70**, 165420 (2004).
- [29] J. ORTEGA, F. HIMPEL, G. MANKEY, and R. WILLIS, *Journal of Applied Physics* **73**, 5771 (1993).
- [30] A. DANESE, *Metallic quantum well states and chemisorption quantum size effects in metal thin film systems*, PhD thesis, Rutgers University, 2005.
- [31] A. ZANGWILL, *Physics at Surfaces*, Cambridge University Press, 1992.
- [32] J. SINFELT, *Reviews of Modern Physics* **51**, 569 (1979).
- [33] K. KLEIN, A. MELECHKO, P. RACK, J. FOWLKES, H. MEYER, and M. SIMPSON, *Carbon (UK)* **43**, 1857 (2005).
- [34] Y. YE, C. AHN, C. WITHAM, B. FULTZ, J. LIU, A. RINZLER, D. COLBERT, K. SMITH, and R. SMALLEY, *Applied Physics Letters* **74**, 2307 (1999).
- [35] B. HAMMER, Y. MORIKAWA, and J. NORSKOV, *Physical Review Letters* **76**, 2141 (1996).
- [36] J. RODRIGUEZ and D. GOODMAN, *Science* **257**, 897 (1992).
- [37] E. WIMMER, C. FU, and A. FREEMAN, *Phys. Rev. Lett. (USA)* **55**, 2618 (1985).
- [38] G. BLYHOLDER, *Journal of Physical Chemistry* **68**, 2772 (1964).

- [39] P. BAGUS and G. PACCHIONI, *Surface Science* **278**, 427 (1992).
- [40] F. CURTI, *The electronic and Chemisorption properties of Cu/fccCo/Cu(100) metallic Quantum Wells*, PhD thesis, Rutgers University, 1999.
- [41] H. G. TOMPKINS, *Vacuum Technology: A Beginning*, AVS Education Committee Book Series, 2002.
- [42] A. ROTH, *Vacuum Technology*, Cambridge University Press, 1988.
- [43] A. TUROS and L. WIELUNSKI, *Nuclear Instruments and Methods* **104**, 117 (1972).
- [44] P. R. GRIFFITHS and J. A. DE HASETH, *Fourier Transform Infrared Spectrometry*, John Wiley & Sons, 1986.
- [45] P. NORTON, *Opto-Electronics Review* **10**, 159 (2002).
- [46] G. BAHIR, V. GARBER, and A. DUST, *Journal of Electronic Materials* **30**, 704 (2001).
- [47] P. AGNIHOTRI, C. MUSCA, and L. FARAONE, *Semiconductor Science and Technology* **13**, 839 (1998).
- [48] P. JOHNSON and S. HULBERT, *Review of Scientific Instruments* **61**, 2277 (1990).
- [49] J. PENDRY, *Journal of Physics C (Solid State Physics)* **14**, 1381 (1981).
- [50] V. DOSE, *Surface Science Reports* **5**, 337 (1985).
- [51] N. SMITH, *Vacuum* **33**, 803 (1983).
- [52] S. HUEFNER, *Photoelectron spectroscopy. Principles and applications*, 1995.
- [53] N. SMITH and F. HIMPEL, *Photoelectron spectroscopy*, 1983.
- [54] D. CLAEISSON, *Doktorsavhandlingar vid Chalmers Tekniska Hogskola*, 1 (1998).
- [55] P. HEIMANN, J. HERMANSON, H. MIOGA, and H. NEDDERMEYER, *Phys. Rev. B, Condens. Matter (USA)* **20**, 3059 (1979).
- [56] L. JOHANSSON, A. CALLENAS, P. STEFAN, A. CHRISTENSEN, and K. SCHWARZ, *Phys. Rev. B, Condens. Matter (USA)* **24**, 1883 (1981).
- [57] N. G. STOFFEL and P. D. JOHNSON, *Nuclear Instruments and Methods in Physics Research, Section A: Accelerators, Spectrometers, Detectors* **A234**, 230 (1985).
- [58] R. SHANKAR, *Principles of Quantum Mechanics*, Plenum Press, 1994.
- [59] P. JOHNSON and J. DAVENPORT, *Physical Review B (Condensed Matter)* **31**, 7521 (1985).
- [60] E. BERSCH, *Energy level alignment in metal/oxide/semiconductor and organic dye/oxide systems*, PhD thesis, Rutgers University, 2008.

- [61] W. K. SIU, *Unoccupied electronic structure of Ru(0001), Pd/Ru(0001) and Cu/fccCo/Cu(100) systems*, PhD thesis, Rutgers University, 2001.
- [62] V. DOSE, W. ALTMANN, A. GOLDMANN, U. KOLAC, and J. ROGOZIK, *Phys. Rev. Lett. (USA)* **52**, 1919 (1984).
- [63] S. HULBERT, P. JOHNSON, N. STOFFEL, W. ROYER, and N. SMITH, *Phys. Rev. B, Condens. Matter (USA)* **31**, 6815 (1985).
- [64] P. H. DAWSON, *Quadrupole Mass Spectrometry and Its Applications*, AVS Book Series, 1997.
- [65] E. DE HOFFMANN & VINCENT STROOBANT, *Mass Spectrometry: Principles and Applications, Third Edition*, Wiley, 2007.
- [66] P. REDHEAD, *vacuum* **12**, 203 (1962).
- [67] E. BORGUET and H.-L. DAI, *The Journal of Chemical Physics* **101**, 9080 (1994).
- [68] D. WOODRUFF and T. DELCHAR, *Modern Techniques of Surface Science*, Cambridge University Press, 1988.
- [69] J. KUBBY and J. BOLAND, *Surface Science Reports* **26**, 63 (1996).
- [70] J. TERSOFF and D. HAMANN, *Physical Review B (Condensed Matter)* **31**, 805 (1985).
- [71] G. BINNIG and H. ROHRER, *Reviews of Modern Physics* **59**, 615 (1987).
- [72] G. SOMORJAI, *Introduction to Surface Chemistry and Catalysis*, Wiley Interscience, 1994.
- [73] T. CHIANG, *Surface Science Reports* **39**, 181 (2000).
- [74] J. SAINIO, E. ALSHAMAILEH, J. LAHTINEN, and C. BARNES, *Surface Review and Letters* **10**, 641 (2003).
- [75] M. BRIDGE, C. COMRIE, and R. LAMBERT, *Surface Science* **67**, 393 (1977).
- [76] B. JOHNSON, P. BERLOWITZ, D. GOODMAN, and C. BARTHOLOMEW, *Surface Science* **217**, 13 (1989).
- [77] W. WEBER, A. BISCHOF, R. ALLENSPACH, C. BACK, J. FASSBENDER, U. MAY, B. SCHIRMER, R. JUNGBLUT, G. GUNTHERODT, and B. HILLEBRANDS, *Physical Review B* **54**, 4075 (1996).
- [78] R. MORONI, D. SEKIBA, F. DE MONGEOT, G. GONELLA, C. BORAGNO, L. MATTERA, and U. VALBUSA, *Physical Review Letters* **91**, 167207 (2003).
- [79] R. TOOMES and D. KING, *Surface Science* **349**, 1 (1996).
- [80] T. WADAYAMA, K. KUBO, T. YAMASHITA, T. TANABE, and A. HATTA, *Applied Surface Science* **199**, 254 (2002).

- [81] T. TANABE, T. SHIBAHARA, R. BUCKMASTER, T. ISHIBASHI, T. WADAYAMA, and A. HATTA, *Surface Science* **466**, 1 (2000).
- [82] J. ORTEGA, F. HIMPSEL, G. MANKEY, and R. WILLIS, *Physical Review B* **47**, 1540 (1993).
- [83] D. YU, M. DONATH, J. BRAUN, and G. RANGELOV, *Physical Review B* **68**, 155415 (2003).
- [84] S. YANG, K. GARRISON, and R. BARTYNSKI, *Phys. Rev. B* **43**, 2025 (1991).
- [85] N. SMITH, *Vacuum* **33**, 803 (1983).
- [86] F. HIMPSEL, *Journal of the Physics and Chemistry of Solids* **49**, 3 (1988).
- [87] P. JOHNSON and S. HULBERT, *Review of Scientific Instruments* **61**, 2277 (1990).
- [88] F. HIMPSEL and J. ORTEGA, *Physical Review B* **46**, 9719 (1992).
- [89] A. GOLDMANN, V. DOSE, and G. BORSTEL, *Phys. Rev. B, Condens. Matter (USA)* **32**, 1971 (1985).
- [90] N. SMITH, *Phys. Rev. B, Condens. Matter (USA)* **32**, 3549 (1985).
- [91] A. DANESE, F. CURTI, and R. BARTYNSKI, *Physical Review B* **70**, 165420 (2004).
- [92] P. BAGUS, K. HERMANN, P. AVOURIS, A. ROSSI, and K. PRINCE, *Chemical Physics Letters* **118**, 311 (1985).
- [93] G. RANGELOV, N. MEMMEL, E. BERTEL, and V. DOSE, *Surface Science* **251-252**, 965 (1991).
- [94] N. SMITH, N. BROOKES, Y. CHANG, and P. JOHNSON, *Phys. Rev. B, Condens. Matter (USA)* **49**, 332 (1994).
- [95] M. MILUN, P. PERVAN, and D. WOODRUFF, *Rep. Prog. Phys. (UK)* **65**, 99 (2002).
- [96] E. MCRAE and M. KANE, *Surf. Sci. (Netherlands)* **108**, 435 (1981).
- [97] A. DANESE and R. BARTYNSKI, *Phys. Rev. B, Condens. Matter Mater. Phys. (USA)* **65**, 174419 (2002).
- [98] D. YU, M. DONATH, J. BRAUN, and G. RANGELOV, *Phys. Rev., B, Condens. Matter Mater. Phys. (USA)* **68**, 155415 (2003).
- [99] D. ASHCROFT, N. & MERMIN, *Solid State Physics*, Brooks Cole, 1976.
- [100] P. ECHENIQUE and J. PENDRY, *Progress in Surface Science* **32**, 111 (1989).
- [101] J. B. PENDRY and S. B. GURMAN, *Surface Science* **49**, 87 (1975).
- [102] G. BLYHOLDER, *Journal of Physical Chemistry* **68**, 2772 (1964).

- [103] G. GANTEFOR, G. SCHULZE ICKING-KONERT, H. HANDSCHUH, and W. EBERHARDT, *Int. J. Mass Spectrom. Ion Process. (Netherlands)* **159**, 81 (1996).
- [104] R. HOFFMANN, *Reviews of Modern Physics* **60**, 601 (1988).
- [105] B. PERSSON and R. RYBERG, *Physical Review B* **24**, 6924 (1981).
- [106] H. UEBA, *Surface Science* **188**, 421 (1987).
- [107] R. WILLIS, A. LUCAS, and G. MAHAN, *Vibrational properties of adsorbed molecules*, Elsevier, Amsterdam, 1983.
- [108] G. D. MAHAN and A. A. LUCAS, *The Journal of Chemical Physics* **68**, 1344 (1978).
- [109] H. UEBA, *Journal of Electron Spectroscopy and Related Phenomena* **44**, 37 (1987).
- [110] B. TREMBLAY, L. MANCERON, G. GUTSEV, L. ANDREWS, and H. PARTRIDGE, *Journal of Chemical Physics* **117**, 8479 (2002).
- [111] K. SINNIH, H. DORSETT, and J. REUTT-ROBEY, *Journal of Chemical Physics* **98**, 9018 (1993).
- [112] M. ZHOU and L. ANDREWS, *Journal of Physical Chemistry A* **102**, 10250 (1998).
- [113] J. LAUTERBACH, M. WITTMANN, and J. KUPPERS, *Surface Science* **279**, 287 (1992).
- [114] B. TREMBLAY, G. GUTSEV, L. MANCERON, and L. ANDREWS, *Journal of Physical Chemistry A* **106**, 10525 (2002).
- [115] A. ZANGWILL, *Physics at Surfaces*, Cambridge University Press, 1992.
- [116] T. RAEKER and A. DEPRISTO, *J. Vac. Sci. Technol. A, Vac. Surf. Films (USA)* **10**, 2396 (1992).
- [117] W. SCHINDLER, T. KOOP, A. KAZIMIROV, G. SCHERB, J. ZEGENHAGEN, T. SCHULTZ, R. FEIDENHANS, and J. KIRSCHNER, *Surface Science* **465**, 783 (2000).
- [118] W. KIRSTEIN, B. KRUGER, and F. THIEME, *Surf. Sci. (Netherlands)* **176**, 505 (1986).
- [119] K. HEINZ, S. MULLER, and L. HAMMER, *J. Phys., Condens. Matter. (UK)* **11**, 9437 (1999).
- [120] S. MULLER, B. SCHULZ, G. KOSTKA, M. FARLE, K. HEINZ, and K. BABERSCHKE, *Surf. Sci. (Netherlands)* **364**, 235 (1996).
- [121] W. PLATOW, U. BOVENSIEPEN, P. POULOPOULOS, M. FARLE, K. BABERSCHKE, L. HAMMER, S. WALTER, S. MULLER, and K. HEINZ, *Phys. Rev. B, Condens. Matter (USA)* **59**, 12641 (1999).

- [122] D. GOODMAN, J. YATES, J.T., and T. MADEY, *Surf. Sci. (Netherlands)* **93**, 135 (1980).
- [123] J. SHEN, J. GIERGIEL, and J. KIRSCHNER, *Phys. Rev. B, Condens. Matter (USA)* **52**, 8454 (1995).
- [124] E. WHANG, J. OH, S. KIM, J. KIM, and G. LEE, *Phys. Rev. B* **63**, 075401 (2001).
- [125] A. GOLDMANN, M. DONATH, W. ALTMANN, and V. DOSE, *Phys. Rev. B, Condens. Matter (USA)* **32**, 837 (1985).
- [126] K. STARKE, K. ERTL, and V. DOSE, *Phys. Rev. B, Condens. Matter (USA)* **45**, 6154 (1992).
- [127] D. WOODRUFF, N. SMITH, P. JOHNSON, and W. ROYER, *Phys. Rev. B, Condens. Matter (USA)* **26**, 2943 (1982).
- [128] P. JOHNSON and N. SMITH, *Phys. Rev. B, Condens. Matter (USA)* **27**, 2527 (1983).
- [129] R. GARRETT and N. SMITH, *Phys. Rev. B, Condens. Matter (USA)* **33**, 3740 (1986).
- [130] J. YATES, J.T. and D. GOODMAN, *J. Chem. Phys. (USA)* **73**, 5371 (1980).
- [131] M. KISKINOVA and D. GOODMAN, *Surf. Sci. (Netherlands)* **108**, 64 (1981).
- [132] E. KAMPSHOFF, E. HAHN, and K. KERN, *Phys. Rev. Lett.* **73**, 704 (1994).
- [133] A. ULMAN, *Chemical Reviews* **96**, 1533 (1996).
- [134] F. BUSSOLOTTI, M. BETTI, and C. MARIANI, *Physical Review B* **74**, 125422 (2006).
- [135] J. ORTEGA and F. HIMPSEL, *Phys. Rev. Lett. (USA)* **69**, 844 (1992).
- [136] D. LI, J. PEARSON, J. E. MATTSON, S. D. BADER, and P. D. JOHNSON, *Phys. Rev. B* **51**, 7195 (1995).
- [137] J. PRITCHARD, *Surface Science* **79**, 231 (1979).
- [138] S. K. C. JEANETTE C. COOK and E. M. MCCASH, *J. Chem. Soc., Faraday Trans.* **93**, 2315 (1997).
- [139] J. COOK and E. MCCASH, *Surface Science* **356**, 445 (1996).
- [140] K. HORN and J. PRITCHARD, *Surface Science* **55**, 701 (1976).
- [141] J. REUTT-ROBEY, D. DOREN, Y. CHABAL, and S. CHRISTMAN, *Journal of Chemical Physics* **93**, 9113 (1990).
- [142] F. BUSSOLOTTI, V. CORRADINI, V. DI CASTRO, M. BETTI, and C. MARIANI, *Surface Science* **566-568**, 591 (2004).

- [143] D. WOODRUFF, *Applied Surface Science* **254**, 76 (2007).
- [144] F. ALLEGRETTI, F. BUSSOLOTTI, D. WOODRUFF, V. DHANAK, M. BECCARI, V. DI CASTRO, M. BETTI, and C. MARIANI, *Surface Science* **602**, 2453 (2008/07/15).
- [145] J. SCHON, H. MENG, and Z. BAO, *Nature* **413**, 713 (2001).
- [146] S. LUKAS, G. WITTE, and C. WOLL, *Physical Review Letters* **88**, 283011 (2002).
- [147] M. OHARA, Y. KIM, and M. KAWAI, *Japanese Journal of Applied Physics* **44**, 5390 (2005).
- [148] W. SHEN, G. NYBERG, and J. LIESEGANG, *Surface Science* **298**, 143 (1993).
- [149] M. SCHMIDT, K. BALDRIDGE, J. BOATZ, S. ELBERT, M. GORDON, J. JENSEN, S. KOSEKI, N. MATSUNAGA, K. NGUYEN, S. SU, T. WINDUS, M. DUPUIS, and J. MONTGOMERY, J.A., *Journal of Computational Chemistry* **14**, 1347 (1993).
- [150] A. GRANOVSKY, PC GAMESS/Firefly version 7.1.F,
<http://classic.chem.msu.su/gran/gamess/index.html>.
- [151] A. FERRETTI and R. DI FELICE, *Physical Review B (Condensed Matter and Materials Physics)* **70**, 115412 (2004).
- [152] S. DRIVER and D. WOODRUFF, *Surface Science* **479**, 1 (2001).
- [153] M. VARGAS, P. GIANNOZZI, A. SELLONI, and G. SCOLES, *Journal of Physical Chemistry B* **105**, 9509 (2001).
- [154] H. KONDOH, M. IWASAKI, T. SHIMADA, K. AMEMIYA, T. YOKOYAMA, T. OHTA, M. SHIMOMURA, and S. KONO, *Physical Review Letters* **90**, 066102 (2003).
- [155] T. HAYASHI, Y. MORIKAWA, and H. NOZOYE, *Journal of Chemical Physics* **114**, 7615 (2001).
- [156] S. VOLLMER, G. WITTE, and C. WOLL, *Langmuir* **17**, 7560 (2001).
- [157] S. DRIVER and D. WOODRUFF, *Surface Science* **488**, 207 (2001).
- [158] M. COLAIANNI and I. CHORKENDORFF, *Physical Review B (Condensed Matter)* **50**, 8798 (1994).
- [159] M. WEDLOCK, A. RINKER, and C. HALLEMAN, *Chemical Physics Letters* **414**, 505 (2005).
- [160] B. SEXTON and G. NYBERG, *Surface Science* **165**, 251 (1986).
- [161] P. LINSTROM and E. W.G. MALLARD, NIST Chemistry WebBook,
<http://webbook.nist.gov>.

Vita

Levan Tskipuri

Education

10/2009	Ph.D. degree at Rutgers University, USA.
09/2003 - 08/2009	Rutgers University
07/2002	M.S. degree at Tbilisi State University, Georgia.
10/2000 - 07/2002	Tbilisi State University
06/2000	B.S. degree at Tbilisi State University, Georgia.
09/1996 - 06/2000	Tbilisi State University

Publications

Carbon monoxide adsorption on the metastable fcc-Co/Cu(100) surface, L. Tskipuri and R.A. Bartynski; Surface Science, v 603, p 802-6, (2009)

Impurity breakdown under transverse runaway of hot electrons, N. Meterveli, Z. Kachlishvili, F. Chumburidze, L. Tskipuri; Physica Status Solidi B, v 240, p 584-90, (2003)